Bistatic Synthetic Aperture Radar Processing

DISSERTATION
zur Erlangung des Grades eines Doktors
der Ingenieurwissenschaften (Dr.-Ing.)
Vom Fachbereich Elektrotechnik und Informatik

vorgelegt von
M.Sc. Qurat-Ul-Ann

eingereicht bei der Naturwissenschaftlich-Technischen Fakultät
der Universität Siegen
Siegen 2013

1. Gutachter: Prof. Dr.-Ing. Otmar Loffeld
2. Gutachter: Prof. Dr.-Ing. Joachim Ender
Vorsitzender der Prüfungskommission: Prof. Dr.-Ing. Hubert Roth

Tag der mündlichen Prüfung: 17.04.2014

Acknowledgement

I owe my deepest gratitude for my advisor, Prof. O. Loffeld, for his devoted guidance and encouragement throughout my research work. I greatly appreciate his motivating attitude and knowledgeable discussions, which were of great help to me for getting a real insight of the topic. I am also grateful to my second advisor, Prof. J. Ender for his generosity, informative lectures and worthy suggestions. I would also like to thank other members of the thesis committee for their feedback. I am much obliged to our team leader, Dr. Holger Nies for his helpful suggestions, many fruitful and interesting discussions, which greatly facilitated the progress of my work. I am thankful to all my colleagues of SAR group: Amaya Medrano Ortiz, Wei Yao, Ashraf Samarah, Jinshan Ding, Florian Behner, Simon Reuter, Thomas Espeter, Simon Meckel, Dr. Wang and Dr. Knedlik for their friendly attitude. I would like to thank Mrs. Niet-Wunram, Mrs. Haut, Mrs. Szabo, Mr. Stadermann, Mr. Twelsiek, the faculty and other colleagues at the Center for Sensor Systems (ZESS) for their kindness. I am grateful to the Higher Education Commission of Pakistan (HEC), the Deutsche Akademischer Austausch Dienst (DAAD) and the University of Siegen, for their financial support. I am thankful to my grandfather, who has always encouraged and motivated me for higher studies. I am also thankful to my parents, brother and sister for their never ending support, love and lots of prayers. Finally, I am grateful to my husband and children for their love, support and wonderful company during my stay in Siegen.

Qurat Ul Ann

Abstract

The interest in bistatic SAR processing has increased tremendously over the years. It is not only a useful advancement of monostatic SAR but offers considerable flexibility in designing SAR mission, improves classification and detection of objects in SAR images, provides additional information about the observed scene, reduces vulnerability in military applications, etc. Besides all these advantages, a bistatic SAR configuration offers a complex geometry with increased processing complexities.

In order to achieve a computationally efficient processing approach, a frequency domain processor has been considered in this thesis for different bistatic SAR configurations. As a first step, the corresponding bistatic point target reference spectrum has been derived. Based on this spectrum an appropriate focusing algorithm is implemented. It is then used to focus both simulated and real bistatic SAR data for various bistatic SAR configurations. The results obtained using frequency domain algorithm, are compared with those obtained using a time domain (back projection) algorithm. A detailed analysis of the data shows that the frequency domain processor provides very good quality images.

Kurzfassung

Das Interesse an bistatischer SAR-Verarbeitung ist in den letzten Jahren enorm gestiegen. Es ist nicht nur eine sinnvolle Weiterentwicklung des monostatischen SAR sondern bietet ein hohes Maß an Flexibilität in der Entwicklung neuer SAR-Missionen, verbesserte Klassifizierung und Entdeckung von Objekten in SAR-Bildern, liefert weitere Informationen über die zu beobachtende Szene, reduziert die Entdeckungswahrscheinlichkeit der Trägerplatform in militärischen Anwendungen usw. Neben all diesen Vorteilen führt eine bistatischen SAR-Konfiguration eine komplexere Geometrie mit erhöhter Verarbeitungskomplexität herbei, als es beim monostatischen SAR der Fall ist.

Um eine rechentechnisch effiziente Verarbeitung zu erreichen, wurde ein Frequenzbereichsprozessor für verschiedene bistatischen SAR-Konfigurationen in dieser Arbeit entwickelt. Als erster Schritt wurde das bistatischen Punktziel Referenzspektrum hergeleitet. Basierend auf diesem Spektrum wurde ein entsprechender Fokussierungsalgorithmus implementiert. Die Verifizierung erfolg mit realen und simulierten bistatischen SAR-Daten für verschiedene bistatische SAR Konstellationen. Die Ergebnisse des Frequenzbereichsalgorithmus wurden mit denen einer Zeitbereichsmethode

(Rückprojektionalgorithmus) verglichen. Eine detailierte Analyse zeigt, dass der hergeleitete Frequenzbereichsprozessor sehr gute Fokussierungsergebnisse liefert.

Index of Contents

List of Figures

List of Tables

List of Acronyms

AER-II	Airborne Experimental Radar
AIC	Azimuth Invariant Configurations
AVC	Azimuth Variant Configurations
BPTRS	Bistatic Point Target Reference Spectrum
COSMO	Constellation of small Satellites for Mediterranean basin Observation
CSA	Canadian Space Agency
CNES	Centre National d'Etudes Spatiales (French Space Agency)
DEM	Digital Elevation Model
DPLL	Digital Phase Locked Loop
DLR	Deutsches Zentrum für Luft und Raumfahrt (German Space Agency)
EM	Electromagnetic Radiations
ERS	European Remote Sensing
ESA	European Space Agency
FGAN	Forschungsgesellschaft für Angewandte Naturwissenschaften (Research Establishment for Applied Natural Sciences)
FFT	Fast Fourier Transformation
GMES	Global Monitoring for Environment and Security
GPS	Global Positioning System
IDL	Interactive Data Language
IFFT	Inverse Fast Fourier Transformation
INS	Inertial Navigation System
InSAR	Interferometric Synthetic Aperture Radar
IRW	Impulse Response Width
ISLR	Integrated Side Lobe Ratio
JERS	Japan Earth Remote Sensing Satellite
LBF	Loffeld's Bistatic Formula
MSP	Method of Stationary Phase

NASA	National Aeronautics and Space Administration
NASDA	National Space Development Agency
NRL	Naval Research Laboratory
ONERA	Office National d'Études et de Recherches AÉrospatiales (French Aerospace Research Center)
PAMIR	Phased Array Multifunctional Imaging Radar
PCA	Point of Closest Approach
PRF	Pulse Repetition Frequency
PRI	Pulse Repetition Interval
PSLR	Peak Side Lobe Ratio
PSP	Point of Stationary Phase
PT	Point Target
QinetiQ	British Defense Technology Company
RADAR	Radio Detection and Ranging
RAR	Real Aperture Radar
RCMC	Range Cell Migration Correction
SAR	Synthetic Aperture Radar
SABRINA	SAR Bistatic fixed Receiver for Interferometric Applications
SIFT	Scaled Inverse Fourier Transformation
SIR	SAR Imaging Radar
SLAR	Side-Looking Aperture Radar
SNR	Signal to Noise Ratio
TBP	Time Bandwidth Product
TI	Translational Invariant
TIRA	Tracking and Imaging Radar
ZESS	Center for Sensor System, University of Siegen

List of Symbols

δ_{range}	Slant range resolution
$\delta_{azimuth}$	Azimuth resolution
c_0	Velocity of light (i.e. $3\times10^8 m/s$)
B_r	Transmitted signal bandwidth
τ	Azimuth time (Slow time)
t	Range time (Fast time)
t_0	Two ways signal traveling time
$R_R(\tau)$	Receiver's slant range
$R_T(\tau)$	Transmitter's slant range
τ_{0R}	Azimuth time when receiver is at closest distance from the point target
τ_{0T}	Azimuth time when transmitter is at closest distance from the point target
R_{0R}	Slant range when receiver is at closest distance from the point target
R_{0T}	Slant range when transmitter is at closest distance from the point target
v_R	Receiver's velocity
v_T	Transmitter's velocity
$P(R_{0R},\tau_{0R})$	Point target in receiver's coordinates
$d(\tau_{0R})$	Distance between transmitter and receiver at receiver's PCA
a_0	Difference between transmitter and receiver azimuth times at PCA
a_2	Ratio of transmitter and receiver slant ranges at PCA
f_0	Carrier frequency
f	Range frequency
f_τ	Azimuth frequency
f_{dc}	Doppler centroid

$f_{\tau T}$	Weighted azimuth transmitter frequency
$f_{\tau R}$	Weighted azimuth receiver frequency
$s_l(t)$	Transmitted signal
$g_l(t)$	Received signal in time domain
$\sigma\left(R_{0R},\tau_{0R}\right)$	Backscattering coefficient
$\omega\left(\tau-\tau_c\right)$	Azimuth time window with center time τ_c
$G_l(f)$	Received signal in frequency domain
ϕ_B	Bistatic phase term
ϕ_R	Receiver's phase term
ϕ_T	Transmitter's phase term
ϕ_S	Intermediate phase term
μ	Weighting factor
$\tilde{\tau}_T$	Individual PSP of transmitter
$\tilde{\tau}_R$	Individual PSP of receiver
$\tilde{\tau}$	Common point of stationary phase
Ψ_{QM}	Quasi monostatic phase term
Ψ_{BD}	Bistatic deformation phase term
f_{DCt}	Doppler centroid transmitter
f_{DCr}	Doppler centroid receiver
θ_{SQt}	Squint angle transmitter
θ_{SQr}	Squint angle receiver
E_T	Transmitter range rate error
E_R	Receiver range rate error
L_{1T}	First validity constraint of transmitter
L_{1R}	First validity constraint of receiver

L_{2T}	Second validity constraint of transmitter
L_{2R}	Second validity constraint of receiver
μ_{+}	Upper limit of weighting factor
μ_{-}	Lower limit of weighting factor
Ψ_{CS}	Complete scene phase term
Ψ_{LCS}	Linearized complete scene phase term
Ψ_{CS0}	Space invariant complete scene phase term
Ψ_{CS_Ra}	Range variant complete scene phase term
Ψ_{CS_Az}	Azimuth variant complete scene phase term
A_{Ra}	Range shift term
B_{Ra}	Range scaling term
A_{Az}	Azimuth shift term
B_{Az}	Azimuth scaling term

1 Introduction and Historical Background

A significant contribution to the evolution of radar technology was made by a German physicist, Heinrich Hertz (1857-1894). As a result of his experiments, he witnessed the reflection of electromagnetic waves by metallic objects and successfully proved the generation and detection of radio waves. A Scottish physicist, James Clerk Maxwell (1831-1879) had also predicted the existence of electromagnetic waves and his theoretical investigations led to the formation of the renowned Maxwell's equations. Guglielmo Marconi, the pioneer of wireless communication, was a keen promoter of practical radio systems. In 1904, a German engineer, Christian Hülsmeyer gave a public demonstration regarding the detection of ships in fog and poor visibility scenarios using radio waves. He was the first one to build a simple ship detection device called the 'Telemobiloscope' but the naval authorities of that time failed to recognize its worth (registered as patent Nr. 165546).

Before the Second World War, parallel efforts for the development of radar systems were initiated by the British, the Germans, the French, the Soviets, the Japanese and the Americans. In USA, most of the earlier developments were made by the Naval Research Laboratory (NRL). In 1930s, both United Kingdom and Germany were successful in demonstrating the tracking of aircrafts using short pulse ranging measurements. In 1937, first operational radar system was developed in United Kingdom by Robert Watson-Watt and his companions. Their work proved useful during the Second World War to track the aircrafts across Europe.

The word RADAR is an acronym suggested by the U.S. Navy in 1940. It stands for RAdio Detection And Ranging. Since the Second World War, it has been used for observation purposes. It is a magnificent tool to detect objects and measure their range (distance) and speed. Later the technological developments over decades made it possible to construct images of the Earth's surface, using Synthetic Aperture Radar (SAR) principles.

1.1 Synthetic Aperture Radar

Imaging active sensors operating in the microwave region of the electromagnetic (EM) spectrum are usually referred to as the Real Aperture Radar (RAR). They offer day and night including all weather imaging along with continuous and global monitoring of the Earth's surface. The main limitation of these sensors is the poor cross range resolution, which is directly proportional to the radiated wavelength and slant range from the sensor to the surface and inversely proportional to the length of sensor's antenna. It means

that if a satellite is operating at a point, say, hundreds of kilometers of altitude from the surface, it would require an antenna of length from several hundred meters to kilometers depending on the wavelength of transmitted signal in order to achieve a resolution in meters. Such a long antenna is practically not feasible. This limitation was overcome using the concept of SAR, where azimuth resolution is independent of the sensor's altitude (see section 1.2.1).

SAR usually referred as the imaging radar, utilizes the concept of creating a very long antenna aperture with the help of signal processing techniques. SAR principle was first registered as a patent in 1954 by Carl A. Wiley of the Goodyear Aerospace Corporation, titled "Pulsed Doppler Radar Method and Means" (US Patent Nr. 3.196.436). He used the Doppler information to increase the azimuth resolution of the Side Looking Aperture Radar (SLAR). The first satellite carrying a SAR sensor was launched in 1978 by NASA for remote sensing applications. The data collected in a 100 days mission of Seasat-A showed that SAR is a wonderful tool for measuring the Earth's surface characteristics. It is a coherent system which retains both amplitude and phase of the backscattered echo signals. It combines the echo signals from each pulse to produce a high resolution image of the terrain as compared to that obtained by a much larger antenna.

SAR technology can be used with aircrafts (Airborne SAR), satellites (Satellite/Spaceborne SAR) or a combination of both aircrafts and satellites (Hybrid SAR). The data collected by SAR sensors is called raw data. Important information lies in the phase of this raw data and with appropriate processing algorithm it can be transformed into a focused SAR image. More details of SAR processing will be provided in the next chapters.

1.1.1 SAR Advantages and Applications

SAR, as an active microwave sensor is capable of monitoring continuously the properties of the geophysical parameters of the Earth's surface. It opens new horizons for the remote sensing and global monitoring of the Earth's natural resources. Being an active sensor, it transmits EM radiations in the microwave region of the EM spectrum. Therefore, it is independent of sunlight. Thus, allowing continuous day and night operations. Spaceborne SAR sensors operate generally between 1-10 GHz (3-30 cm) of microwave region. It is possible to choose appropriate wavelength of the transmitted signal which offers less attenuation due to clouds, fog and precipitation. Thus, it is suitable for all weather conditions. It offers good resolution at remote distances, large area coverage and rapid data acquisition throughout the year. It has made possible to continuously monitor and gain information about the ocean currents, iceberg movements, oil films on ocean waters, surface mapping, geological structures, soil moisture, soil erosion, floods, forest ecology, etc. In comparison with the optical sensors, the EM waves emitted by

the SAR sensors reflect differently from different materials and thus can provide a better discrimination of the surface features. It is possible to acquire images of areas with backscattering characteristics of EM radiations and it also offers better resolution as compared to the conventional radar systems. SAR is widely used in the applications for remote sensing and mapping of the surface of the Earth and of the other planets.

1.2 SAR Principle

The basic principle of SAR is to synthesize a longer antenna aperture with the help of spaceborne or airborne platform to achieve better azimuth resolution. As the platform moves along the trajectory, it transmits pulses at regular azimuth time intervals. The reflected echoes are linear superposition of the received signals of each point target within the antenna's foot print and are coherently recorded and processed. This post processing technique creates a larger synthetic aperture as compared to the physical antenna length and hence generates high resolution SAR images. The length of the flight path during which point target remains illuminated corresponds to the synthetic aperture length as shown in Figure 1. In monostatic SAR, same sensor is used for the transmission and reception of radar pulses. The range of the point target varies with the motion of platform. It decreases and reaches its minimum value at point of closest approach (shortest distance between point target and platform trajectory) and then increases as the platform moves. Hence, the range history in this case, takes the shape of a hyperbola.

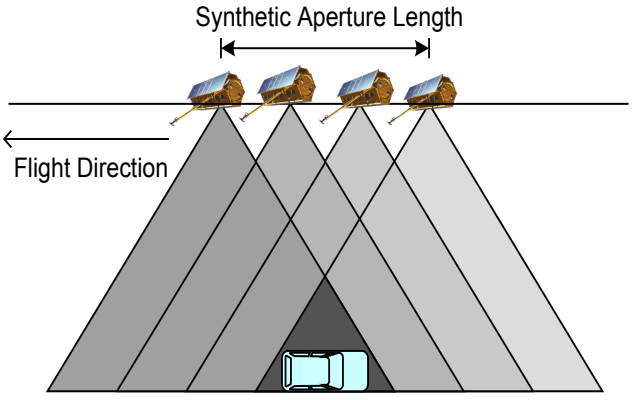

Figure 1: Synthetic Aperture Length

Pulses are emitted by the antenna which illuminates the Earth's surface. The ground area illuminated by the pulses is called the antenna's footprint as shown in Figure 2. The illuminated ground area may consist of large number of small point targets. Each point target reflects the signal back to the antenna according to its own backscattering strength. The along track motion of the sensor is called azimuth direction. The slant

range represents the distance from the antenna to the point target and is a measure of the roundtrip propagation delay of the radar pulses.

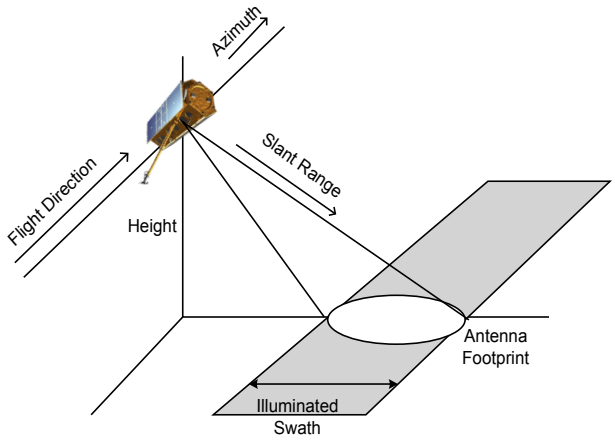

Figure 2: SAR Principle

The reflected signal is basically the superposition of the back scattered signals from all point targets in the antenna footprint. The received signal is demodulated from its carrier signal and is converted into a baseband signal. It is then recorded as two dimensional raw data. This raw data is processed using a focusing algorithm. The focused image is superposition of impulse responses from all point targets.

1.2.1 SAR Resolution

The pulse length used in the practical systems is long enough to obtain a good resolution. Pulse compression technique is used to obtain narrow pulses and hence fine resolution in the range direction. Slant range resolution is defined as:

$$\delta_{range} = \frac{c_0}{2B_r} \tag{1.1}$$

It depends on the transmitted pulse bandwidth B_r and the velocity of light c_0. It does not depend on the physical antenna length.

In azimuth direction better resolution is obtained by using the fact that different scatterers in a radar beam reflect energy with a different Doppler shift. Using this Doppler shift an aperture of several kilometers can be synthesized with an improved azimuth resolution. In stripmap SAR mode (explained in section 1.4), the azimuth resolution is given as:

$$\delta_{azimuth} = \frac{L}{2} \tag{1.2}$$

The azimuth resolution is equal to half of the physical antenna length L and it is independent of the slant range. The azimuth resolution is also called along track or cross range resolution.

1.3 Bistatic SAR

Bistatic SAR is a promising and useful advancement of monostatic SAR systems. In general bistatic SAR configurations, transmitter and receiver are located on different platforms, thus offering considerable flexibility in designing bistatic SAR missions using a combination of spaceborne, airborne or stationary ground-based platforms. Classification of objects in bistatic SAR images is improved and additional information of scene is obtained using bistatic SAR systems. Another advantage of bistatic SAR is to use one transmitter with several passive receivers. In a hostile environment, it is more appropriate to use an active transmitter far from the scene with passive receivers located closer to the scene. As the receiver is passive, therefore it can not be easily detected. In bistatic SAR images, dihedral and polyhedral effects are reduced especially in the urban areas, due to decrease in multipath scattering. They can image in flight direction and backwards.

Despite all these advantages, bistatic SAR configurations offer many technical challenges. Major challenges are time synchronization of transmitter and receiver platforms and motion compensation. Bistatic SAR processing itself is a non trivial task. Advancements in navigation and communication technologies made it possible to address some of these issues. European radar research institutes like German space agency (DLR), Fraunhofer institute for high frequency physics and radar techniques-FHR (former FGAN), ONERA and QinetiQ have made remarkable progress in the spaceborne/airborne bistatic SAR experiments [19]-[22].

1.4 SAR Modes

SAR can be operated in different modes. The basic operating modes are stripmap, scan and spotlight. In stripmap SAR mode, antenna points to a fixed direction with respect to the flight path and the antenna's footprint sweeps a strip on the ground during sensor's flight as shown in Figure 3. It enables continuous imaging. The azimuth resolution depends on the length of antenna. The image dimension is limited in range but not in azimuth.

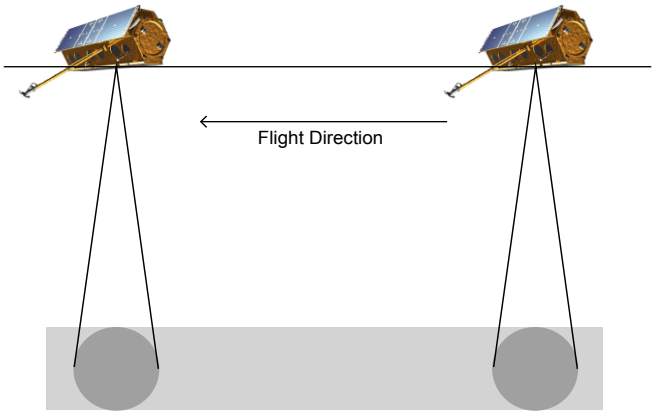

Figure 3: Stripmap SAR Mode

In scan SAR mode, a wider range swath is imaged as compared to the stripmap SAR. During data intake, antenna is scanned in range several times which is achieved by periodically shifting the antenna beam to neighboring sub swaths, as shown in Figure 4. SAR operates continuously but only a portion of synthetic aperture is available for each target in sub swath. The azimuth resolution is therefore decreased as compared to the stripmap mode due to wide swath. This mode provides a trade off between wider range swath dimensions and poor azimuth resolution.

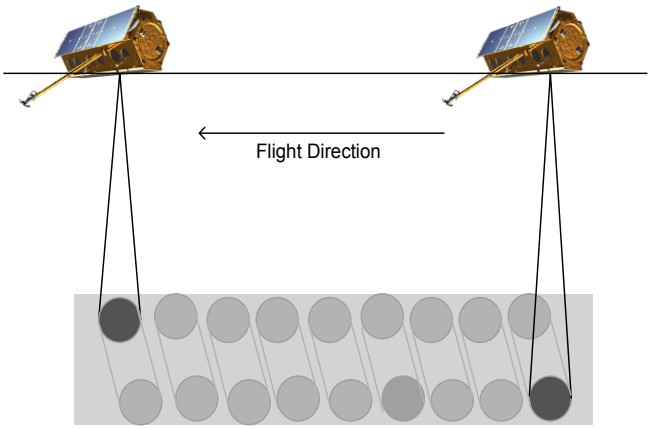

Figure 4: Scan SAR Mode

The spotlight mode is used to image some area of interest or spot on the ground as shown in Figure 5. The radar antenna is steered to illuminate the spot during the overall data acquisition time. It does not offer continuous imaging but an improved azimuth resolution due to increase in angular extent of illumination of the spot. In this mode, beam is steered backward as the sensor moves forward thus creating an effect of a wider antenna beam. The number of received backscattered echoes by each target in the scene increases significantly as compared to the stripmap mode, thus improving azimuth resolution. This mode provides a trade off between better azimuth resolution and limited coverage area.

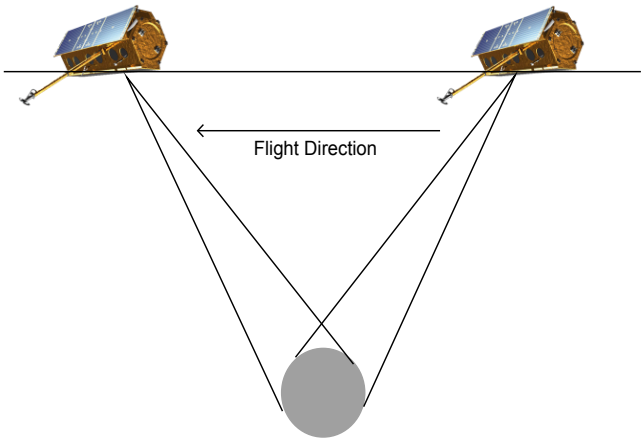

Figure 5: Spotlight SAR Mode

The sliding SAR mode is a combination of stripmap and spotlight as shown in Figure 6. In this mode, antenna's footprint slides over the Earth's surface with accelerated or reduced footprint velocity with respect to the platform's velocity (aircraft or satellite). The looking direction of the antenna beam can be forward or backward. This mode offers a balance between azimuth scene extent and resolution.

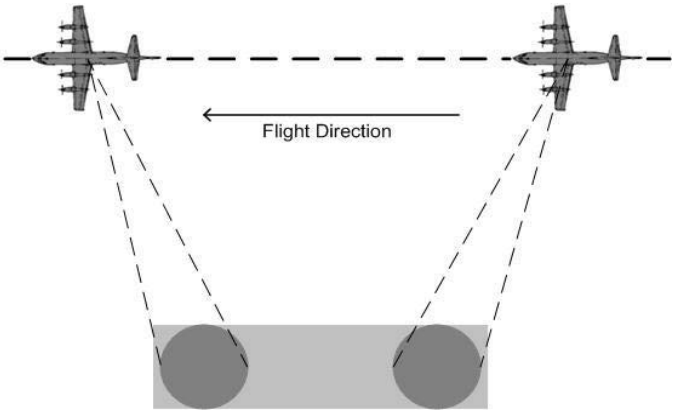

Figure 6: Sliding SAR Mode

In the inverse SAR mode, SAR sensor is stationary and target is moving which can be used to track aircrafts and satellites from a ground base radar system. In this mode movement of targets generates the synthetic antenna.

The Interferometric SAR (InSAR) provides an opportunity for obtaining 3D SAR images. They are obtained by combining two or more coherent images of the same scene taken by two antennas with slightly different observation angles and exploring the phase difference among them. It is also referred to as the phase interferogram. If the two antennas are separated along range and are perpendicular to the flight track, they are called across track InSAR. Across track InSAR configurations may consist of a system with two antennas which can be present at the same time on aircraft or spacecraft (single pass

interferometer) or a system with a single antenna having two time separated passes over the same scene (two pass interferometer).

1.5 Spaceborne SAR Missions

The launch of Seasat in 1978 by NASA has opened a new era in the remote sensing. It was the first civilian spaceborne SAR. It operated at L-band. Later during 1990s, the European Space Agency (ESA), the National Space Development Agency (NASDA) of Japan and the Canadian Space Agency (CSA) decided to join NASA for developing SAR systems for global monitoring of the Earth's natural resources. In March 1991, the Soviet Union launched S-band satellite named ALMAZ. Followed by the launch of ERS-1 (European Remote Sensing Satellite) which was a C-band SAR system. The image showed in Figure 7 is captured by ERS-1 (SAR) of Malaspina glacier in Alaska in July 1992. In 1995, ERS-2 was launched which was identical to the ERS-1. Both satellites shared the same orbit with the time delay of one day at an altitude of almost 800 km. Such constellations helped to carry out the interferometric TanDEM-X mission.

Figure 7: ERS-1 (SAR) Image © ESA

Another successful mission was C/X band spaceborne SAR Imaging Radar (SIR) launched in 1994 on a space shuttle. It has recorded the SAR data in L, C and X band. An image of Petra region (Jordan) acquired by SIR-C/X (SAR) in April 1994 is shown in Figure 8. It was a joint mission of the German, Italian and American space agencies.

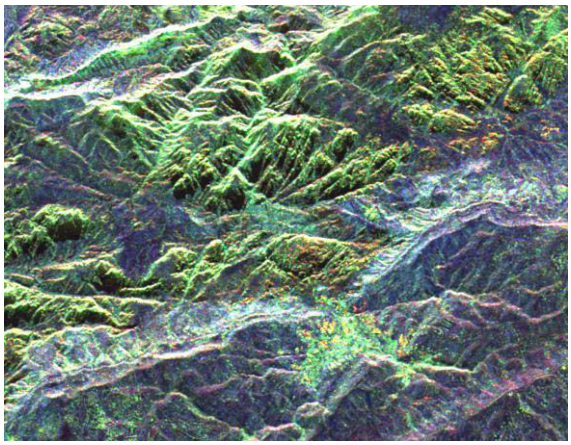

Figure 8: SIR-C/X (SAR) Image [Courtesy NASA/JPL-Caltech]

The Japanese Earth Remote Sensing (JERS-1) satellite was launched in 1992. It was an L-band SAR system for the observation of geological changes and environmental monitoring. The CSA launched RadarSat-1 in 1995. It was a C-band SAR system with the main purpose for daily monitoring of the Arctic glaciers and icebergs. It was capable of providing SAR images with a spatial resolution of 10m. RadarSat-2 was launched in 2007 which was able to provide a spatial resolution of 3m. COSMO-SkyMed (Constellation Of small Satellites for Mediterranean basin Observation) is an Earth observation Italian satellite system with X-band SAR sensors used for the global monitoring and coverage of the Earth's surface. The first COSMO-SkyMed satellite was launched in June 2007, followed by the launch of a second satellite in December 2007 and still another in October 2008. SAR-Lupe is a German satellite system of five identical satellites controlled by a ground station. It uses X-band and operates in spotlight and stripmap modes. Its first satellite was launched in December 2006 and the last one was launched in July 2008. Another, TerraSAR-X, a German Earth observation satellite was launched in 2007. Its data is available both for the scientific purposes and for the commercial use. It has ability to get high resolution Earth images and has been designed to carry out its tasks for five years. It can acquire radar data in stripmap, spotlight and scan SAR modes. It was followed by the launch of another satellite, TanDEM-X in June 2010. Both satellites work in pair to generate a global high resolution Digital Elevation Model (DEM) of the Earth.

The interferometric cartwheel was proposed by D. Massonnet [65] at a research program of the French Space Agency (CNES). It consists of multistatic SAR configuration of three passive micro satellites working with an active SAR satellite. Its purpose is to build a cost effective system which can produce an accurate DEM. The advantage of this concept is stable, horizontal and vertical baselines due to orbital configuration. Stable baselines are very important in the SAR interferometry as a small error in baseline leads to a large error in DEM. A combination of images from these micro satellites can

improve the final image resolution and can produce along and across track interferometric data.

Sentinel-1 is a future European radar observation satellite system (Figure 9). It is a C-band SAR mission expected to launch in 2013. Its data would be used by the Global Monitoring for Environment and Security (GMES) and ESA for land and ocean observations.

Figure 9: Sentinel-1 Satellite © ESA

Tandem-L is a proposed future satellite (Figure 10) for L-band interferometric and polarimetric SAR missions, used for global monitoring of forestation, forest biomass changes, earthquakes, volcanic activities, ice cover and mass changes, flooding etc.

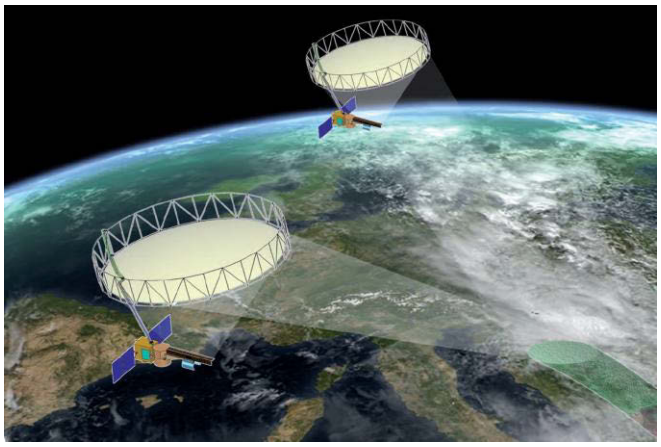

Figure 10: Tandem-L Satellite © DLR & ESA

1.6 SAR Processing

Different processing algorithms have been proposed to focus SAR data. Algorithms developed in the time domain to focus SAR data are more precise but computationally inefficient. On the other hand, algorithms developed in the frequency domain are more

efficient and easy to implement. Therefore, frequency domain algorithms are mostly preferred [1]-[55].

Bistatic SAR processing is more complicated than the monostatic SAR. Bistatic SAR data can be azimuth invariant as both transmitter and receiver can have different motion trajectories. In monostatic SAR, range history has a hyperbolic shape. Where as, in bistatic SAR range history is more complicated, as it is the sum of transmitter and receiver ranges. The sum of two hyperbolic range histories of the transmitter and receiver, results in a double square root term in the bistatic range history. It has the shape of flat-top hyperbola. It is not possible to focus the bistatic SAR data using monostatic SAR algorithms. They must be modified to handle bistatic SAR configurations.

Back projection algorithm is implemented in the time domain for SAR data processing. Its computational complexities can be reduced using fast back projection processing techniques. A frequency domain bistatic SAR processing approach was proposed by Prof. Rocca and his team at Milan Polytechnic University. They used a technique which was already available for monostatic SAR processing. In this preprocessing technique [14], Dip Move Out operator (also called as 'smile' operator) is used to convert bistatic SAR data into monostatic for constant offset configuration. Later, it has been extended to general bistatic SAR configurations. Prof. Ender and his team at Fraunhofer-FHR have proposed Omega–k algorithm for bistatic SAR processing for Translational Invariant (TI) configurations (transmitter and receiver moving parallel to each other with constant velocities and offset) and tandem configurations (transmitter and receiver following each other on a single path with constant offset) [20], [26]. They have also used back projection and range Doppler processors for real bistatic SAR data processing [19].

Prof. Bamler and his team at DLR (German Aerospace Center) proposed a numerical transfer function for TI configurations [34]. There focusing algorithm replaces the analytical SAR transfer function with numerical equivalent and are able to handle azimuth invariant and squinted configurations. I. Cumming, F. Wong and Y. Neo derived 2D point target reference spectrum based on extended nonlinear chirp scaling algorithm [41]-[42], and a method of series reversion for the processing of general bistatic SAR configurations [43].

Prof. Loffeld at the University of Siegen derived a Bistatic Point Target Reference Spectrum (BPTRS) known as Loffeld Bistatic Formula (LBF) for general bistatic SAR configurations [1]-[2], [6]-[8]. It consists of the quasi monostatic phase term and bistatic deformation term. A Scaled Inverse Fourier Transformation (SIFT) is used to process bistatic SAR data for general configurations [3], [5], [8]. It works well for those configurations where transmitter and receiver contribute equally towards the bistatic phase (e.g. tandem configurations, TI configurations) but for hybrid configurations it does not

focus in azimuth. Dr. Wang came up with the idea of extended Loffeld's bistatic formula [46]-[50] with unequal azimuth contribution of transmitter and receiver phases, by using the Time Bandwidth Product (TBP). My work is also based on the unequal azimuth contribution of transmitter and receiver phase terms for bistatic SAR configurations by using a weighting factor derived by minimizing the square difference between common and individual points of stationary phases of transmitter and receiver [53]-[57]. More details are given in the next chapters.

1.7 Structure of the Thesis

This thesis is structured as follows:

First chapter is based on the overview of synthetic aperture radar. Evolution of SAR over years, its working principle, its modes, spaceborne missions and processing techniques are discussed in **Chapter 1**.

Bistatic point target reference spectrum based on the Loffeld's bistatic formula is derived in **Chapter 2**. It presents the bistatic signal model and point target impulse response function. It is based on different azimuth contributions of transmitter and receiver phase terms.

Four validity constraints based on different azimuth contributions of transmitter and receiver phase terms are derived in **Chapter 3**. They were used to find different weighting to azimuth contribution of transmitter and receiver phases.

Focusing of the complete scene for different bistatic SAR configurations are discussed in **Chapter 4**. A frequency domain processing algorithm is implemented using a SIFT and is applied to focus real bistatic SAR data.

Stationary receiver configurations are considered in **Chapter 5**. A BPTRS is derived and based on it an appropriate frequency domain processing algorithm is implemented. This algorithm is used to focus the real bistatic SAR data obtained during the stationary receiver experiments conducted at the University of Siegen.

Finally, a summary of contributions to this thesis is provided in **Chapter 6**.

2 Bistatic Point Target Reference Spectrum

2.1 Introduction

An approximated BPTRS is derived in [1]. This frequency domain processing approach called LBF provides an analytical solution for focusing different bistatic SAR configurations. The method of stationary phase has been used in its derivations. The phase terms are expanded using Taylor's series around the individual stationary points of the transmitter and receiver.

This chapter contributes towards the theoretical understanding of the bistatic SAR signal model. It begins with the description of general bistatic SAR geometry. Using this geometry, a bistatic signal model is derived. Later, an analytical BPTRS based on LBF is derived, assuming different azimuth contributions of the transmitter and receiver phases. The transmitter and receiver phases are weighted differently based on their contributions towards the bistatic phase history.

2.2 Bistatic SAR Geometry

In bistatic SAR, transmitter and receiver are located on different carrier platforms. A general bistatic SAR configuration offers a complex geometry, with the transmitter and receiver moving in different directions with different velocities. The bistatic SAR configurations can be used in a variety of constellations between the transmitter and receiver e.g. using two airborne/spaceborne platforms as transmitter and receiver, spaceborne platform as transmitter with an airborne platform as receiver, or a moving transmitter platform with a stationary receiver, etc. The transmitter and receiver are separated in space but they must be synchronized by using some communication channel or by direct reception of the transmitted signal by the receiving unit.

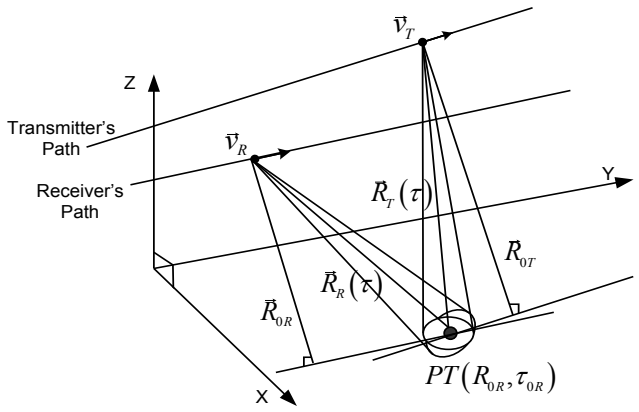

Figure 11: Bistatic SAR Geometry

The bistatic SAR geometry of a general configuration is shown in Figure 11. We suppose a flat Earth model and a Cartesian coordinate system. The platforms are flying along y-axis and their heights are along z-axis. The imaged scene is in the xy-plane. Here we assume that the transmitter and the receiver are moving with different velocities along non parallel tracks. The velocity vectors of the transmitter and receiver are denoted by $\vec{v}_T$ and $\vec{v}_R$. The time along the flight axis is called the azimuth time τ. The distances of the transmitter and the receiver from the point target are referred as the slant ranges and are denoted by $R_T(\tau)$ and $R_R(\tau)$ respectively. For simplicity, we have considered only one point target and is represented in receiver's coordinates $P(R_{0R}, \tau_{0R})$. The azimuth time when transmitter (or receiver) is at the closest distance from the point target, is also referred as the time at Point of Closest Approach (PCA) of the transmitter (or receiver) and is denoted as τ_{0T} (or τ_{0R}). The slant ranges at PCA of the transmitter and receiver are denoted by R_{0T} and R_{0R} respectively.

2.3 Bistatic SAR Signal Model

In bistatic SAR geometry, the slant range histories of transmitter and receiver can either be expressed in transmitter related or receiver related coordinates. In our approach, we specify the position of a PT at time instant τ_{0R}, when it is at PCA of the receiver at a slant range R_{0R}. Similarly, transmitter related coordinates can also be used for general bistatic SAR configurations. The choice of coordinates also depends on the bistatic SAR configuration or its application. For example, in case of a stationary transmitter (or receiver) and moving receiver (or transmitter) configurations, it is more appropriate to express the bistatic slant range histories in terms of the moving platform.

In bistatic SAR we have two carrier platforms. The angle between the lines joining the transmitter and receiver with the point target, keeping the point target in the center, is called the bistatic angle [shown in Figure 12]. The line joining transmitter and receiver is called the baseline and is denoted by $d(\tau)$.

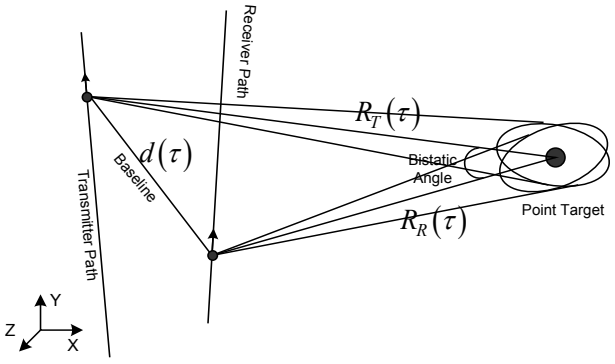

Figure 12: Bistatic SAR Imaging Model

We assume that both the platforms are moving with constant velocities along straight flight path. The slant range vectors of the receiver and transmitter at any azimuth time instant τ can be written as:

$$R_R\left(\tau, R_{0R}, \tau_{0R}\right) = \sqrt{R_R^2\left(\tau_{0R}, R_{0R}, \tau_{0R}\right) + v_R^2\left(\tau - \tau_{0R}\right)^2} \tag{2.1}$$

From Figure 13, it can be seen that the slant range R_{0R} at PCA of the receiver is perpendicular to the velocity vector $\vec{v}_R$.

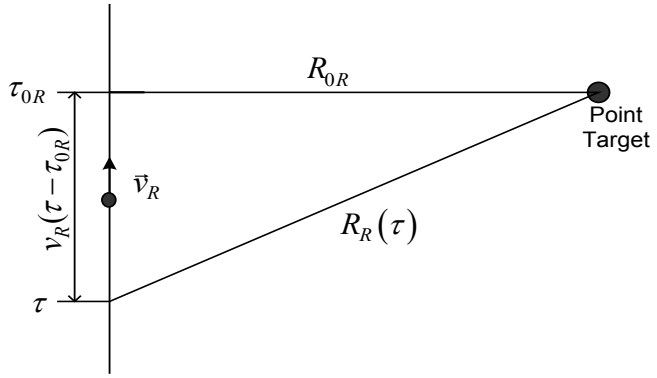

Figure 13: Slant Range Relationship

Similarly, the slant range equation for the transmitter will take the form as:

$$R_T\left(\tau, R_{0R}, \tau_{0R}\right) = \sqrt{R_T^2\left(\tau_{0T}, R_{0R}, \tau_{0R}\right) + v_T^2\left(\tau - \tau_{0T}\right)^2} \tag{2.2}$$

It depends on the azimuth time and velocity of the platform. The received signal is recorded coherently in range and azimuth directions. The bistatic slant range is sum of the transmitter and receiver slant ranges, which is in fact sum of two hyperbolic ranges. It is given as:

$$R_B\left(\tau, R_{0R}, \tau_{0R}\right) = R_T\left(\tau, R_{0R}, \tau_{0R}\right) + R_R\left(\tau, R_{0R}, \tau_{0R}\right) \tag{2.3}$$

The signal propagation time is denoted by t_0 and can be written as:

$$t_0\left(\tau, R_{0R}, \tau_{0R}\right) = \frac{R_T\left(\tau, R_{0R}, \tau_{0R}\right) + R_R\left(\tau, R_{0R}, \tau_{0R}\right)}{c_0} \tag{2.4}$$

The transmitter and the receiver should be synchronized. The phase stability of the local oscillator is important to have well focused images. For bistatic SAR configurations with large and rapidly changing baselines, synchronization of transmitter and receiver is not a trivial task and it may result in poorly focused images.

2.4 Bistatic Point Target Response

The transmitter emits pulses at regular Pulse Repetition Interval (PRI) during its flight. These pulses are up converted to a certain carrier frequency f_0 before transmission. The transmitted signal is usually a linear frequency modulated signal (e.g. chirp signal) with instantaneous frequency as a linear function of time. The received echo is down converted and sampled with a sampling rate greater than signal bandwidth B_r to avoid aliasing [83]. The received signal is considered as a time delayed replica of the transmitted signal. The received signal after demodulation to a base band signal for a point target response is given as:

$$g_l\left(t,\tau,R_{0R},\tau_{0R}\right)=\sigma\left(R_{0R},\tau_{0R}\right)w\left(\tau-\tau_c\right)s_l\left(t-t_0\right)e^{-j2\pi f_0 t_0} \tag{2.5}$$

Where, $\sigma\left(R_{0R},\tau_{0R}\right)$ is the backscattering coefficient. It provides information about the brightness of a point target. $w\left(\tau-\tau_c\right)$ is a rectangular window with center time τ_c. $s_l\left(t-t_0\right)$ is the delayed transmitted signal.

2.5 Bistatic Point Target Reference Spectrum

The received signal in equation (2.5) is represented in the time domain. After performing the Fourier transformation over the range time t and azimuth time τ, we get the point target spectrum in range frequency f and azimuth frequency f_τ domain.

After performing the Fourier transformation over range time t, on the received signal given in equation (2.5), we get:

$$G_l\left(f,\tau,R_{0R},\tau_{0R}\right)=\sigma\left(R_{0R},\tau_{0R}\right)w\left(\tau-\tau_c\right)S_l\left(f\right)e^{-j2\pi(f+f_0)t_0} \tag{2.6}$$

We substitute t_0 from equation (2.4) and perform the Fourier transformation over azimuth time τ. We obtain:

$$G_l\left(f,f_\tau,R_{0R},\tau_{0R}\right)=\sigma\left(R_{0R},\tau_{0R}\right)S_l\left(f\right) \int_{-\infty}^{\infty} w\left(\tau-\tau_c\right)e^{-j2\pi\left\{\frac{(f+f_0)}{c_0}\left[R_T\left(\tau,R_{0R},\tau_{0R}\right)+R_R\left(\tau,R_{0R},\tau_{0R}\right)\right]+f_\tau\tau\right\}}d\tau \tag{2.7}$$

Where, $G_l\left(f,f_\tau\right)$ is the received signal spectrum in frequency domain. The phase term in equation (2.7) is called as the bistatic phase term and is denoted by:

$$\phi_B = 2\pi\left\{\frac{(f+f_0)}{c_0}\left[R_T(\tau,R_{0R},\tau_{0R})+R_R(\tau,R_{0R},\tau_{0R})\right]+f_\tau\tau\right\} \tag{2.8}$$

The bistatic phase depends on the range and azimuth frequencies and the slant range histories of the transmitter and receiver. As both transmitter and receiver contribute to the bistatic phase, we can express it as the sum of transmitter and receiver phase terms.

$$\begin{aligned}\phi_T &= 2\pi\left\{\frac{(f+f_0)}{c_0}R_T(\tau,R_{0R},\tau_{0R})+f_{\tau T}\tau\right\}\\ \phi_R &= 2\pi\left\{\frac{(f+f_0)}{c_0}R_R(\tau,R_{0R},\tau_{0R})+f_{\tau R}\tau\right\}\end{aligned} \tag{2.9}$$

The weighted azimuth frequencies of the transmitter and receiver are defined as:

$$f_{\tau T} = \frac{\mu}{2}f_\tau \quad ; \quad f_{\tau R} = \frac{(2-\mu)}{2}f_\tau \tag{2.10}$$

Here, μ is the weighting factor which represents the unequal azimuth contribution of the transmitter and the receiver phases. In [1], equal azimuth contribution of the transmitter and receiver phases is considered i.e. $\mu = 1$. It works well for those bistatic SAR configurations where the transmitter and receiver both contribute equally towards the bistatic phase. But in certain configurations like hybrid configurations where the transmitter and receiver have large differences in the altitudes and velocities, we assume different azimuth contributions of the transmitter and receiver in the bistatic phase. An analytical expression for the weighting factor μ is derived in the next section. In every case, $f_{\tau T} + f_{\tau R} = f_\tau$ is satisfied.

The Method of Stationary Phase (MSP) has been used in the derivation of LBF [1]. The phase term in equation (2.7) oscillates very fast and most of the contribution of the integral comes from the vicinity of the stationary point. At the stationary point, the gradient of a function becomes zero [83]. The phase terms of the transmitter and receiver are expanded around their individual Points of Stationary Phases (PSP) $\tilde{\tau}_T, \tilde{\tau}_R$ using the Taylor's expansion. The second order Taylor's expansion of the transmitter and receiver phases is given as:

$$\begin{aligned}\phi_T &\simeq \phi_T(\tilde{\tau}_T)+\dot{\phi}_T(\tilde{\tau}_T)(\tau-\tilde{\tau}_T)+\frac{1}{2}\ddot{\phi}_T(\tilde{\tau}_T)(\tau-\tilde{\tau}_T)^2+\ldots\\ \phi_R &\simeq \phi_R(\tilde{\tau}_R)+\dot{\phi}_R(\tilde{\tau}_R)(\tau-\tilde{\tau}_R)+\frac{1}{2}\ddot{\phi}_R(\tilde{\tau}_R)(\tau-\tilde{\tau}_R)^2+\ldots\end{aligned} \tag{2.11}$$

The PSP of the transmitter and receiver are obtained using the following relations:

$$\left.\frac{d\phi_T}{d\tau}\right|_{\tau=\tilde{\tau}_T} = 0 \quad ; \qquad \left.\frac{d\phi_R}{d\tau}\right|_{\tau=\tilde{\tau}_R} = 0 \tag{2.12}$$

Simplifying equation (2.11) using equation (2.12), the bistatic phase term can be written as:

$$\phi_B \simeq \phi_T\left(\tilde{\tau}_T\right) + \phi_R\left(\tilde{\tau}_R\right) + \frac{1}{2}\ddot{\phi}_T\left(\tilde{\tau}_T\right)\left(\tau - \tilde{\tau}_T\right)^2 + \frac{1}{2}\ddot{\phi}_R\left(\tilde{\tau}_R\right)\left(\tau - \tilde{\tau}_R\right)^2 + \ldots \tag{2.13}$$

Substituting equation (2.13) into (2.7), and taking constant terms outside the integral, we get the following expression:

$$G_l\left(f, f_\tau, R_{0R}, \tau_{0R}\right) = \sigma\left(R_{0R}, \tau_{0R}\right) S_l\left(f\right) e^{-j\left[\phi_T\left(\tilde{\tau}_T\right) + \phi_R\left(\tilde{\tau}_R\right)\right]} \int_{-\infty}^{\infty} w\left(\tau - \tau_c\right) e^{-j\frac{1}{2}\left[\ddot{\phi}_T\left(\tilde{\tau}_T\right)\left(\tau - \tilde{\tau}_T\right)^2 + \ddot{\phi}_R\left(\tilde{\tau}_R\right)\left(\tau - \tilde{\tau}_R\right)^2\right]} d\tau \tag{2.14}$$

The phase term inside the integral is sum of two quadratic terms. As the sum of two quadratic terms remains quadratic, so they can be regrouped and expanded around a common PSP. Let the phase terms of the integral be denoted by:

$$\phi_S\left(\tau\right) = \ddot{\phi}_T\left(\tilde{\tau}_T\right)\left(\tau - \tilde{\tau}_T\right)^2 + \ddot{\phi}_R\left(\tilde{\tau}_R\right)\left(\tau - \tilde{\tau}_R\right)^2 \tag{2.15}$$

The common PSP $\tilde{\tau}$ is obtained as follows:

$$\left.\frac{d\phi_S}{d\tau}\right|_{\tau=\tilde{\tau}} = 0 \qquad \Rightarrow \qquad \tilde{\tau} = \frac{\ddot{\phi}_T\left(\tilde{\tau}_T\right)\tilde{\tau}_T + \ddot{\phi}_R\left(\tilde{\tau}_R\right)\tilde{\tau}_R}{\ddot{\phi}_T\left(\tilde{\tau}_T\right) + \ddot{\phi}_R\left(\tilde{\tau}_R\right)} \tag{2.16}$$

The phase term given in equation (2.15) is expanded using the second order Taylor's expansion and we get:

$$\phi_S\left(\tau\right) \simeq \phi_S\left(\tilde{\tau}\right) + \frac{1}{2}\ddot{\phi}_S\left(\tilde{\tau}\right)\left(\tau - \tilde{\tau}\right)^2 + \ldots \tag{2.17}$$

Using equations (2.15) and (2.16), we can simplify equation (2.17) as:

$$\phi_S\left(\tau\right) = \frac{\ddot{\phi}_T\left(\tilde{\tau}_T\right)\ddot{\phi}_R\left(\tilde{\tau}_R\right)}{\ddot{\phi}_T\left(\tilde{\tau}_T\right) + \ddot{\phi}_R\left(\tilde{\tau}_R\right)}\left(\tilde{\tau}_R - \tilde{\tau}_T\right)^2 + \left[\ddot{\phi}_T\left(\tilde{\tau}_T\right) + \ddot{\phi}_R\left(\tilde{\tau}_R\right)\right]\left(\tau - \tilde{\tau}\right)^2 \tag{2.18}$$

The phase term of equation (2.18) is substituted into (2.14). After simplifications, we obtain the BPTRS as follows:

$$G_l\left(f,f_\tau,R_{0R},\tau_{0R}\right)=\sigma\left(R_{0R},\tau_{0R}\right)S_l\left(f\right)w\left(\tilde{\tau}-\tau_{cb}\right)\frac{\sqrt{2\pi}}{\sqrt{\ddot{\phi}_T\left(\tilde{\tau}_T\right)+\ddot{\phi}_R\left(\tilde{\tau}_R\right)}} \tag{2.19}$$
$$e^{-j\frac{\pi}{4}}e^{-j\Psi_{QM}}e^{-\frac{j}{2}\Psi_{BD}}$$

The first phase term in equation (2.19) is called as the Quasi Monostatic (QM) term and the second term is called as the Bistatic Deformation (BD) term. These phase terms are expressed as follows:

$$\Psi_{QM}=\phi_T(\tilde{\tau}_T)+\phi_R(\tilde{\tau}_R)\quad;\quad\Psi_{BD}=\frac{\ddot{\phi}_T\left(\tilde{\tau}_T\right)\ddot{\phi}_R\left(\tilde{\tau}_R\right)}{\ddot{\phi}_T\left(\tilde{\tau}_T\right)+\ddot{\phi}_R\left(\tilde{\tau}_R\right)}\left(\tilde{\tau}_T-\tilde{\tau}_R\right)^2 \tag{2.20}$$

The transmitter and the receiver phase terms can be simplified mathematically. The expanded derivations of these results are given in Appendix A. The second order derivatives of the phase terms at the individual PSP of the transmitter and receiver are simplified as:

$$\ddot{\phi}_T\left(\tilde{\tau}_T\right)=\frac{2\pi v_T^2}{c_0R_{0T}}\frac{\operatorname{sgn}\left(f+f_0\right)}{\left(f+f_0\right)^2}F_T^{3/2}\left(f,f_\tau\right) \tag{2.21}$$
$$\ddot{\phi}_R\left(\tilde{\tau}_R\right)=\frac{2\pi v_R^2}{c_0R_{0R}}\frac{\operatorname{sgn}\left(f+f_0\right)}{\left(f+f_0\right)^2}F_R^{3/2}\left(f,f_\tau\right)$$

Where, F_T,F_R represent frequency histories and are given as:

$$F_T\left(f,f_\tau\right)=\left(f+f_0\right)^2-\frac{\mu^2f_\tau^2c_0^2}{4v_T^2} \tag{2.22}$$
$$F_R\left(f,f_\tau\right)=\left(f+f_0\right)^2-\frac{(2-\mu)^2f_\tau^2c_0^2}{4v_R^2}$$

The individual PSP of the transmitter and the receiver are obtained as below:

$$\tilde{\tau}_T=\tau_{0T}-\frac{\mu f_\tau c_0}{2v_T^2}\frac{R_{0T}\operatorname{sgn}\left(f+f_0\right)}{F_T^{1/2}\left(f,f_\tau\right)} \tag{2.23}$$
$$\tilde{\tau}_R=\tau_{0R}-\frac{(2-\mu)f_\tau c_0}{2v_R^2}\frac{R_{0R}\operatorname{sgn}\left(f+f_0\right)}{F_R^{1/2}\left(f,f_\tau\right)}$$

The common PSP is derived as follows:

$$\tilde{\tau}=\frac{v_T^2F_T^{3/2}\left(\tau_{0R}+a_0\right)+a_2\tau_{0R}v_R^2F_R^{3/2}-c_0a_2R_{0R}f_\tau\left(\mu F_T+(2-\mu)F_R\right)/2}{v_T^2F_T^{3/2}+a_2v_R^2F_R^{3/2}} \tag{2.24}$$

Here a_0, a_2 are called the system parameters. a_0 is the azimuth time difference of the transmitter and receiver at PCA. Whereas, a_2 is the slant range ratio of the transmitter and receiver at PCA and are given as:

$$a_0 = \tau_{0T} - \tau_{0R} \quad ; \quad a_2 = \frac{R_{0T}}{R_{0R}} \tag{2.25}$$

The QM and BD phase terms given in equation (2.20) are simplified as follows:

$$\Psi_{QM} = \pi f_\tau \left(2\tau_{0R} + \mu a_0\right) + \frac{2\pi R_{0R}\,\mathrm{sgn}\left(f+f_0\right)}{c_0}\left(F_R^{1/2} + a_2 F_T^{1/2}\right) \tag{2.26}$$

$$\Psi_{BD} = \frac{2\pi v_T^2 v_R^2}{R_{0R} c_0}\frac{\mathrm{sgn}\left(f+f_0\right)}{\left(f+f_0\right)^2}\frac{F_R^{3/2}F_T^{3/2}}{F_T^{3/2}v_T^2 + a_2 v_R^2 F_R^{3/2}}$$
$$\left[a_0 - \frac{f_\tau c_0 R_{0R}\,\mathrm{sgn}(f+f_0)}{2v_T^2 v_R^2}\left(\frac{\mu a_2 v_R^2}{F_T^{1/2}} - \frac{(2-\mu)v_T^2}{F_R^{1/2}}\right)\right]^2$$

The two dimensional BPTRS based on the LBF for unequal azimuth contribution of the transmitter and receiver phase terms is given in equation (2.19), can be simplified using the equations (2.21) - (2.26). This BPTRS is essential for the development of the bistatic SAR processing algorithm.

2.6 Optimum Weighting Factor

In the final expression of BPTRS, all parameters except the weighting factor μ are known. The next step is to derive an analytical expression for the weighting factor. We know that the MSP has been used in the derivation of LBF [1]. It is only applicable if the common PSP $\tilde{\tau}$ is located in the vicinity of the individual PSPs of the transmitter $\tilde{\tau}_T$ and the receiver $\tilde{\tau}_R$. Also, the individual PSPs of transmitter and receiver should not be too far apart.

Based on the above mentioned facts, we come up with an idea that the weighting factor can be obtained by minimizing the square difference between the individual PSPs of the transmitter and receiver, and is given as:

$$\frac{d}{d\mu}\left(\tilde{\tau}_T - \tilde{\tau}_R\right)^2 = 0 \tag{2.27}$$

Simplifying the above equation, we get:

$$2\left(\tilde{\tau}_T - \tilde{\tau}_R\right)\left[\frac{d\tilde{\tau}_T}{d\mu} - \frac{d\tilde{\tau}_R}{d\mu}\right] = 0 \tag{2.28}$$

Derivation of individual PSPs of the transmitter and receiver with respect to the weighting factor μ can be obtained using equation (2.23) as:

$$\frac{d\tilde{\tau}_T}{d\mu} = -\frac{f_\tau c_0}{2v_T^2}\frac{R_{0T}}{(f+f_0)} \qquad (2.29)$$
$$\frac{d\tilde{\tau}_R}{d\mu} = \frac{f_\tau c_0}{2v_R^2}\frac{R_{0R}}{(f+f_0)}$$

The frequency histories of the transmitter and receiver given in equation (2.22) are approximated as:

$$F_T(f, f_\tau) \simeq (f+f_0)^2 \qquad (2.30)$$
$$F_R(f, f_\tau) \simeq (f+f_0)^2$$

Substituting equations (2.23) and (2.29) into (2.28), we get:

$$2\left\{\left(\tau_{0T} - \frac{\mu f_\tau c_0}{2v_T^2}\frac{R_{0T}}{(f+f_0)}\right) - \left(\tau_{0R} - \frac{(2-\mu) f_\tau c_0}{2v_R^2}\frac{R_{0R}}{(f+f_0)}\right)\right\} \qquad (2.31)$$
$$\left[-\frac{f_\tau c_0}{2v_T^2}\frac{R_{0T}}{(f+f_0)} - \frac{f_\tau c_0}{2v_R^2}\frac{R_{0R}}{(f+f_0)}\right] = 0$$

After simplifying the above equation, we get weighting factor μ as follows:

$$\mu = \frac{2(f+f_0)}{f_\tau c_0}\frac{v_T^2 v_R^2}{\left(R_{0T}v_R^2 + R_{0R}v_T^2\right)}\left[\frac{f_\tau c_0 R_{0R}}{v_R^2(f+f_0)} + a_0\right] \qquad (2.32)$$
$$= \frac{2v_T^2}{\left(a_2 v_R^2 + v_T^2\right)}\left[1 + \frac{a_0 v_R^2 (f+f_0)}{f_\tau c_0 R_{0R}}\right]$$

The above equation shows that the weighting factor μ depends upon the range and azimuth frequencies, the platform velocities, slant ranges and azimuth time of the transmitter and receiver at PCA.

2.6.1 Simulation Results

An analytical solution for the weighting factor μ is obtained by using the fact that MSP can only remain valid if we have a single PSP. Therefore, the difference between the individual PSPs of the transmitter and receiver should remain as small as possible, i.e. $(\tilde{\tau}_T - \tilde{\tau}_R) \to 0$. We plot the difference between the individual PSPs of the transmitter and receiver for hybrid (spaceborne/airborne) configuration, using the parameters given in Table 1.

Table 1: Parameters for Hybrid Configuration

Parameters	**Transmitter**	**Receiver**
Velocity	7600 m/s	100 m/s
Pulse duration	3 μs	
Carrier frequency	9.65 GHz	
Bandwidth	150 MHz	
PRF	4000 Hz	
Beam width (azimuth)	0.33°	2.9°
Altitude	514 km	3000 m

In [46], Time Bandwidth Product (TBP) is used to give different weighting to azimuth contributions of the transmitter and receiver phase terms. For our simulations, we consider three cases:

Case 1: Assume equal azimuth contributions of the transmitter and receiver phases, i.e. $\mu = 1$ (Original LBF).

Case 2: Consider TBP [46] as the weighting factor.

Case 3: Use the weighting factor obtained in equation (2.32).

In Figure 14, the difference between the individual PSPs of the transmitter and receiver are plotted against range and azimuth frequencies, for the three above mentioned cases, using the parameters of Table 1.

Case 1:

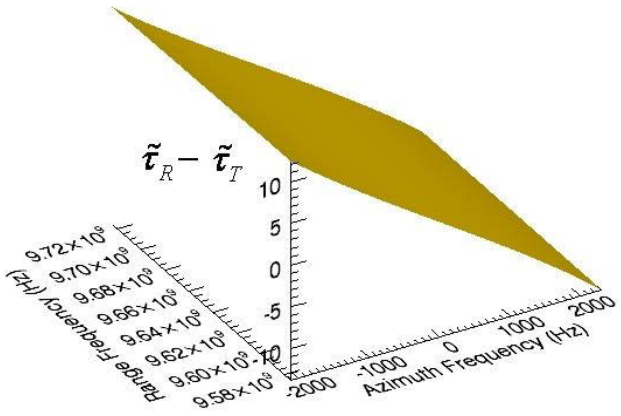

Case 2:

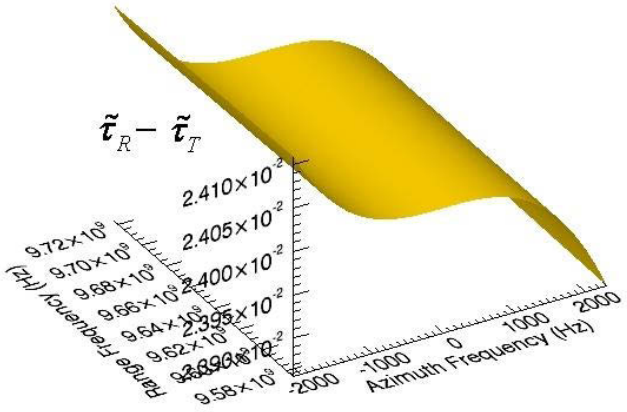

Case 3:

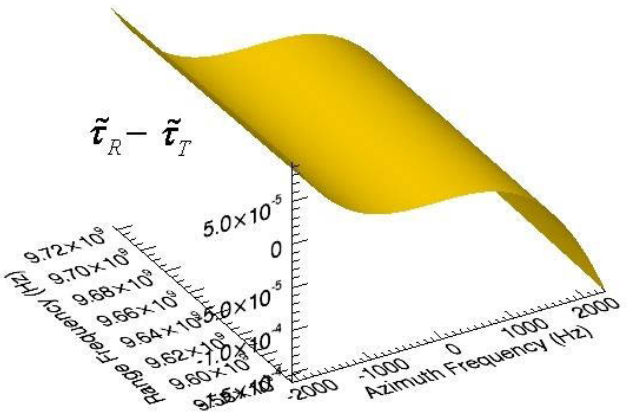

Figure 14: Difference between the Individual PSPs of the Transmitter and the Receiver

In Figure 14, comparing case 1 with cases 2 and 3, we conclude that the difference between the individual PSPs of the transmitter and receiver is considerably decreased by using weighted azimuth contributions of the transmitter and receiver phase terms. Individual PSPs came closer to each other in case 3 as compared to case 2. Hence, we can say that weighting factor obtained by minimizing square difference between individual PSPs of the transmitter and receiver is optimum as compared to TBP.

2.6.2 Difference between Common and Individual Point of Stationary Phase of the Transmitter

Another approach is to minimize the difference between common and individual PSP of the transmitter. We get the weighting factor μ by minimizing the square difference between common and the transmitter's PSP and is given as:

$$\frac{d}{d\mu}\left(\tilde{\tau} - \tilde{\tau}_T\right)^2 = 0 \tag{2.33}$$

Simplifying the above equation we get:

$$2\left(\tilde{\tau}-\tilde{\tau}_T\right)\left[\frac{d\tilde{\tau}}{d\mu}-\frac{d\tilde{\tau}_T}{d\mu}\right]=0 \tag{2.34}$$

Using equations (2.23), (2.24) and the approximation given in equation (2.30), we can further simplify equation (2.34) as follows:

$$2\left\{\left(\frac{1}{\left(v_T^2+a_2v_R^2\right)}\left[\left(v_T^2\tau_{0T}+a_2\tau_{0R}v_R^2\right)-\frac{c_0R_{0T}f_\tau}{\left(f+f_0\right)}\right]\right)-\left\{\left[\frac{f_\tau c_0R_{0T}}{2v_T^2\left(f+f_0\right)}\right]=0\right.\right. \tag{2.35}$$
$$\left.\left.\left(\tau_{0T}-\frac{f_\tau c_0\mu}{2v_T^2}\frac{R_{0T}}{\left(f+f_0\right)}\right)\right.\right.$$

Simplifying the above equation for weighting factor μ we obtain:

$$\mu=\frac{2v_T^2\left(f+f_0\right)}{R_{0T}f_\tau c_0}\left[\frac{R_{0T}f_\tau c_0}{\left(f+f_0\right)\left(v_T^2+a_2v_R^2\right)}+\frac{a_0v_R^2a_2}{v_T^2+a_2v_R^2}\right] \tag{2.36}$$
$$=\frac{2v_T^2}{\left(v_T^2+a_2v_R^2\right)}\left[1+\frac{a_0v_R^2\left(f+f_0\right)}{f_\tau c_0R_{0R}}\right]$$

We have reached to the same result as obtained in equation (2.32). The difference between common and transmitter's PSP $\left(\tilde{\tau}_T-\tilde{\tau}\right)$, is plotted for the hybrid configurations using the parameters given in Table 1. We consider three cases mentioned in section 2.6.1.

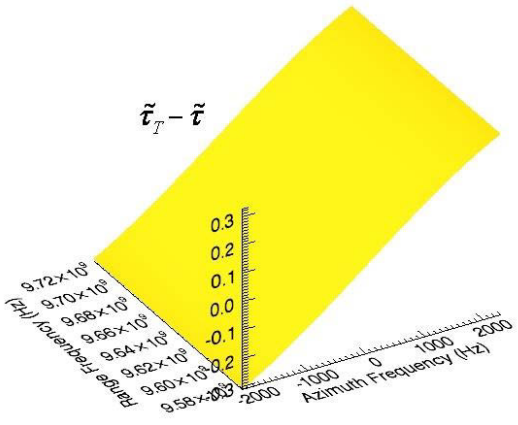

Case 1:

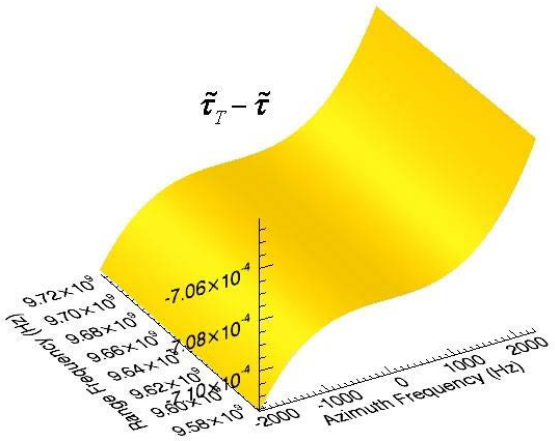

Case 2:

Case 3:

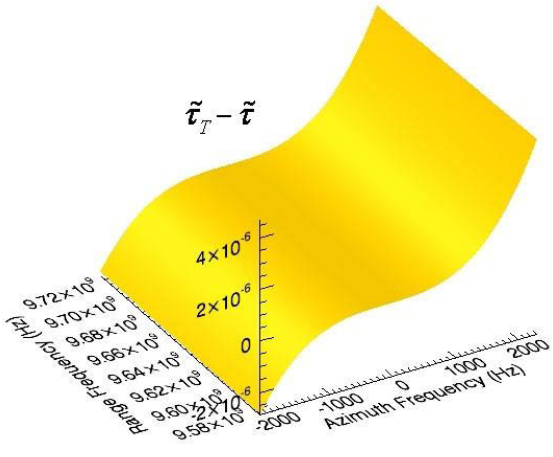

Figure 15: Difference between Common and Individual PSP of the Transmitter

These three cases are plotted in Figure 15 and we observe that the common and individual PSP of the transmitter came closer to each other in case 2 and 3 as compared to the case 1. Also, case 3 gave better results as compared to the case 2.

2.6.3 Difference between Common and Individual Point of Stationary Phase of the Receiver

It would also be interesting to compare difference between common and individual PSP of the receiver. We minimize the square difference between the common and the receiver's PSP and is given as:

$$\frac{d}{d\mu}\left(\tilde{\tau}-\tilde{\tau}_R\right)^2 = 0 \tag{2.37}$$

Simplifying the above equation we get:

$$2\left(\tilde{\tau}-\tilde{\tau}_R\right)\left[\frac{d\tilde{\tau}}{d\mu}-\frac{d\tilde{\tau}_R}{d\mu}\right] = 0 \tag{2.38}$$

Using equations (2.23), (2.24) and the approximation given in equation (2.30), we can further simplify equation (2.38) as follows:

$$2\left\{\left(\frac{1}{\left(v_T^2+a_2v_R^2\right)}\left[\left(v_T^2\tau_{0T}+a_2\tau_{0R}v_R^2\right)-\frac{c_0R_{0T}f_\tau}{\left(f+f_0\right)}\right]\right)-\left(\tau_{0R}-\frac{f_\tau c_0(2-\mu)}{2v_R^2}\frac{R_{0R}}{\left(f+f_0\right)}\right)\right\}\left[-\frac{f_\tau c_0R_{0R}}{2v_R^2\left(f+f_0\right)}\right]=0 \tag{2.39}$$

Now simplifying the above equation for weighting factor μ we get:

$$\mu = \frac{2v_R^2(f+f_0)}{f_\tau c_0 R_{0R}}\left[\frac{v_T^2(\tau_{0T}-\tau_{0R})}{v_T^2+a_2v_R^2} - \frac{f_\tau c_0 R_{0T}}{(f+f_0)\left(v_T^2+a_2v_R^2\right)} + \frac{f_\tau c_0 R_{0R}}{v_R^2(f+f_0)}\right] \tag{2.40}$$

$$= \frac{2}{\left(v_T^2+a_2v_R^2\right)}\left[\frac{v_T^2 a_0 v_R^2(f+f_0)}{f_\tau c_0 R_{0R}} - \frac{v_R^2 R_{0T}}{R_{0R}} + v_T^2 + a_2 v_R^2\right]$$

$$= \frac{2v_T^2}{\left(v_T^2+a_2v_R^2\right)}\left[1+\frac{a_0 v_R^2(f+f_0)}{f_\tau c_0 R_{0R}}\right]$$

In this case, we have obtained a similar expression as in the equations (2.32) and (2.36). Here, we can say that by minimizing the square difference between common and individual PSPs of the transmitter or receiver or by minimizing the square difference between individual PSPs of the transmitter and receiver, we get similar expression for the weighting factor μ.

Now, we plot the difference between common and receiver's PSP $\left(\tilde{\tau}_R - \tilde{\tau}\right)$, for hybrid configurations using the parameters given in Table 1. We again consider three different cases of section 2.6.1.

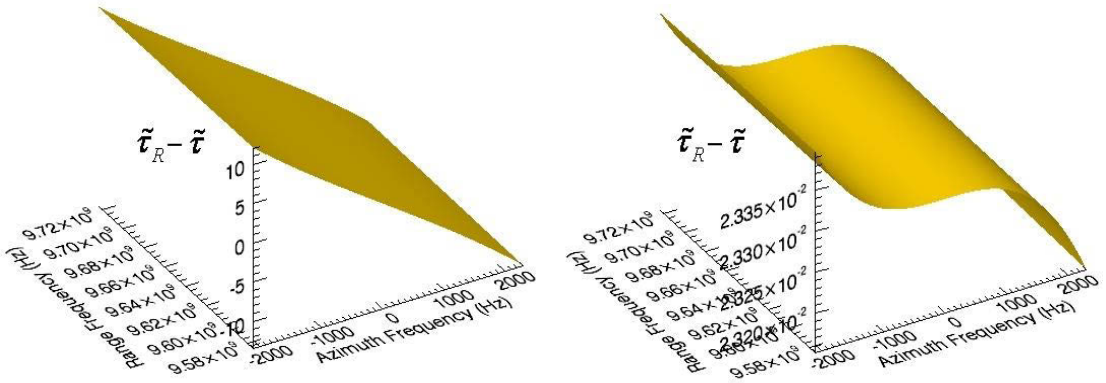

Case 1: Case 2:

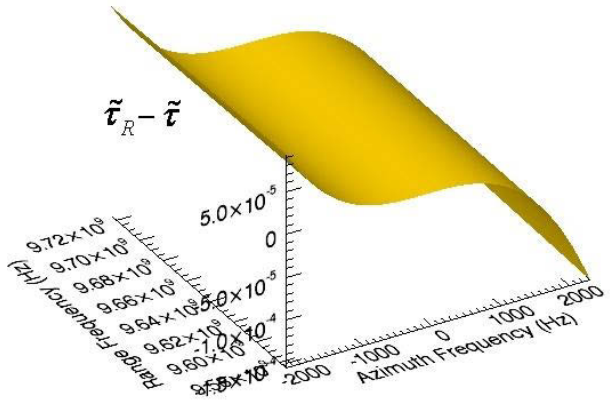

Case 3:

Figure 16: Difference between Common and Individual PSP of the Receiver

In Figure 16, we can see that the difference between the common and individual PSP of the receiver became smaller in cases 2 and 3 as compare to the case 1.

2.6.4 Comparison of Time Bandwidth Product and Weighting Factor μ

In this section, we draw a comparison between the weighting introduced using TBP and by minimizing the square difference between the common and the individual PSPs of the transmitter or receiver. In [46], the weighted azimuth frequencies are defined as:

$$f_{\tau T\_TBP} = k_T f_\tau \quad ; \quad f_{\tau R\_TBP} = k_R f_\tau \tag{2.41}$$

Where, k_T, k_R are TBP ratios of the transmitter and receiver respectively. They are defined as ratio of transmitter/receiver TBP to the sum of transmitter's and receiver's TBP and are given as:

$$\begin{aligned} k_T &= \frac{TBP_T}{TBP_T + TBP_R} = \frac{\left(v_T^2/\lambda R_{0T}\right)T_A^2}{\left(v_T^2/\lambda R_{0T}\right)T_A^2 + \left(v_R^2/\lambda R_{0R}\right)T_A^2} \\ k_R &= \frac{TBP_R}{TBP_T + TBP_R} = \frac{\left(v_R^2/\lambda R_{0R}\right)T_A^2}{\left(v_T^2/\lambda R_{0T}\right)T_A^2 + \left(v_R^2/\lambda R_{0R}\right)T_A^2} \end{aligned} \tag{2.42}$$

Where, T_A is the composite synthetic aperture time. Using the above equation, we can write equation (2.41) as follows:

$$\begin{aligned} f_{\tau T\_TBP} &= \frac{v_T^2}{v_T^2 + v_R^2 a_2} f_\tau \\ f_{\tau R\_TBP} &= \frac{v_R^2}{v_R^2 + v_T^2/a_2} f_\tau \end{aligned} \tag{2.43}$$

Later on these weighted azimuth frequencies are modified in [51] and residual Doppler shift of transmitter and receiver are included and is given as:

$$\begin{aligned} f_{\tau T\_TBP_T} &= k_T f_\tau - k_T\left(f_{DCr} + f_{DCt}\right) + f_{DCt} \\ f_{\tau R\_TBP_R} &= k_R f_\tau - k_R\left(f_{DCr} + f_{DCt}\right) + f_{DCr} \end{aligned} \tag{2.44}$$

The Doppler centroid of the transmitter and receiver are defined as follows:

$$\begin{aligned} f_{DCt} &= \frac{v_T}{\lambda}\sin\theta_{SQt} \\ f_{DCr} &= \frac{v_R}{\lambda}\sin\theta_{SQr} \end{aligned} \tag{2.45}$$

Where, θ_{SQt} and θ_{SQr} are squint angles of the transmitter and receiver respectively. Squint angles can be simplified from geometry given in Figure 17, as follows:

$$\sin\theta_{SQt} = \frac{v_T\left(\tau_{0T}-\tau\right)}{R_T\left(\tau\right)} = \frac{v_T\left(\tau_{0T}-\tau\right)}{\sqrt{R_{0T}^2 + v_T^2\left(\tau_{0T}-\tau\right)^2}} \tag{2.46}$$

$$as,\ v_T^2\left(\tau_{0T}-\tau\right)^2 \ll R_{0T}^2$$

$$\sin\theta_{SQt} \simeq \frac{v_T\left(\tau_{0T}-\tau\right)}{R_{0T}}$$

$$\sin\theta_{SQr} \simeq \frac{v_R\left(\tau_{0R}-\tau\right)}{R_{0R}}$$

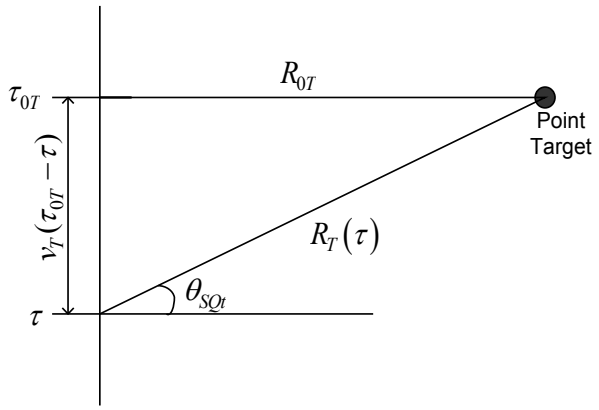

Figure 17: Squint Angle Geometry

Doppler centroid of the transmitter and receiver are simplified using (2.46), as:

$$f_{DCt} = \frac{v_T^2\left(\tau_{0T}-\tau\right)}{\lambda R_{0T}} \tag{2.47}$$

$$f_{DCr} = \frac{v_R^2\left(\tau_{0R}-\tau\right)}{\lambda R_{0R}}$$

Weighted azimuth frequency of the transmitter in equation (2.44), can be simplified using equations (2.42) - (2.47), we get:

$$f_{\tau T\_TBP_T} = \frac{v_T^2/R_{0T}}{v_T^2/R_{0T} + v_R^2/R_{0R}} f_\tau - \frac{v_T^2/R_{0T}}{v_T^2/R_{0T} + v_R^2/R_{0R}} \frac{v_R^2\left(\tau_{0R}-\tau\right)}{\lambda R_{0R}} + \left[1 - \frac{v_T^2/R_{0T}}{v_T^2/R_{0T} + v_R^2/R_{0R}}\right] \frac{v_T^2\left(\tau_{0T}-\tau\right)}{\lambda R_{0T}} \tag{2.48}$$

Simplifying the above equation we get:

$$
\begin{aligned}
f_{\tau T\_TBP_T} &= \frac{v_T^2/R_{0T}}{v_T^2/R_{0T}+v_R^2/R_{0R}} f_\tau + \frac{v_T^2 v_R^2\left(\tau_{0T}-\tau_{0R}\right)}{\left[v_T^2/R_{0T}+v_R^2/R_{0R}\right]\lambda R_{0T}R_{0R}} \\
&= \frac{v_T^2/R_{0T}}{v_T^2/R_{0T}+v_R^2/R_{0R}}\left[f_\tau + \frac{v_R^2 a_0}{\lambda R_{0R}}\right] \\
&= \frac{v_T^2}{v_T^2+a_2 v_R^2}\left[f_\tau + \frac{a_0\left(f+f_0\right)v_R^2}{c_0 R_{0R}}\right]
\end{aligned}
\tag{2.49}
$$

The above weighted azimuth frequency is obtained using TBP and the residual Doppler shift for the transmitter. Now, we compare it with the weighted azimuth frequency obtained by minimizing square difference between common and individual PSP. Using equations (2.10) and (2.32), we can write:

$$
f_{\tau T} = \frac{v_T^2}{\left(a_2 v_R^2 + v_T^2\right)}\left[f_\tau + \frac{a_0 v_R^2\left(f+f_0\right)}{c_0 R_{0R}}\right] \tag{2.50}
$$

Comparing equations (2.49) and (2.50), we conclude that the modified time bandwidth approach along with residual Doppler shift for transmitter and receiver is similar to our approach. Hence, we can say that mathematically, weighting factor and modified TBP approaches are identical.

2.7 Conclusions

In this chapter, we have derived the BPTRS based on LBF, using different azimuth contributions of the transmitter and receiver phase terms. We considered a general bistatic SAR configuration and used the MSP in the derivation of BPTRS. The phases of transmitter and receiver are expanded using the second order Taylor expansion around their individual PSPs. And a final expression of BPTRS is derived which depends on the weighted azimuth contributions of the transmitter and receiver phase terms.

The weighting factor is derived by minimizing the square difference between the individual points of stationary phases of the transmitter and receiver. The simulations are carried out for the hybrid bistatic SAR configurations. The simulation results show that the weighting factor minimizes the difference between the common and the individual PSPs of the transmitter and receiver, as compared to the original LBF and TBP. In the end a comparison of the weighting factor with modified TBP is provided.

3 Validity Constraints

3.1 Introduction

Our approach is based on the BPTRS [1]. It consists of two phase terms, quasi monostatic and bistatic deformation phase terms. The method of stationary phase has been used in the derivation of LBF. The phase terms of the transmitter and receiver are expanded using second order Taylor's series around their individual points of stationary phases. This approach yields an expression with a sum of two quadratic terms. As sum of two quadratic terms remain quadratic, we can express sum of transmitter and receiver phase terms as a second order Taylor expansion around a common bistatic stationary point.

In this chapter four validity constraints are derived based on LBF. These constraints are very important in planning a bistatic SAR mission. They are used to validate BPTRS for different bistatic SAR configurations. This chapter is structured as follows: In section 3.2, four validity constraints, two each for the transmitter and the receiver are derived. Their performance for different bistatic SAR configurations is observed in section 3.3. Simulations are carried out to analyze their performance. Also, some considerations based on validity constraints for spaceborne/airborne configuration are provided in section 3.4. Finally, they are analyzed to determine unequal azimuth contributions of the transmitter and receiver phase terms in section 3.5. Conclusions are provided in the last section.

3.2 Derivation of Validity Constraints for Bistatic Point Target Reference Spectrum

Some initial work for the derivation of validity constraints has been done in [1]. In the derivation of BPTRS [1], transmitter and receiver phases are expanded using Taylor's series till second order, higher order terms were neglected. Validity constraints are derived to minimize the error introduced by neglecting the higher order phase terms. A fourth order Taylor's expansion of transmitter and receiver slant range is given as follows:

$$
\begin{aligned}
R_T(\tau) &= R_T(\tilde{\tau}_T) + \dot{R}_T(\tilde{\tau}_T)(\tau-\tilde{\tau}_T) + \frac{1}{2!}\ddot{R}_T(\tilde{\tau}_T)(\tau-\tilde{\tau}_T)^2 + \\
&\quad \frac{1}{3!}\dddot{R}_T(\tilde{\tau}_T)(\tau-\tilde{\tau}_T)^3 + \frac{1}{4!}\ddddot{R}_T(\xi_T)(\tau-\tilde{\tau}_T)^4 \\
R_R(\tau) &= R_R(\tilde{\tau}_R) + \dot{R}_R(\tilde{\tau}_R)(\tau-\tilde{\tau}_R) + \frac{1}{2!}\ddot{R}_R(\tilde{\tau}_R)(\tau-\tilde{\tau}_R)^2 + \\
&\quad \frac{1}{3!}\dddot{R}_R(\tilde{\tau}_R)(\tau-\tilde{\tau}_R)^3 + \frac{1}{4!}\ddddot{R}_R(\xi_R)(\tau-\tilde{\tau}_R)^4
\end{aligned}
\tag{3.1}
$$

The last terms in the above equations are Lagrange forms of remainder and according to the mean value theorem they sum up higher order terms, ξ_T and ξ_R lie with the intervals $[\tilde{\tau}_T, \tau]$ and $[\tilde{\tau}_R, \tau]$, respectively. The range rate errors of equation (3.1) are given as:

$$
\begin{aligned}
E_T(\tau) &= \frac{1}{2!}\dddot{R}_T(\tilde{\tau}_T)(\tau-\tilde{\tau}_T)^2 + \frac{1}{3!}\ddddot{R}_T(\xi_T)(\tau-\tilde{\tau}_T)^3 \\
E_R(\tau) &= \frac{1}{2!}\dddot{R}_R(\tilde{\tau}_R)(\tau-\tilde{\tau}_R)^2 + \frac{1}{3!}\ddddot{R}_R(\xi_R)(\tau-\tilde{\tau}_R)^3
\end{aligned}
\tag{3.2}
$$

The higher order terms of Taylor's expansion can be neglected if the range rate errors are negligible against their nominal values. The range rate errors at the common point of stationary phase against their nominal values can be written as:

$$
\begin{aligned}
\left|\frac{1}{2!}\dddot{R}_T(\tilde{\tau}_T)(\tilde{\tau}-\tilde{\tau}_T) + \frac{1}{3!}\ddddot{R}_T(\xi_T)(\tilde{\tau}-\tilde{\tau}_T)^2\right| &<< \left|\ddot{R}_T(\tilde{\tau}_T)\right| \\
\left|\frac{1}{2!}\dddot{R}_R(\tilde{\tau}_R)(\tilde{\tau}-\tilde{\tau}_R) + \frac{1}{3!}\ddddot{R}_R(\xi_R)(\tilde{\tau}-\tilde{\tau}_R)^2\right| &<< \left|\ddot{R}_R(\tilde{\tau}_R)\right|
\end{aligned}
\tag{3.3}
$$

Above equation holds if,

$$
\left|\frac{\frac{1}{2!}\dddot{R}_T(\tilde{\tau}_T)(\tilde{\tau}-\tilde{\tau}_T)}{\ddot{R}_T(\tilde{\tau}_T)}\right| << 1 \quad ; \quad \left|\frac{\frac{1}{2!}\dddot{R}_R(\tilde{\tau}_R)(\tilde{\tau}-\tilde{\tau}_R)}{\ddot{R}_R(\tilde{\tau}_R)}\right| << 1
\tag{3.4}
$$

and if,

$$
\left|\frac{\frac{1}{3!}\ddddot{R}_T(\xi_T)(\tilde{\tau}-\tilde{\tau}_T)^2}{\ddot{R}_T(\tilde{\tau}_T)}\right| << 1 \quad ; \quad \left|\frac{\frac{1}{3!}\ddddot{R}_R(\xi_R)(\tilde{\tau}-\tilde{\tau}_R)^2}{\ddot{R}_R(\tilde{\tau}_R)}\right| << 1
\tag{3.5}
$$

If the conditions mentioned in equation (3.4) and (3.3) are fulfilled then the higher order terms can be neglected. Equation (3.4) and (3.5) will give two constraints for the transmitter and two constraints for the receiver. To simplify these equations we need second, third and fourth order derivatives of transmitter and receiver slant ranges at their indi-

vidual points of stationary phases. The first and second order derivatives of slant ranges at their individual points of stationary phases are derived in Appendix A. Equations (A.16) and (A.17) give first and second order derivatives of the receiver's slant range at its stationary point $\tilde{\tau}_R$. Equations (A.26) and (A.40) provide first and second order derivatives of the transmitter's slant ranges at its stationary point $\tilde{\tau}_T$. We now consider the receiver's case; second, third and fourth order derivatives of the receiver's slant range are obtained by differentiating equation (A.6).

$$\begin{aligned} &\dot{R}_R^2(\tau)+\ddot{R}_R(\tau)R_R(\tau)=v_R^2 \\ &3\dot{R}_R(\tau)\ddot{R}_R(\tau)+R_R(\tau)\dddot{R}_R(\tau)=0 \\ &3\ddot{R}_R^2(\tau)+R_R(\tau)\ddddot{R}_R(\tau)+4\dot{R}_R(\tau)\dddot{R}_R(\tau)=0 \end{aligned} \tag{3.6}$$

The second order derivative of the receiver's slant range at stationary point of receiver $\tilde{\tau}_R$ is given in equation (A.8), which is further simplified using equation (A.12) and we get:

$$\begin{aligned} \ddot{R}_R(\tilde{\tau}_R,R_{0R},\tau_{0R}) &= \frac{v_R^2}{R_R(\tilde{\tau}_R,R_{0R},\tau_{0R})}-\frac{v_R^4(\tilde{\tau}_R-\tau_{0R})^2}{R_R^3(\tilde{\tau}_R,R_{0R},\tau_{0R})} \\ &= \frac{v_R^2}{R_R(\tilde{\tau}_R,R_{0R},\tau_{0R})}\left(1-\frac{R_R^2(\tilde{\tau}_R,R_{0R},\tau_{0R})-R_{0R}^2}{R_R^2(\tilde{\tau}_R,R_{0R},\tau_{0R})}\right) \\ &= \frac{v_R^2R_{0R}^2}{R_R^3(\tilde{\tau}_R,R_{0R},\tau_{0R})} \end{aligned} \tag{3.7}$$

Similarly, the third order derivative of the receiver's slant range can be obtained from equation (3.6) as:

$$\dddot{R}_R(\tau)=-\frac{3\dot{R}_R(\tau)\ddot{R}_R(\tau)}{R_R(\tau)} \tag{3.8}$$

The above equation is simplified using equations (A.6), (A.8) and (A.12). The third order derivative of the receiver's slant range at stationary point of receiver $\tilde{\tau}_R$ is given as:

$$\begin{aligned} \dddot{R}_R(\tilde{\tau}_R) &= -\frac{3v_R^4(\tilde{\tau}_R-\tau_{0R})}{R_R^3(\tilde{\tau}_R,R_{0R},\tau_{0R})}\left[1-\frac{v_R^2(\tilde{\tau}_R-\tau_{0R})^2}{R_R^2(\tilde{\tau}_R,R_{0R},\tau_{0R})}\right] \\ &= -\frac{3v_R^4(\tilde{\tau}_R-\tau_{0R})}{R_R^3(\tilde{\tau}_R,R_{0R},\tau_{0R})}\left[1-\frac{R_R^2(\tilde{\tau}_R,R_{0R},\tau_{0R})-R_{0R}^2}{R_R^2(\tilde{\tau}_R,R_{0R},\tau_{0R})}\right] \\ &= -\frac{3v_R^4(\tilde{\tau}_R-\tau_{0R})R_{0R}^2}{R_R^5(\tilde{\tau}_R,R_{0R},\tau_{0R})} \end{aligned} \tag{3.9}$$

The fourth order derivative of the receiver's slant range is given from equation (3.6) as:

$$\ddddot{R}_R(\tau) = -\frac{\left[3\ddot{R}_R^2(\tau) + 4\dot{R}_R(\tau)\dddot{R}_R(\tau)\right]}{R_R(\tau)} \tag{3.10}$$

Substituting equations (A.6), (3.7) and (3.9), into (3.10), we get the fourth order derivative of the receiver's slant range at receiver's stationary point $\tilde{\tau}_R$ as follows:

$$\begin{aligned}\ddddot{R}_R(\tilde{\tau}_R) &= -\frac{3}{R_R(\tilde{\tau}_R)}\left[\left(\frac{v_R^2 R_{0R}^2}{R_R^3(\tilde{\tau}_R)}\right)^2 - \frac{4v_R^6 R_{0R}^2(\tilde{\tau}_R - \tau_{0R})^2}{R_R^6(\tilde{\tau}_R)}\right] \\ &= -\frac{3v_R^4 R_{0R}^2}{R_R^7(\tilde{\tau}_R)}\left[R_{0R}^2 - 4v_R^2(\tilde{\tau}_R - \tau_{0R})^2\right]\end{aligned} \tag{3.11}$$

Due to symmetry, second, third and fourth order derivatives of the transmitter's slant range at transmitter's stationary point $\tilde{\tau}_T$ can be written as:

$$\begin{aligned}\ddot{R}_T(\tilde{\tau}_T) &= \frac{v_T^2 R_{0T}^2}{R_T^3(\tilde{\tau}_T)} \\ \dddot{R}_T(\tilde{\tau}_T) &= -\frac{3v_T^4(\tilde{\tau}_T - \tau_{0T})R_{0T}^2}{R_T^5(\tilde{\tau}_T)} \\ \ddddot{R}_T(\tilde{\tau}_T) &= -\frac{3v_T^4 R_{0T}^2}{R_T^7(\tilde{\tau}_T)}\left[R_{0T}^2 - 4v_T^2(\tilde{\tau}_T - \tau_{0T})^2\right]\end{aligned} \tag{3.12}$$

The derivatives of the transmitter and receiver slant ranges are used in the derivation of the transmitter's and receiver's validity constraints.

3.2.1 First Validity Constraint

After determining the slant range derivatives of the transmitter and receiver at their points of stationary phases, we can now derive validity constraints. The first validity constraint of transmitter and receiver are obtained using equation (3.5). Substituting the second and fourth order slant range derivatives of the transmitter from equation (3.12), we get:

$$\left|\frac{\frac{v_T^4 R_{0T}^2}{2R_T^7(\xi_T)}\left[R_{0T}^2 - 4v_T^2(\xi_T - \tau_{0T})^2\right](\tilde{\tau} - \tilde{\tau}_T)^2}{\frac{v_T^2 R_{0T}^2}{R_T^3(\tilde{\tau}_T)}}\right| << 1$$

$$\left|\frac{v_T^2\left[R_{0T}^2 - 4v_T^2(\xi_T - \tau_{0T})^2\right](\tilde{\tau} - \tilde{\tau}_T)^2}{2R_T^4(\xi_T)}\right| << 1 \tag{3.13}$$

The transmitter slant range evaluated at ξ_T can be expanded using equation (2.2), we get:

$$\left|\frac{v_T^2\left[R_{0T}^2-4v_T^2\left(\xi_T-\tau_{0T}\right)^2\right]\left(\tilde{\tau}-\tilde{\tau}_T\right)^2}{2R_T^4\left(\xi_T\right)}\right|<<1 \tag{3.14}$$

$$\left|\frac{v_T^2\left[1-\dfrac{4v_T^2\left(\xi_T-\tau_{0T}\right)^2}{R_{0T}^2}\right]\left(\tilde{\tau}-\tilde{\tau}_T\right)^2}{2R_T^2\left(\xi_T\right)\left[1-\dfrac{v_T^2\left(\xi_T-\tau_{0T}\right)^2}{R_{0T}^2}\right]}\right|<<1$$

Here, we make an assumption that the slant range is much larger than the distance covered by platform between two azimuth time instances ξ_T and τ_{0T}. This implies that $v_T^2\left(\xi_T-\tau_{0T}\right)^2<<R_{0T}^2$. This further implies that $\dfrac{v_T^2\left(\xi_T-\tau_{0T}\right)^2}{R_{0T}^2}<<1$. Using these assumptions we can simplify equation (3.14) as follows:

$$\left|\frac{v_T^2\left(\tilde{\tau}-\tilde{\tau}_T\right)^2}{2R_{0T}^2}\right|<<1 \tag{3.15}$$

$$\left|\tilde{\tau}-\tilde{\tau}_T\right|<<\frac{\sqrt{2}R_{0T}}{v_T}$$

Using equations (2.23), (2.24) and approximation given in equation (2.30), we can simplify the difference between the common and the transmitter's points of stationary phases.

$$\begin{aligned}\tilde{\tau}-\tilde{\tau}_T &= \frac{v_T^2\tau_{0T}+a_2\tau_{0R}v_R^2}{v_T^2+a_2v_R^2}-\frac{c_0R_{0T}f_\tau\left[\mu+\left(2-\mu\right)\right]}{2\left(f+f_0\right)\left[v_T^2+a_2v_R^2\right]}-\tau_{0T}+\frac{\mu R_{0T}f_\tau c_0}{2\left(f+f_0\right)v_T^2} \\ &= \frac{a_2v_R^2\left(\tau_{0R}-\tau_{0T}\right)}{v_T^2+a_2v_R^2}-\frac{f_\tau c_0}{2\left(f+f_0\right)}\left[\frac{R_{0T}\left[\mu+\left(2-\mu\right)\right]}{\left[v_T^2+a_2v_R^2\right]}-\frac{\mu R_{0T}}{v_T^2}\right] \\ &= -\frac{a_0}{1+\dfrac{v_T^2}{a_2v_R^2}}-\frac{f_\tau c_0R_{0T}}{2v_T^2\left(f+f_0\right)}\left[\frac{\dfrac{\left(2-\mu\right)v_T^2}{a_2v_R^2}-\mu}{1+\dfrac{v_T^2}{a_2v_R^2}}\right] \\ &= \frac{-a_0+\dfrac{f_\tau c_0}{2\left(f+f_0\right)}\left[\dfrac{\mu R_{0T}}{v_T^2}-\dfrac{\left(2-\mu\right)R_{0R}}{v_R^2}\right]}{1+\dfrac{v_T^2}{a_2v_R^2}}\end{aligned} \tag{3.16}$$

Substituting equation (3.16) into (3.15), we get:

$$\left|\frac{-a_0+\frac{f_\tau c_0}{2\left(f+f_0\right)}\left[\frac{\mu R_{0T}}{v_T^2}-\frac{\left(2-\mu\right)R_{0R}}{v_R^2}\right]}{1+\frac{v_T^2}{a_2 v_R^2}}\right| << \frac{\sqrt{2}R_{0T}}{v_T} \tag{3.17}$$

After simplification, first constraint of the transmitter is obtained as:

$$\left|L_{1T}\right| = \left|\frac{-a_0+\frac{f_\tau c_0}{2\left(f+f_0\right)}\left[\frac{\mu R_{0T}}{v_T^2}-\frac{\left(2-\mu\right)R_{0R}}{v_R^2}\right]}{\sqrt{2}v_T\left[\frac{R_{0T}}{v_T^2}+\frac{R_{0R}}{v_R^2}\right]}\right| << 1 \tag{3.18}$$

Similarly, we can derive first constraint of the receiver and is given as:

$$\left|L_{1R}\right| = \left|\frac{a_0+\frac{f_\tau c_0}{2\left(f+f_0\right)}\left[\frac{\left(2-\mu\right)R_{0R}}{v_R^2}-\frac{\mu R_{0T}}{v_T^2}\right]}{\sqrt{2}v_R\left[\frac{R_{0T}}{v_T^2}+\frac{R_{0R}}{v_R^2}\right]}\right| << 1 \tag{3.19}$$

Here, L_{1T} and L_{1R} denote first constraints of the transmitter and receiver respectively. They depend on range and azimuth frequencies, the platform velocities, slant ranges and azimuth times at the point of closest approach of the transmitter and receiver.

3.2.2 Second Validity Constraint

Second validity constraint of the transmitter and receiver are obtained using equation (3.4). Substituting the second and third order slant range derivatives of transmitter from equation (3.12), we get:

$$\left|\frac{\frac{3v_T^4\left(\tilde{\tau}_T-\tau_{0T}\right)R_{0T}^2}{2R_T^5\left(\tilde{\tau}_T\right)}\left(\tilde{\tau}-\tilde{\tau}_T\right)}{\frac{v_T^2R_{0T}^2}{R_T^3\left(\tilde{\tau}_T\right)}}\right| << 1 \tag{3.20}$$

$$\left|\tilde{\tau}_T-\tau_{0T}\right|\left|\tilde{\tau}-\tilde{\tau}_T\right| << \frac{2R_T^2\left(\tilde{\tau}_T\right)}{3v_T^2}$$

Substituting the transmitter's slant range from equation (2.2) evaluated at stationary point of transmitter, we get:

$$\left|\tilde{\tau}_T-\tau_{0T}\right|\left|\tilde{\tau}-\tilde{\tau}_T\right|<<\frac{2}{3v_T^2}\left[R_{0T}^2+v_T^2\left(\tilde{\tau}_T-\tau_{0T}\right)^2\right] \tag{3.21}$$

$$\left|\tilde{\tau}_T-\tau_{0T}\right|\left|\tilde{\tau}-\tilde{\tau}_T\right|<<\frac{2}{3}\left[\frac{R_{0T}^2}{v_T^2}+\left(\tilde{\tau}_T-\tau_{0T}\right)^2\right]$$

Now, we substitute azimuth time differences from equations (A.39) and (3.16) into above equation, we get:

$$\left|\frac{-a_0+\dfrac{f_\tau c_0}{2\left(f+f_0\right)}\left[\dfrac{\mu R_{0T}}{v_T^2}-\dfrac{\left(2-\mu\right)R_{0R}}{v_R^2}\right]}{1+\dfrac{v_T^2}{a_2v_R^2}}\right|<<\frac{2}{3}\frac{\left[\dfrac{R_{0T}^2}{v_T^2}+\left(\dfrac{\mu f_\tau c_0}{2v_T^2}\dfrac{R_{0T}}{\left(f+f_0\right)}\right)^2\right]}{\left|\dfrac{\mu f_\tau c_0}{2v_T^2}\dfrac{R_{0T}}{\left(f+f_0\right)}\right|} \tag{3.22}$$

$$\left|\left\{-a_0+\frac{f_\tau c_0}{2\left(f+f_0\right)}\left[\frac{\mu R_{0T}}{v_T^2}-\frac{\left(2-\mu\right)R_{0R}}{v_R^2}\right]\right\}\frac{\mu f_\tau c_0R_{0T}^2v_R^2}{2v_T^2R_{0R}\left(f+f_0\right)\left[a_2v_R^2+v_T^2\right]}\right|<<\frac{2R_{0T}^2}{3v_T^2}\left[1+\frac{\mu^2f_\tau^2c_0^2}{4v_T^2\left(f+f_0\right)^2}\right]$$

$$\left|\frac{\dfrac{3\mu f_\tau c_0}{4v_T^2\left(f+f_0\right)}\left\{-a_0+\dfrac{f_\tau c_0}{2\left(f+f_0\right)}\left[\dfrac{\mu R_{0T}}{v_T^2}-\dfrac{\left(2-\mu\right)R_{0R}}{v_R^2}\right]\right\}}{\dfrac{R_{0R}}{v_T^2v_R^2}\left[a_2v_R^2+v_T^2\right]\left[1+\dfrac{\mu^2f_\tau^2c_0^2}{4v_T^2\left(f+f_0\right)^2}\right]}\right|<<1$$

Simplifying above equation gives second constraint of the transmitter as follows:

$$\left|L_{2T}\right|=\left|\frac{\dfrac{3\mu f_\tau c_0}{4v_T^2\left(f+f_0\right)}\left\{-a_0+\dfrac{f_\tau c_0}{2\left(f+f_0\right)}\left[\dfrac{\mu R_{0T}}{v_T^2}-\dfrac{\left(2-\mu\right)R_{0R}}{v_R^2}\right]\right\}}{\left[\dfrac{R_{0T}}{v_T^2}+\dfrac{R_{0R}}{v_R^2}\right]\left[1+\dfrac{\mu^2f_\tau^2c_0^2}{4v_T^2\left(f+f_0\right)^2}\right]}\right|<<1 \tag{3.23}$$

Similarly, we can derive second constraint for the receiver and is given as:

$$\left|L_{2R}\right|=\left|\frac{\dfrac{3f_\tau c_0\left(2-\mu\right)}{4v_R^2\left(f+f_0\right)}\left\{a_0+\dfrac{f_\tau c_0}{2\left(f+f_0\right)}\left[\dfrac{\left(2-\mu\right)R_{0R}}{v_R^2}-\dfrac{\mu R_{0T}}{v_T^2}\right]\right\}}{\left[\dfrac{R_{0T}}{v_T^2}+\dfrac{R_{0R}}{v_R^2}\right]\left[1+\dfrac{\left(2-\mu\right)^2f_\tau^2c_0^2}{4v_R^2\left(f+f_0\right)^2}\right]}\right|<<1 \tag{3.24}$$

Here, L_{2T} and L_{2R} represent second constraints of the transmitter and receiver respectively.

3.3 Performance Analysis of Validity Constraints for Bistatic SAR Configurations

The validity constraints of the transmitter and receiver are used to verify the validity of BPTRS for different bistatic SAR configurations. We will consider here three different bistatic SAR configurations to validate our approach.

3.3.1 Tandem Configurations

It is an azimuth invariant bistatic SAR configuration, in which transmitter and receiver are flying on the same track following each other in such a way that they have fixed along track baseline between them. The tandem configuration is shown in Figure 18.

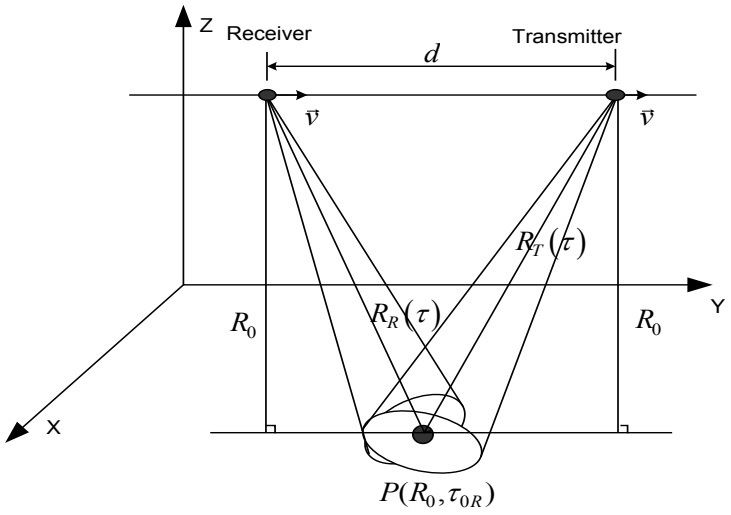

Figure 18: Tandem Configuration Geometry

We consider that the transmitter and receiver are moving with same velocity vectors and at point of closest approach their slant ranges are equal and are given as:

$$R_{0T} = R_{0R} = R_0 \tag{3.25}$$
$$v_T = v_R = v$$

The along track baseline between transmitter and receiver is given as:

$$d = \left|\tau_{0T} - \tau_{0R}\right| v \tag{3.26}$$

3.3.1.1 Validity constraints

The validity constraints of the transmitter given in equations (3.18) and (3.23) are simplified for tandem configuration and are expressed as:

$$\left|L_{1T\_Tandem}\right| = \left|\frac{a_0 v}{2\sqrt{2}R_0}\right| << 1$$

$$\left|L_{2T\_Tandem}\right| = \left|\frac{3a_0 f_\tau c_0}{8R_0\left(f+f_0\right)}\left[1+\frac{f_\tau^2 c_0^2}{4v^2\left(f+f_0\right)^2}\right]^{-1}\right| << 1 \tag{3.27}$$

Here, we have taken weighting factor $\mu = 1$, as the transmitter and receiver contribute equally towards the bistatic phase term. Validity constraints for receiver can be derived in a similar way. Simulations are carried out to evaluate the validity constraints for tandem configuration using the parameters given in Table 2.

Table 2: Parameters for Tandem Configuration

Parameters	**Transmitter**	**Receiver**
Velocity	100 m/s	
Pulse duration	3 μs	
Carrier frequency	10.17 GHz	
Bandwidth	300 MHz	
PRF	1250 Hz	
Squint Angle	-5.71°	5.71°
Off Nadir Angle	40°	40°
Slant Range	5000 m	
Distance between planes	1000 m	

The first transmitter constraint given in equation (3.27) does not depend on range and azimuth frequencies and has a numerical value equals 0.0707. Second transmitter constraint is plotted against range and azimuth frequencies and is shown in Figure 19. It has a maximum numerical value of 4.99×10^{-3}. The results show that both transmitter constraints are fulfilled for tandem configuration. Similarly, results for the receiver constraints can be obtained.

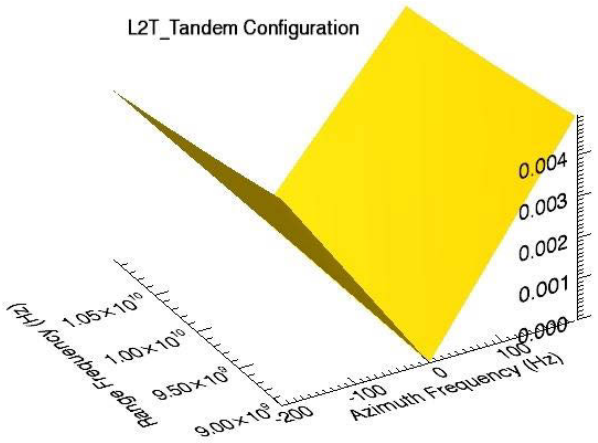

Figure 19: Validity Constraints for Tandem Configuration

3.3.1.2 Simulation Results

After analyzing the validity constraints of tandem configurations, we now consider focusing of a point target using Loffeld's BPTRS. The focusing result of a Point Target (PT) is shown in Figure 20. The parameters used in simulations are given in Table 2. Raw data is generated by collecting backscattered radiations in two-dimensional array, top left figure represents the raw data in range and azimuth; middle and right represent raw data after range and azimuth compression respectively and bottom one represents the focused PT. It shows clearly that the PT is well focused in range and azimuth.

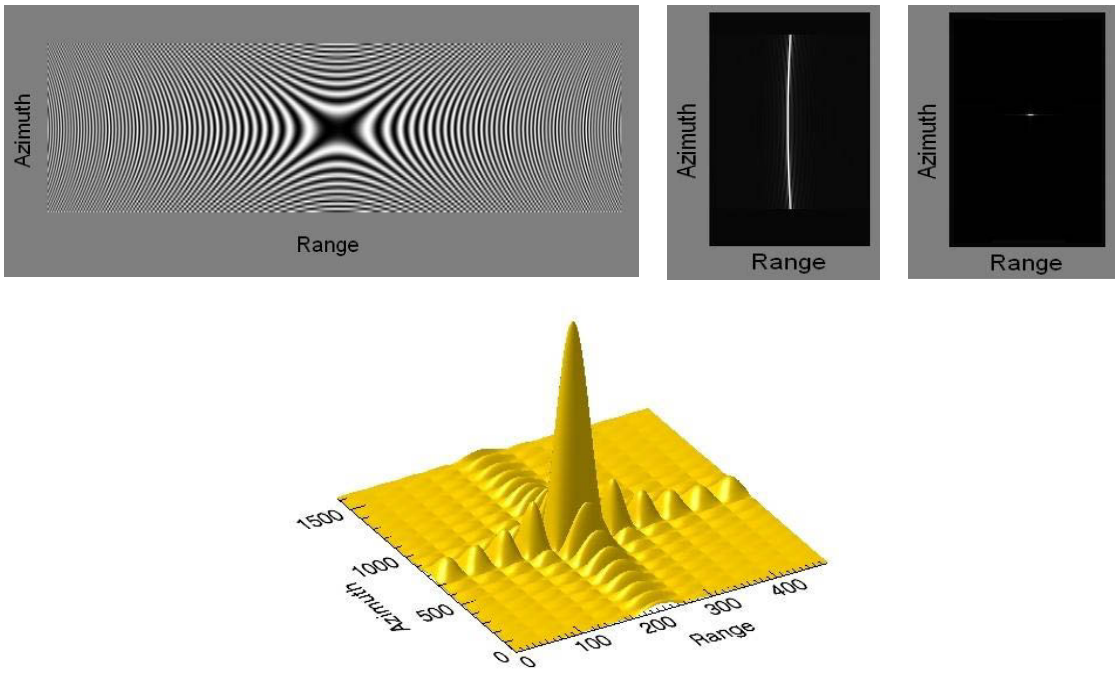

Figure 20: Focusing Results of Tandem Configuration

3.3.2 Translational Invariant Configurations

In TI configurations, transmitter and receiver move along parallel tracks with equal velocities, in such a way that the difference between the azimuth time of the transmitter and receiver at PCA is zero. The baseline between the transmitter and receiver is fixed.

$$\begin{aligned} v_T &= v_R = v \\ a_0 &= \left(\tau_{0T} - \tau_{0R}\right) = 0 \end{aligned} \tag{3.28}$$

The TI configuration is shown in Figure 21.

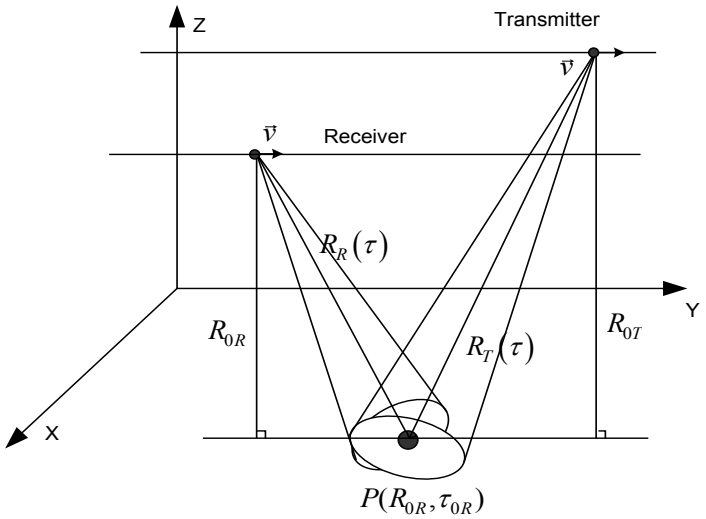

Figure 21: Translational Invariant Configuration Geometry

3.3.2.1 Validity Constraints

The validity constraints of the transmitter given in equations (3.18) and (3.23) are simplified for TI configuration and are given as:

$$\begin{aligned} \left|L_{1T\_TI}\right| &= \left|\frac{f_\tau c_0}{2\sqrt{2}\left(f+f_0\right)v}\left[\frac{R_{0T}-R_{0R}}{R_{0T}+R_{0R}}\right]\right| << 1 \\ \left|L_{2T\_TI}\right| &= \left|\frac{3}{2}\left[\frac{R_{0T}-R_{0R}}{R_{0T}+R_{0R}}\right]\left(1+\frac{4v^2\left(f+f_0\right)^2}{{f_\tau}^2 c_0^2}\right)^{-1}\right| << 1 \end{aligned} \tag{3.29}$$

The transmitter and receiver are contributing equally towards bistatic phase term, therefore, we have taken weighting factor $\mu = 1$. The validity constraints for TI configuration given in equation (3.29) are evaluated for an airborne configuration using parameters given in Table 3.

Table 3: Parameters for Translational Invariant Configuration

Parameters	**Transmitter**	**Receiver**
Velocity	100 m/s	
Pulse duration	3 µs	
Carrier frequency	10.17 GHz	
Bandwidth	300 MHz	
PRF	1250 Hz	
Squint Angle	0°	0°
Off Nadir Angle	30°	40°
Slant Range	4424 m	5000 m
Distance between planes	1000 m	

The constraints for receiver are completely analogous to the transmitter constraints and can be derived in a similar way. The transmitter constraints for TI configuration, are plotted against range and azimuth frequencies using the parameters given in Table 3 and are shown in Figure 22.

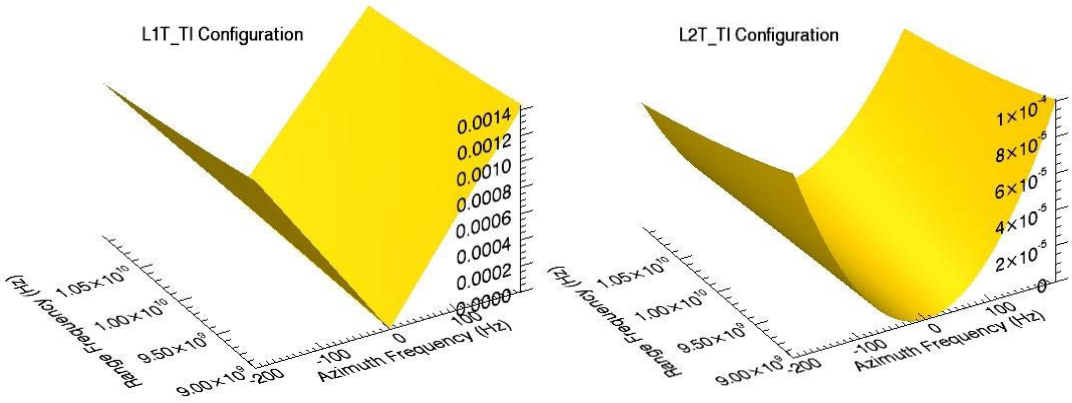

Figure 22: Validity Constraints for Translational Invariant Configuration

The first and second transmitter constraints have maximum numerical values of 1.43×10^{-3} and 1.016×10^{-4} respectively. The simulation results show that validity constraints are fulfilled for TI configuration. Similarly, results can be obtained for the receiver.

3.3.2.2 Simulation Results

Simulations are carried out for TI configurations. Bistatic point target references spectrum is used to focus a PT using parameters given in Table 3. Figure 23 shows that the PT is well focused both in range and azimuth.

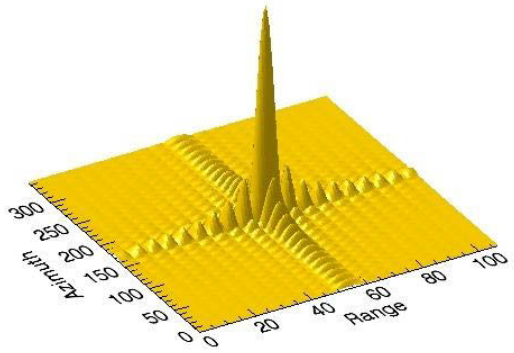

Figure 23: Focusing Result for Translational Invariant Configuration

3.3.3 Hybrid Configurations

A hybrid configuration is an azimuth variant spaceborne/airborne configuration. We assume that satellite is used as the transmitter and an aircraft as the receiver. Satellite is moving 76 times faster than the aircraft. In hybrid configurations, there is not only a large difference in the altitudes of transmitter and receiver but also in their velocities. Therefore, transmitter and receiver do not contribute equally towards the bistatic phase. Hence, different azimuth contributions of the transmitter and receiver phases have been taken into account, as mentioned in section 2.5. The weighting factor μ, which gives different weighting to the individual azimuth contributions of the transmitter and receiver phase terms, is defined in equation (2.32). A hybrid bistatic SAR configuration is shown in Figure 24.

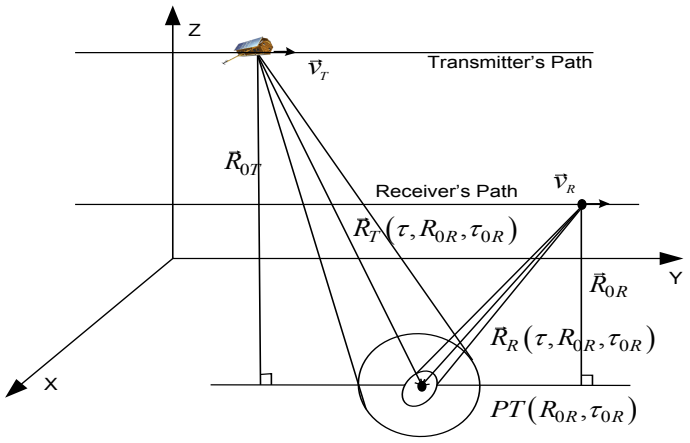

Figure 24: Hybrid Configuration Geometry

3.3.3.1 Validity Constraints

In order to verify our approach, simulations are carried out for hybrid configuration. Validity constraints of transmitter and receiver, given in equations (3.18), (3.19), (3.23) and (3.24) are analyzed for hybrid bistatic SAR configuration.

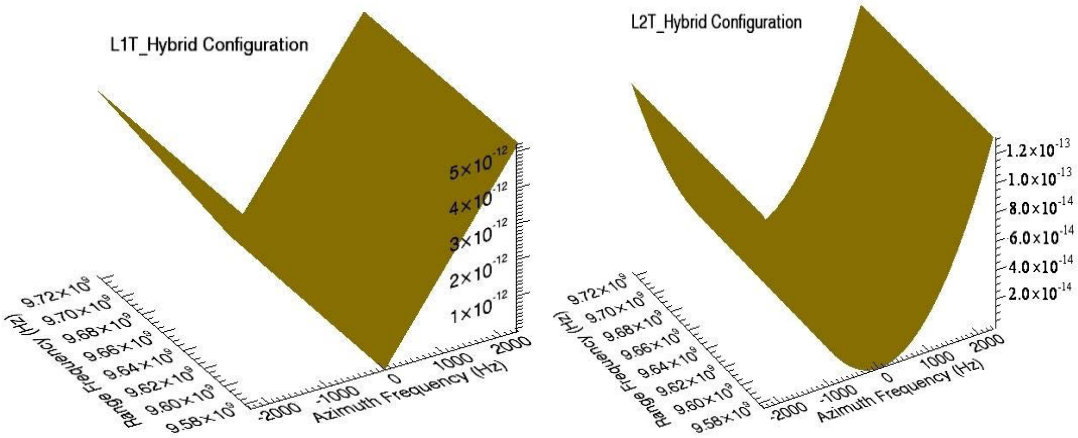

Figure 25: Transmitter Validity Constraints for Hybrid Configuration

The transmitter constraints are plotted in Figure 25 against range and azimuth frequencies using the parameters given in Table 1. The first and second transmitter constraints have maximum numerical values of 5.22×10^{-12} and 1.32×10^{-13} respectively.

Similarly, the receiver constraints are plotted in Figure 26. The first and second receiver constraints have maximum numerical values of 3.96×10^{-10} and 1.53×10^{-10} respectively.

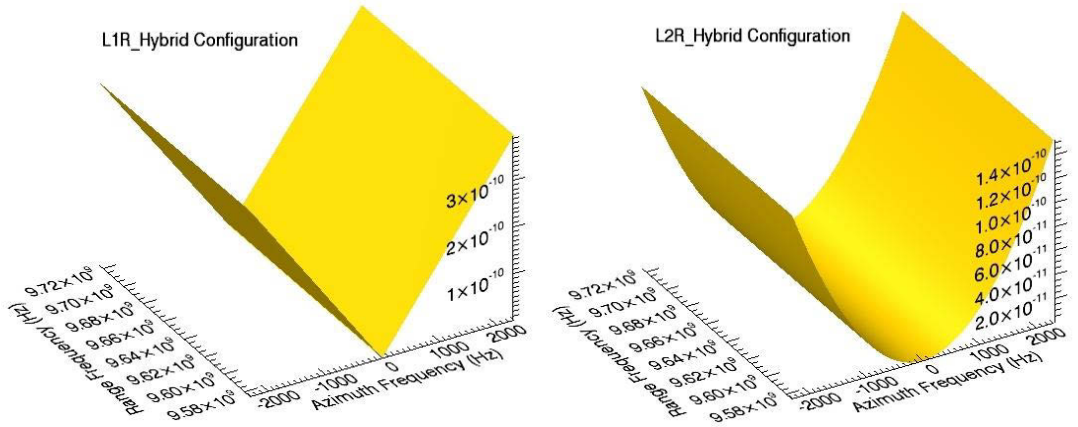

Figure 26: Receiver Validity Constraints for Hybrid Configuration

The simulation results show that both transmitter and receiver constraints are fulfilled for hybrid configuration.

3.3.3.2 Simulation Results

We consider focusing of a PT with and without using different azimuth contributions of the transmitter and receiver phases, using the parameters given in Table 1. Figure 27 shows focusing results using equal azimuth contributions of transmitter and receiver phase terms ($\mu = 1$).

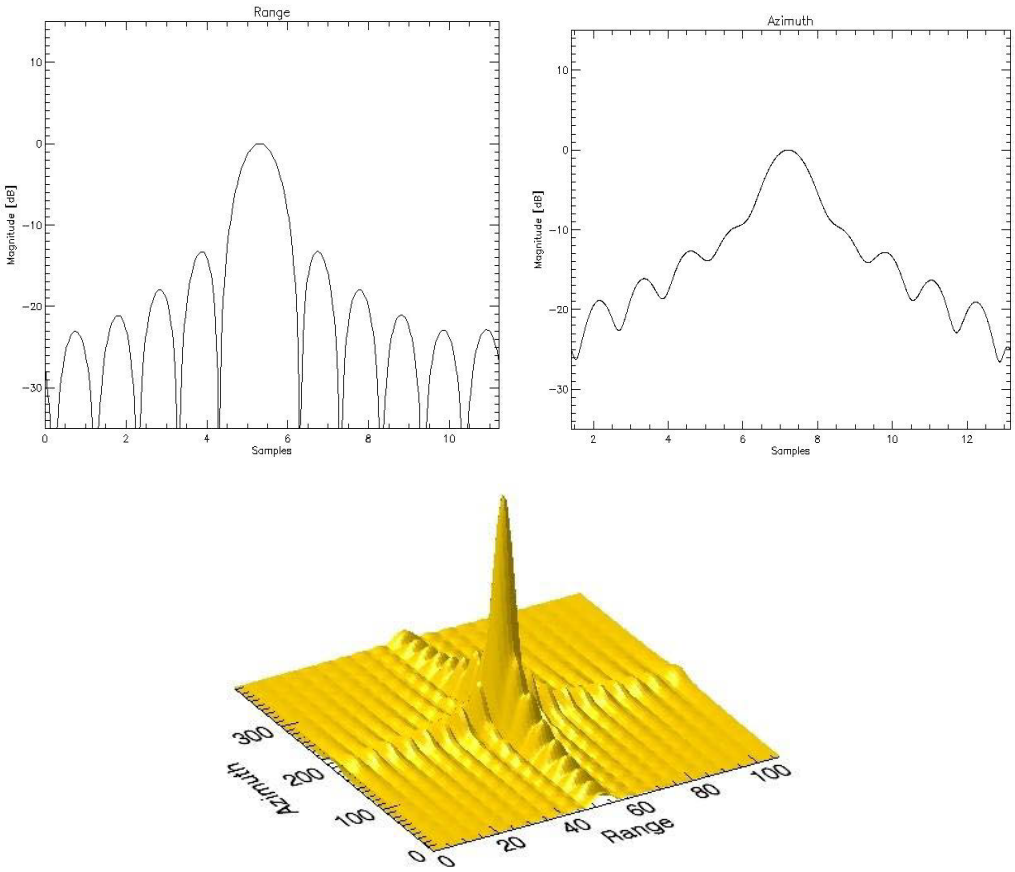

Figure 27: Focusing Results of Hybrid Configurations (Equal Azimuth Contribution of Transmitter and Receiver Phases)

In the above figure, we can compare the range and azimuth responses of a PT. It is obvious that the PT is focused in range but not in azimuth. Now we consider different azimuth contribution of the transmitter and receiver phases using μ given in equation (2.32). Figure 28 shows that point target is well focused in range and azimuth.

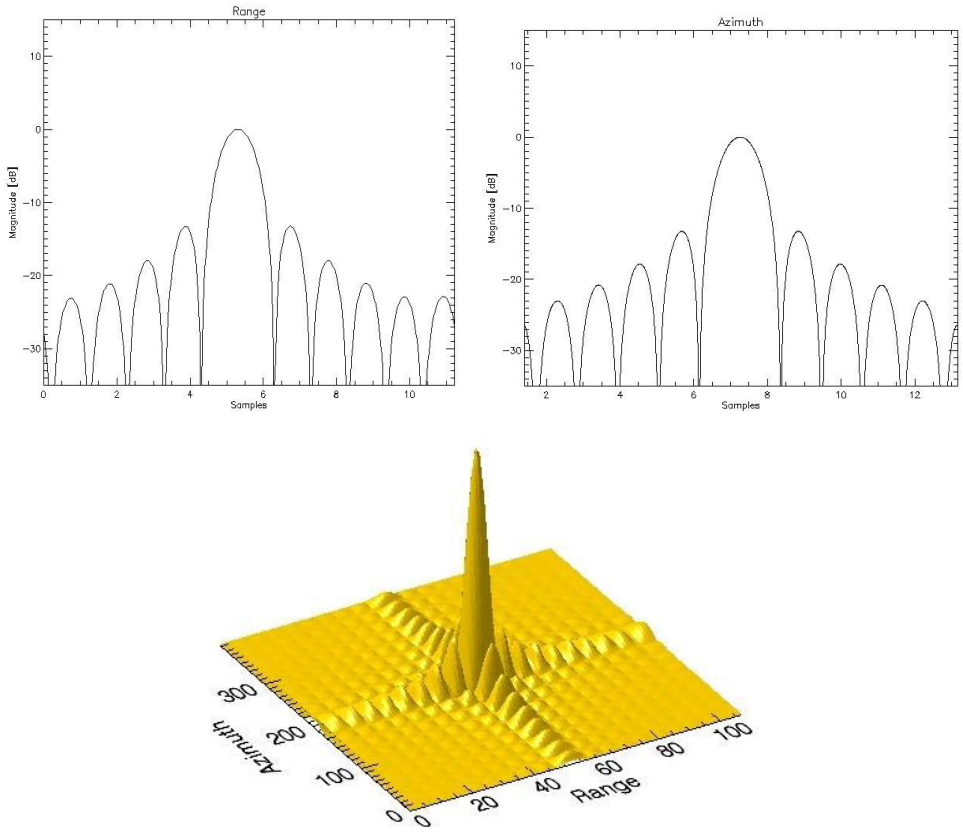

Figure 28: Focusing Results of Hybrid Configurations (Different Azimuth Contribution of Transmitter and Receiver Phases)

Comparing Figure 27 and Figure 28, we can say that in hybrid configurations due to extreme geometrical difference (altitudes and velocities) between the transmitter and receiver, equal azimuth contribution of the transmitter and receiver phases can not be taken into account.

3.4 Some Considerations on Validity Constraints

Four validity constraints are derived in section 3.2 for the transmitter and receiver. Both transmitter and receiver constraints depend on weighting factor μ. These constraints are further investigated in this section for hybrid bistatic SAR configuration in order to explore their dependence on the weighting factor μ.

3.4.1 First Validity Constraint for Transmitter

The first transmitter constraint is given in equation (3.18) and can be written as:

$$\left|L_{1T}\right| << 1 \qquad \Rightarrow \qquad -1 << L_{1T} << +1 \tag{3.30}$$

Now we consider two cases:

3.4.1.1 Case A:

In the first case, we assume that L_{1T} is positive, i.e. $L_{1T} \geq 0$.

$$L_{1T} << +1 \tag{3.31}$$

Substituting equation (3.18), into above relation we get:

$$\frac{-a_0 + \frac{f_\tau c_0}{2(f+f_0)}\left[\frac{\mu R_{0T}}{v_T^2} - \frac{(2-\mu)R_{0R}}{v_R^2}\right]}{\sqrt{2}v_T\left[\frac{R_{0T}}{v_T^2} + \frac{R_{0R}}{v_R^2}\right]} << 1 \tag{3.32}$$

The above equation is now simplified as follows:

$$-a_0 + \frac{f_\tau c_0}{2(f+f_0)}\left[\frac{\mu R_{0T}}{v_T^2} - \frac{(2-\mu)R_{0R}}{v_R^2}\right] << \sqrt{2}v_T\left[\frac{R_{0T}}{v_T^2} + \frac{R_{0R}}{v_R^2}\right] \tag{3.33}$$

After further simplifications, we can rewrite equation (3.33) in terms of the weighting factor μ as:

$$\mu_+ << \frac{2(f+f_0)}{f_\tau c_0}\left[\sqrt{2}v_T + a_0\left(\frac{R_{0T}}{v_T^2} + \frac{R_{0R}}{v_R^2}\right)^{-1}\right] + 2\left(1 + \frac{R_{0T}}{R_{0R}}\frac{v_R^2}{v_T^2}\right)^{-1} \tag{3.34}$$

The above equation gives the upper limit of the weighting factor μ and is denoted as μ_+.

3.4.1.2 Case B:

Here, we consider second case which will give us the lower limit of the weighting factor μ. We assume that L_{1T} is negative, i.e. $L_{1T} < 0$.

$$L_{1T} >> -1 \tag{3.35}$$

Substituting equation (3.18), into above relation we get:

$$\frac{-a_0 + \frac{f_\tau c_0}{2(f+f_0)}\left[\frac{\mu R_{0T}}{v_T^2} - \frac{(2-\mu)R_{0R}}{v_R^2}\right]}{\sqrt{2}v_T\left[\frac{R_{0T}}{v_T^2} + \frac{R_{0R}}{v_R^2}\right]} >> -1 \tag{3.36}$$

The above equation is now simplified as follows:

$$-a_0 + \frac{f_\tau c_0}{2(f+f_0)}\left[\frac{\mu R_{0T}}{v_T^2} - \frac{(2-\mu)R_{0R}}{v_R^2}\right] >> -\sqrt{2}v_T\left[\frac{R_{0T}}{v_T^2} + \frac{R_{0R}}{v_R^2}\right] \tag{3.37}$$

After further simplifications, we can rewrite equation (3.37) in terms of the weighting factor μ as:

$$\mu_{\_} >> \frac{2(f+f_0)}{f_\tau c_0}\left[a_0\left(\frac{R_{0T}}{v_T^2} + \frac{R_{0R}}{v_R^2}\right)^{-1} - \sqrt{2}v_T\right] + 2\left(1 + \frac{R_{0T}}{R_{0R}}\frac{v_R^2}{v_T^2}\right)^{-1} \tag{3.38}$$

The above equation gives the lower limit of the weighting factor μ for first transmitter constraint and is denoted as $\mu_{\_}$.

3.4.1.3 Simulation Results:

Simulations are carried out for spaceborne/airborne configuration using the parameters given in Table 1. Equation (3.34) and (3.38) provide us with upper and lower limits of the weighting factor μ for first transmitter constraint. They have azimuth frequency dependence. Using middle value of the interval given by equation (3.34) and (3.38), e.g. at azimuth frequency $f_\tau = 23\ Hz$, weighting factor is $\mu = 1.7$. The focusing result for a PT based on the weighted Loffeld's BPTRS is shown in Figure 29.

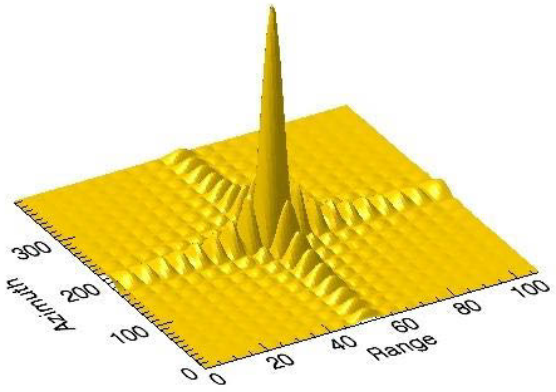

Figure 29: Focused Point Target using L_{1T}

Table 4: Quality Parameters for Focused Point Target using L_{1T}

	IRW (m)	**PSLR (dB)**	**ISLR (dB)**
Range	0.8906	-13.25	-10.56
Azimuth	0.978	-13.25	-10.65

The Impulse Response Width (IRW), Peak Side Lobe Ratio (PSLR) and Integrated Side Lobe Ratio (ISLR) are used as quality criteria for the focused result of a PT are given in Table 4. More details on quality measuring parameters are given in Appendix B.

3.4.2 First Validity Constraint for Receiver

The first receiver constraint is given in equation (3.19), we can write it as:

$$\left|L_{1R}\right| << 1 \qquad \Rightarrow \qquad -1 << L_{1R} << +1 \tag{3.39}$$

Again we consider two cases:

3.4.2.1 Case A:

In the first case, we assume that L_{1R} is positive, i.e. $L_{1R} \geq 0$.

$$L_{1R} << +1 \tag{3.40}$$

Substituting equation (3.19), into above equation we get:

$$\frac{a_0 + \dfrac{f_\tau c_0}{2\left(f+f_0\right)}\left(\dfrac{\left(2-\mu\right)R_{0R}}{v_R^2} - \dfrac{\mu R_{0T}}{v_T^2}\right)}{\sqrt{2}v_R\left(\dfrac{R_{0R}}{v_R^2} + \dfrac{R_{0T}}{v_T^2}\right)} << 1 \tag{3.41}$$

The above equation is now simplified as follows:

$$a_0 + \frac{f_\tau c_0}{2\left(f+f_0\right)}\left(\frac{\left(2-\mu\right)R_{0R}}{v_R^2} - \frac{\mu R_{0T}}{v_T^2}\right) << \sqrt{2}v_R\left(\frac{R_{0R}}{v_R^2} + \frac{R_{0T}}{v_T^2}\right) \tag{3.42}$$

After further simplifications, we can rewrite equation (3.42) in terms of the weighting factor μ as:

$$\mu_{-} >> 2\left(1 + \frac{R_{0T}}{R_{0R}}\frac{v_R^2}{v_T^2}\right)^{-1} + \frac{2\left(f+f_0\right)}{f_\tau c_0}\left[a_0\left(\frac{R_{0T}}{v_T^2} + \frac{R_{0R}}{v_R^2}\right)^{-1} - \sqrt{2}v_R\right] \tag{3.43}$$

The above equation gives the lower limit of the weighting factor μ and shows that it should be much greater than the expression on right hand side.

3.4.2.2 Case B:

Here, we consider second case which will give us the upper limit of the weighting factor μ. We assume that L_{1R} is negative, i.e. $L_{1R} < 0$.

$$L_{1R} >> -1 \tag{3.44}$$

Substituting equation (3.19), into above equation we get:

$$\frac{a_0 + \dfrac{f_\tau c_0}{2(f+f_0)}\left(\dfrac{(2-\mu)R_{0R}}{v_R^2} - \dfrac{\mu R_{0T}}{v_T^2}\right)}{\sqrt{2}v_R\left(\dfrac{R_{0T}}{v_T^2} + \dfrac{R_{0R}}{v_R^2}\right)} >> -1 \tag{3.45}$$

The above equation is now simplified as follows:

$$a_0 + \frac{f_\tau c_0}{2(f+f_0)}\left(\frac{(2-\mu)R_{0R}}{v_R^2} - \frac{\mu R_{0T}}{v_T^2}\right) >> -\sqrt{2}v_R\left(\frac{R_{0T}}{v_T^2} + \frac{R_{0R}}{v_R^2}\right) \tag{3.46}$$

After further simplifications, we can rewrite equation (3.46) in terms of the weighting factor μ as:

$$\mu_+ << \frac{2(f+f_0)}{f_\tau c_0}\left[a_0\left(\frac{R_{0T}}{v_T^2} + \frac{R_{0R}}{v_R^2}\right)^{-1} + \sqrt{2}v_R\right] + 2\left(1 + \frac{R_{0T}}{R_{0R}}\frac{v_R^2}{v_T^2}\right)^{-1} \tag{3.47}$$

The above equation gives the upper limit of the weighting factor μ for first receiver constraint and is denoted as μ_+.

3.4.2.3 Simulation Results:

Simulations are carried out for hybrid configuration using the parameters given in Table 1. Equation (3.47) and (3.43) provide upper and lower limits of the weighting factor μ for the first receiver constraint. Using middle value of the interval given by equation (3.47) and (3.43), e.g. at azimuth frequency $f_\tau = 23\ Hz$, weighting factor is $\mu = 4$. The focusing result for a PT based on the weighted Loffeld's BPTRS is shown in Figure 30.

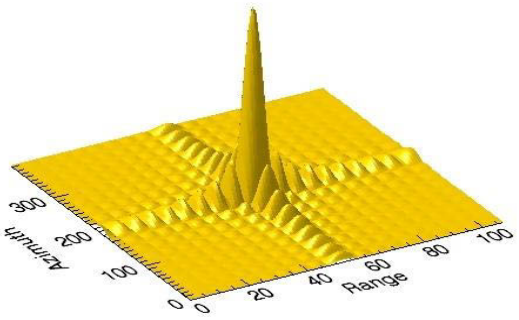

Figure 30: Focused Point Target using L_{1R}

The IRW, PSLR and ISLR for focused point target using the first validity constraint of receive are given in Table 5.

Table 5: Quality Parameters for Focused Point Target using L_{1R}

	IRW (m)	PSLR (dB)	ISLR (dB)
Range	0.89	-13.25	-10.56
Azimuth	0.978	-13.25	-10.65

3.4.3 Second Validity Constraint for Transmitter

The second transmitter's constraint is given in equation (3.23) and can be written as:

$$\left|L_{2T}\right| << 1 \tag{3.48}$$

Substituting equation (3.23), into above relation we get:

$$\left| \frac{3f_\tau c_0 \mu}{4v_T^2\left(f+f_0\right)} \left(\begin{array}{c} -a_0 + \dfrac{f_\tau c_0}{2\left(f+f_0\right)} \\ \left(\dfrac{\mu R_{0T}}{v_T^2} - \dfrac{\left(2-\mu\right)R_{0R}}{v_R^2} \right) \end{array} \right) \div D \right| << 1 \tag{3.49}$$

$$where, \quad D = \left(1 + \frac{f_\tau{}^2 c_0^2 \mu^2}{4v_T^2\left(f+f_0\right)^2} \right)\left(\frac{R_{0T}}{v_T^2} + \frac{R_{0R}}{v_R^2} \right)$$

From the above equation we can see that D is always positive and greater than 1. Hence, we can rewrite the above equation as:

$$\mu \left(\begin{array}{c} -a_0 + \dfrac{f_\tau c_0}{2\left(f+f_0\right)} \\ \left(\dfrac{\mu R_{0T}}{v_T^2} - \dfrac{\left(2-\mu\right)R_{0R}}{v_R^2} \right) \end{array} \right) << D \frac{4v_T^2\left(f+f_0\right)}{3f_\tau c_0} \tag{3.50}$$

As D is always positive and larger than one, we can simplify the above inequality as:

$$\mu \left[-a_0 + \frac{f_\tau c_0}{2\left(f+f_0\right)} \left(\frac{\mu R_{0T}}{v_T^2} - \frac{\left(2-\mu\right)R_{0R}}{v_R^2} \right) \right] << \frac{4v_T^2\left(f+f_0\right)}{3f_\tau c_0} \tag{3.51}$$

The above rational inequality can be solved by changing the inequality sign into an equality sign and is written as follows:

$$-a_0\mu + \frac{f_\tau c_0 \mu}{2\left(f+f_0\right)} \left[\mu \left(\frac{R_{0T}}{v_T^2} + \frac{R_{0R}}{v_R^2} \right) - \frac{2R_{0R}}{v_R^2} \right] - \frac{4v_T^2\left(f+f_0\right)}{3f_\tau c_0} = 0 \tag{3.52}$$

After further simplifications, we can write upper and lower limits of weighting factor μ as:

$$\mu_{\pm} = \frac{(f+f_0)}{f_\tau c_0}\left(\frac{R_{0T}}{v_T^2}+\frac{R_{0R}}{v_R^2}\right)^{-1}\left\{a_0+\frac{f_\tau c_0 R_{0R}}{v_R^2(f+f_0)} \pm \sqrt{\left(a_0+\frac{f_\tau c_0 R_{0R}}{v_R^2(f+f_0)}\right)^2+\frac{8v_T^2}{3}\left(\frac{R_{0T}}{v_T^2}+\frac{R_{0R}}{v_R^2}\right)}\right\} \quad (3.53)$$

3.4.3.1 Simulation Results:

Simulations are carried out for spaceborne/airborne configuration using the parameters given in Table 1. Equation (3.53) provides upper and lower limits of the weighting factor μ for the second transmitter constraint. They have azimuth frequency dependence. Using middle value of the interval given by equation (3.53), e.g. at azimuth frequency $f_\tau = 23\ Hz$, weighting factor is $\mu = 1.6$ and is in agreement with the results obtained from the first validity constraint of transmitter. The focusing result for a PT is shown in Figure 31.

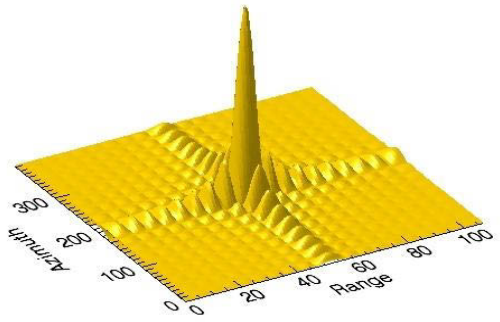

Figure 31: Focused Point Target using L_{2T}

The IRW, PSLR and ISLR for focused point target using second validity constraint of transmitter are given in Table 6.

Table 6: Quality Parameters for Focused Point Target using L_{2T}

	IRW (m)	**PSLR (dB)**	**ISLR (dB)**
Range	0.8906	-13.25	-10.56
Azimuth	0.978	-13.25	-10.65

A comparison of the quality parameters in Table 4 and Table 6 for first and second validity constraints of transmitter further confirms the agreement of the focusing results.

3.4.4 Second Validity Constraint for Receiver

The second receiver constraint is given in equation (3.24) and can be written as:

$$\left|L_{2R}\right| << 1 \tag{3.54}$$

$$\left|\frac{3f_\tau c_0(2-\mu)}{4v_R^2(f+f_0)}\left(a_0+\frac{f_\tau c_0}{2(f+f_0)}\left(\frac{(2-\mu)R_{0R}}{v_R^2}-\frac{\mu R_{0T}}{v_T^2}\right)\right)\div D\right| << 1$$

$$where,\quad D=\left(1+\frac{{f_\tau}^2 c_0^2(2-\mu)^2}{4v_R^2(f+f_0)^2}\right)\left(\frac{R_{0T}}{v_T^2}+\frac{R_{0R}}{v_R^2}\right)$$

Above equation shows dependence of L_{2R} on weighting factor μ. As D is always positive and greater than one, we can rewrite the above equation as:

$$(2-\mu)\left[a_0+\frac{f_\tau c_0}{2(f+f_0)}\left(\frac{(2-\mu)R_{0R}}{v_R^2}-\frac{\mu R_{0T}}{v_T^2}\right)\right] << D\frac{4v_R^2(f+f_0)}{3f_\tau c_0} \tag{3.55}$$

As stronger requirement would be written as:

$$(2-\mu)\left[a_0+\frac{f_\tau c_0}{2(f+f_0)}\left(\frac{(2-\mu)R_{0R}}{v_R^2}-\frac{\mu R_{0T}}{v_T^2}\right)\right] << \frac{4v_R^2(f+f_0)}{3f_\tau c_0} \tag{3.56}$$

The above rational inequality can be solved by changing the inequality sign into an equality sign and is written as follows:

$$(2-\mu)\left[a_0+\frac{f_\tau c_0}{2(f+f_0)}\left(\frac{2R_{0R}}{v_R^2}-\mu\left(\frac{R_{0T}}{v_T^2}+\frac{R_{0R}}{v_R^2}\right)\right)\right]-\frac{4v_R^2(f+f_0)}{3f_\tau c_0}=0 \tag{3.57}$$

After further simplifications, we can write upper and lower limits of the weighting factor μ as:

$$\mu_\pm=\frac{\left[\frac{(f+f_0)}{f_\tau c_0}\right]}{\left[\frac{R_{0T}}{v_T^2}+\frac{R_{0R}}{v_R^2}\right]}\left\{\begin{array}{l} a_0+\frac{f_\tau c_0}{(f+f_0)}\left(\frac{R_{0T}}{v_T^2}+\frac{2R_{0R}}{v_R^2}\right)\pm \\ \sqrt{\left(a_0+\frac{f_\tau c_0}{(f+f_0)}\left(\frac{R_{0T}}{v_T^2}+\frac{2R_{0R}}{v_R^2}\right)\right)^2-\frac{4f_\tau c_0}{(f+f_0)}} \\ \sqrt{\left(\frac{R_{0T}}{v_T^2}+\frac{R_{0R}}{v_R^2}\right)\left[a_0+\frac{f_\tau c_0 R_{0R}}{v_R^2(f+f_0)}-\frac{2v_R^2(f+f_0)}{3f_\tau c_0}\right]} \end{array}\right\} \tag{3.58}$$

3.4.4.1 Simulation Results:

Simulations are carried out for spaceborne/airborne configuration using the parameters given in Table 1. Equation (3.58) provides upper and lower limits of the weighting factor μ for the second receiver constraint. Using middle value of the interval given by

equation (3.58), e.g. at azimuth frequency $f_\tau = 23\ Hz$, weighting factor is $\mu = 2.1$ and is in agreement with the results obtained from the first validity constraint of receiver. The focusing result for a PT is shown in Figure 32.

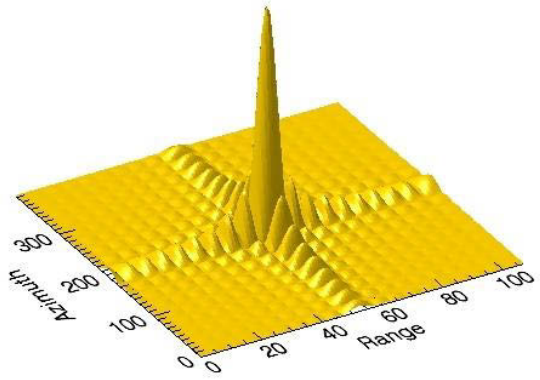

Figure 32: Focused Point Target using L_{2R}

The IRW, PSLR and ISLR for focused point target using the second validity constraint of transmitter are given in Table 7.

Table 7: Quality Parameters for Focused Point Target using L_{2R}

	IRW (m)	**PSLR (dB)**	**ISLR (dB)**
Range	0.89	-13.25	-10.56
Azimuth	0.978	-13.25	-10.65

Again, comparing the quality parameters in Table 5 and Table 7, for first and second validity constraints of the receiver, confirms agreement of the focusing results.

3.4.5 Comparison of Results

In this section, we have investigated the validity constraints based on LBF for a spaceborne/airborne configuration. These four validity constraints of transmitter and receiver provide us four ranges for weighting factor μ, such that the validity conditions are fulfilled. As these ranges overlap each other, we can choose weighting factor μ in such a way that all the constraints are fulfilled at the same time. For example, if we add the upper and lower limits of the weighting factor μ and divide it by 2.0 (i.e. center of the interval) or divide by 1.6 (i.e. close to the center of the interval), then all the four constraints are fulfilled at the same time. We have observed from our simulation results that, μ lies approximately in the center of the interval between its upper and lower limits.

Simulation results are supported with focusing of a PT for spaceborne/airborne configurations. The results obtained from the second validity constraints show good consistency with those obtained from the first validity constraints of transmitter and receiver respectively. Quality parameters are also provided for a good comparison of the focusing results.

3.5 Determining Unequal Azimuth Contribution of Transmitter and Receiver Phase Terms Based on Validity Constraints

Four validity constraints of transmitter and receiver are analyzed to determine the unequal azimuth contributions of the transmitter and receiver phase terms in the previous section. In this section, we further investigate the validity constraints of transmitter and receiver to find an analytical expression for the weighting factor μ. In section 3.4, some approximations have been used for the second constraint of transmitter and receiver. Here, we will focus only on the first validity constraints of transmitter and receiver to determine the weighting factor μ.

3.5.1 Transmitter constraint

Equations (3.34) and (3.38) give upper and lower limit of weighting factor μ, for the first transmitter's validity constraint. We can write:

$$\mu_{-} << \mu << \mu_{+} \tag{3.59}$$

However, it is not obvious from above expression that how much smaller or larger weighting factor μ should be from its upper and lower limit respectively. From the simulation results obtained in the previous section, we assume that weighting factor μ takes center value of this interval. We can write:

$$\mu = \frac{\mu_{+} + \mu_{-}}{2} \tag{3.60}$$

Substituting equations (3.34) and (3.38) into the above equation we get:

$$\begin{aligned} \mu &= \frac{2\left(f + f_0\right)}{f_\tau c_0} a_0 \left(\frac{R_{0T}}{v_T^2} + \frac{R_{0R}}{v_R^2} \right)^{-1} + 2\left(1 + \frac{R_{0T}}{R_{0R}} \frac{v_R^2}{v_T^2} \right)^{-1} \\ &= \frac{2v_T^2}{\left[v_R^2 R_{0T} + R_{0R} v_T^2 \right]} \left[\frac{a_0 v_R^2 \left(f + f_0 \right)}{f_\tau c_0} + R_{0R} \right] \end{aligned} \tag{3.61}$$

Simplifying the above expression we get:

$$\mu = \frac{2v_T^2}{a_2 v_R^2 + v_T^2}\left[1 + \frac{a_0 v_R^2 (f + f_0)}{f_\tau c_0 R_{0R}}\right] \tag{3.62}$$

The above equation gives the same result as we have obtained by minimizing the square difference between the common point of stationary phase $\tilde{\tau}$ and the individual points of stationary phases of the transmitter or receiver $\tilde{\tau}_T, \tilde{\tau}_R$ and are given in the equations (2.36) and (2.40).

3.5.2 Receiver Constraint

Equations (3.47) and (3.43) give upper and lower limit of the weighting factor μ, for the first receiver constraint. Considering average value of this interval we can write:

$$\mu = \frac{2a_0 (f + f_0)}{f_\tau c_0}\left(\frac{R_{0T}}{v_T^2} + \frac{R_{0R}}{v_R^2}\right)^{-1} + 2\left(1 + \frac{R_{0T}}{R_{0R}}\frac{v_R^2}{v_T^2}\right)^{-1} \tag{3.63}$$

Simplifying the above expression we get:

$$\mu = \frac{2v_T^2}{a_2 v_R^2 + v_T^2}\left[1 + \frac{a_0 v_R^2 (f + f_0)}{f_\tau c_0 R_{0R}}\right] \tag{3.64}$$

The above equation gives the same result as obtained for the first transmitter's constraint and is also in agreement with the results obtained in the equations (2.36) and (2.40).

3.5.3 Simulation Results

In order to verify our bistatic SAR processing approach, we consider a simulated scene consisting of nine point targets arranged as elements of a $[3\times3]$ matrix. The raw data is generated for hybrid configuration. The set of PTs are focused using weighted Loffeld's point target reference spectrum.

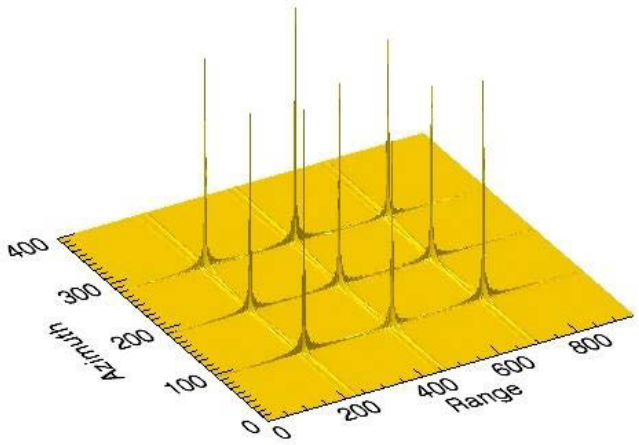

Figure 33: Focused Point Targets

The processing result of the simulated data using the parameters given in Table 1 is shown in Figure 33. All the point targets are well focused in range and azimuth.

3.6 Conclusions

In this chapter, we have derived four validity constraints for the transmitter and the receiver. These validity constraints are then applied to different bistatic SAR configurations. They are verified for tandem and TI configurations. Later, we considered hybrid configurations; simulations showed that validity constraints are better verified using different azimuth contributions of the transmitter and receiver phases.

These four validity constraints are used to find out upper and lower limit for the weighting factor and simulation results are provided in each case. From the simulation results, it is observed that the weighting factor takes the average value of its upper and lower limits. The analytical expressions of the average of the upper and lower limits of weighting factor for first validity constraints of transmitter and receiver gave similar results as obtained in the previous chapter. Hence, it further verifies our results.

4 General Focusing Algorithm for Different Bistatic SAR Configurations

4.1 Introduction

Bistatic SAR is considered as a very effective tool for exploring different geometrical configurations. The spatial separation of the transmitter and receiver not only allows different data acquisition geometries but also provides more information content of the imaging scene. The location of transmitter and receiver on different platforms has several advantages over monostatic SAR systems. Analysis and classification of objects in bistatic SAR has improved based on their backscattering characteristics. Different experiments have been performed and processing algorithms have been implemented over the years [1]-[81]. The first series of hybrid bistatic experiments with spaceborne transmitter and airborne receiver were conducted by USA in the mid nineties using ERS-1 satellite and SIR-C space shuttle as transmitter with airborne receivers [32]. Due to limitation in technology and bistatic processing algorithms, less interest was seen in the bistatic area. With the proposal of interferometric cartwheel [65] in 2001, several bistatic SAR experiments [25], [29]-[33] were conducted with great interest. FHR has performed airborne bistatic experiments in 2003, using their AER-II as airborne transmitter and PAMIR as airborne receiver [25]. In 2007, DLR conducted hybrid bistatic experiment using their TerraSAR-X satellite as transmitter with F-SAR airborne receiver [31]. During 2008 and 2009, FHR performed hybrid bistatic SAR experiments, using TerraSAR-X satellite as transmitter and PAMIR as airborne receiver [29]-[30].

The focusing of bistatic SAR data has been addressed in a number of publications [1]-[61]. The wave number domain algorithm to focus bistatic SAR data is presented in [17], [26] and [35]. A preprocessing technique used to transform azimuth invariant configurations to monostatic geometry, also called 'Dip move out' is given in [14], [15]. A numerical transfer function for bistatic SAR data processing is presented in [34]. A modified range Doppler algorithm is proposed for processing bistatic configurations in [35]. A nonlinear chirp scaling algorithm based on analytical BPTRS is applied to bistatic configurations in [41], [45]. Based on LBF [1], scaled inverse Fourier transformation is used for azimuth variant and invariant configurations and is given in [8], [47] and [52]. In [8], different azimuth contributions of the transmitter and receiver phase terms have not been taken into account, therefore it does not work well for hybrid configurations. In [47], the linearization of BPTRS accommodates both BD and QM phase terms. It involves many phase terms and computationally complex range and azimuth

variant modulation and scaling terms, inspite of the fact that the contribution of linearized BD phase term is negligible towards them.

In this chapter, we consider different bistatic SAR configurations and present a general frequency domain focusing algorithm. The approach used for focusing the complete scene is based on LBF. A BPTRS has been derived in chapter 2, using different azimuth contributions of the transmitter and receiver phases. In this chapter, we implement an efficient processing algorithm using a SIFT for focusing of the complete scene.

4.2 Frequency Domain Focusing of a Complete Scene

The BPTRS in range and azimuth frequency domain is expressed in equation (2.19). It contains all important parameters used for processing. The spectrum of a complete scene is the sum of the reflected signals from all PTs and is expressed as follows:

$$W_0\left(f,f_\tau\right)=\int_{-\infty}^{\infty}\int_{-\infty}^{\infty}G_l\left(f,f_\tau,R_{0R},\tau_{0R}\right)dR_{0R}d\tau_{0R} \tag{4.1}$$

The above equation represents integration of BPTRS over all PTs illuminated by antenna. The final expression of the references spectrum $G_l\left(f,f_\tau,R_{0R},\tau_{0R}\right)$ of PT located at $\left(R_{0R},\tau_{0R}\right)$ is given in equation (2.19). Different steps are involved in the bistatic SAR processing. In the first step range compression is done using match filtering operation in the frequency domain. The complete scene spectrum is multiplied by complex conjugate of the transmitted signal and is expressed as follows:

$$W_1\left(f,f_\tau\right)=W_0\left(f,f_\tau\right)\times S_l^*\left(f\right) \tag{4.2}$$

Here, $S_l\left(f\right)$ is the transmitted signal spectrum. After range compression, the compressed spectrum needs to undergo an amplitude term $A_{amp}\left(f,f_\tau\right)$ correction. The amplitude term is corrected by multiplying the spectrum with its inverse. We get the following expression:

$$\begin{aligned} W_2\left(f,f_\tau\right)&=W_1\left(f,f_\tau\right)\times A_{amp}\left(f,f_\tau\right) \\ A_{amp}\left(f,f_\tau\right)&=\sqrt{\frac{1}{c_0R_{0R}}\left[\frac{v_T^2F_T^{3/2}\left(f,f_\tau\right)}{a_2}+v_R^2F_R^{3/2}\left(f,f_\tau\right)\right]}\Bigg/\left|f+f_0\right| \end{aligned} \tag{4.3}$$

We assume parallel flight trajectories of transmitter and receiver. The parameter a_2, given in equation (2.25) is constant over the azimuth time. We consider the average value of the receiver's slant range R_{0R} at PCA for the amplitude term correction.

After that, we will perform the BD phase term Ψ_{BD} compensation. In [47], the linearization of both QM and BD phase terms is considered. It involves a very complex derivation comprising a number of phase terms and computationally complex range and azimuth scaling and shift terms for the complete scene focusing. After processing the raw data using this algorithm [47], we observe that the contribution of BD phase term is negligible and the main contribution towards the bistatic phase comes from the QM phase term. Therefore, we compensate it before applying the Taylor's expension to the remaining phase term of the complete scene Ψ_{CS}. The BD phase term compensation is given as follows:

$$W_3\left(f, f_\tau\right) = W_2\left(f, f_\tau\right) \times \Psi_{BD}^{*} \tag{4.4}$$

The complete scene spectrum after range compression, amplitude correction and BD phase term compensation can be written as:

$$W_3(f, f_\tau) = \int_{-\infty}^{\infty}\int_{-\infty}^{\infty} \sigma\left(R_{0R}, \tau_{0R}\right)\; e^{-j\Psi_{CS}\left(f, f_\tau, R_{0R}, \tau_{0R}\right)}\; dR_{0R} d\tau_{0R} \tag{4.5}$$

Here, Ψ_{CS} is the remaining phase term of the complete scene and is expressed as:

$$\begin{aligned}\Psi_{CS}\left(f, f_\tau, R_{0R}, \tau_{0R}\right) = \pi f_\tau \left[\left(2-\mu\right)\tau_{0R} + \mu\tau_{0T}\right] + \\ \frac{2\pi}{c_0}\left[R_{0R} F_R^{1/2}\left(f, f_\tau\right) + R_{0T} F_T^{1/2}\left(f, f_\tau\right)\right]\end{aligned} \tag{4.6}$$

The complete scene phase term Ψ_{CS} is not linearly dependent on the four space position variables $\left(R_{0R}, \tau_{0R}, R_{0T}, \tau_{0T}\right)$. Here, R_{0T}, τ_{0T} are functions of the target coordinates R_{0R}, τ_{0R}. Before linearizing the complete scene phase term Ψ_{CS}, we need to express R_{0T}, τ_{0T} in terms of receiver's coordinates R_{0R}, τ_{0R}.

$$Y = HX \tag{4.7}$$

$$Y = \begin{bmatrix}\tau_{0T} & R_{0T}\end{bmatrix}^T; \qquad X = \begin{bmatrix}1 & \tau_{0R} & R_{0R}\end{bmatrix}^T; \qquad H = \begin{bmatrix}e_{11} & e_{12} & e_{13} \\ e_{21} & e_{22} & e_{23}\end{bmatrix}$$

After simplifying the above equations, we can express R_{0T}, τ_{0T} as:

$$\begin{aligned}\tau_{0T} &= e_{11} + e_{12} R_{0R} + e_{13}\tau_{0R} \\ R_{0T} &= e_{21} + e_{22} R_{0R} + e_{23}\tau_{0R}\end{aligned} \tag{4.8}$$

Here, $\left(e_{11}, e_{12}, e_{13}, e_{21}, e_{22}, e_{23}\right)$ are linearization parameters and can be computed as follows:

$$e_{11} = \tau_{0T}(0, R_m); \qquad e_{12} = \left.\frac{\partial \tau_{0T}}{\partial R_{0R}}\right|_{\substack{\tau_{0R}=0 \\ R_{0R}=R_m}}; \qquad e_{13} = \left.\frac{\partial \tau_{0T}}{\partial \tau_{0R}}\right|_{\substack{\tau_{0R}=0 \\ R_{0R}=R_m}} \tag{4.9}$$

$$e_{21} = R_{0T}(0, R_m); \qquad e_{22} = \left.\frac{\partial R_{0T}}{\partial R_{0R}}\right|_{\substack{\tau_{0R}=0 \\ R_{0R}=R_m}}; \qquad e_{23} = \left.\frac{\partial R_{0T}}{\partial \tau_{0R}}\right|_{\substack{\tau_{0R}=0 \\ R_{0R}=R_m}}$$

Equation (4.8) is used to represent R_{0T}, τ_{0T} in terms of R_{0R}, τ_{0R} and using this information the complete scene phase term Ψ_{CS} in equation (4.6) can be simplified. The linearization operation is performed at $\tau_{0R} = 0;\ R_{0R} = R_m$.Where R_m is the closest range from scene center to the receiver's track. A range variable $r = R_{0R} - R_m$ is introduced which is the difference between the receiver range at PCA R_{0R} and R_m. The linear expression of the complete scene phase term Ψ_{CS} is represented as:

$$\begin{aligned} \Psi_{LCS}(f, f_\tau, R_{0R}, \tau_{0R}) \approx{}& \Psi_{CS}(f, f_\tau, R_{0R}, \tau_{0R})\Big|_{\substack{\tau_{0R}=0 \\ R_{0R}=R_m}} \\ &+ \left.\frac{\partial \Psi_{CS}(f, f_\tau, R_{0R}, \tau_{0R})}{\partial \tau_{0R}}\right|_{\substack{\tau_{0R}=0 \\ R_{0R}=R_m}} \tau_{0R} \\ &+ \left.\frac{\partial \Psi_{CS}(f, f_\tau, R_{0R}, \tau_{0R})}{\partial R_{0R}}\right|_{\substack{\tau_{0R}=0 \\ R_{0R}=R_m}} (R_{0R} - R_m) \end{aligned} \tag{4.10}$$

The first term in the above expression is space invariant and can be taken out from the integral. The second and third terms are azimuth and range variant terms respectively.

$$\begin{aligned} \Psi_{CS0}(f, f_\tau) &= \Psi_{CS}(f, f_\tau, R_{0R}, \tau_{0R})\Big|_{\substack{\tau_{0R}=0 \\ R_{0R}=R_m}} \\ &= \pi f_\tau \mu R_m e_{11} + \frac{2\pi}{c_0} R_m \left[F_R^{1/2}(f, f_\tau) + F_T^{1/2}(f, f_\tau) e_{21} \right] \end{aligned} \tag{4.11}$$

Second term:

$$\begin{aligned} \Psi_{CS\_Az}(f, f_\tau) &= \left.\frac{\partial \Psi_{CS}(f, f_\tau, R_{0R}, \tau_{0R})}{\partial \tau_{0R}}\right|_{\substack{\tau_{0R}=0 \\ R_{0R}=R_m}} \\ &= R_m \pi f_\tau \left[(2 - \mu) + \mu e_{13} \right] + \frac{2\pi}{c_0} R_m F_T^{1/2}(f, f_\tau) e_{23} \end{aligned} \tag{4.12}$$

Third term:

$$\Psi_{CS\_Ra}(f,f_\tau)=\left.\frac{\partial\Psi_{CS}(f,f_\tau,R_{0R},\tau_{0R})}{\partial R_{0R}}\right|_{\substack{\tau_{0R}=0\\R_{0R}=R_m}} \tag{4.13}$$

$$=\pi f_\tau \mu R_m e_{12}+\frac{2\pi}{c_0}R_m\left[F_R^{1/2}(f,f_\tau)+F_T^{1/2}(f,f_\tau)e_{22}\right]$$

Substituting Equations (4.10) - (4.13) into (4.5), we get:

$$W_3(f,f_\tau)=e^{-j\Psi_{CS0}(f,f_\tau)} \tag{4.14}$$

$$\int_{-\infty}^{\infty}\int_{-\infty}^{\infty}\sigma(R_{0R},\tau_{0R})e^{-j\left[\Psi_{CS\_Ra}(f,f_\tau)(R_{0R}-R_m)+\Psi_{CS\_Az}(f,f_\tau)\tau_{0R}\right]}dR_{0R}d\tau_{0R}$$

Range dependent phase term is expanded using the first order Taylor expansion at range frequency f, we get the following expression:

$$\Psi_{CS\_Ra}(f,f_\tau)\approx\Psi_{CS\_Ra}(f,f_\tau)\Big|_{f=0}+\left.\frac{\partial\Psi_{CS\_Ra}(f,f_\tau)}{\partial f}\right|_{f=0}f \tag{4.15}$$

$$\approx A_{Ra}(f_\tau)+B_{Ra}(f_\tau)f$$

The first term is the range shift term and is dependent on the azimuth frequency. The second term is the range scaling term and is also azimuth frequency dependent term. They are expressed as:

$$A_{Ra}(f_\tau)=\pi f_\tau\mu R_m e_{12}+2\pi R_m\frac{f_0}{c_0}\left\{\sqrt{1-\frac{(2-\mu)^2 f_\tau^2 c_0^2}{4v_R^2 f_0^2}}+e_{22}\sqrt{1-\frac{\mu^2 f_\tau^2 c_0^2}{4v_T^2 f_0^2}}\right\} \tag{4.16}$$

$$B_{Ra}(f_\tau)=\frac{2\pi R_m}{c_0}\left\{\frac{1}{\sqrt{1-\frac{(2-\mu)^2 f_\tau^2 c_0^2}{4v_R^2 f_0^2}}}+\frac{e_{22}}{\sqrt{1-\frac{\mu^2 f_\tau^2 c_0^2}{4v_T^2 f_0^2}}}\right\}$$

The azimuth dependent phase term of equation (4.14) is expanded using the first order Taylor expansion at azimuth frequency f_τ.

$$\Psi_{CS\_Az}(f,f_\tau)\approx\Psi_{CS\_Az}(f,f_\tau)\Big|_{f_\tau=0}+\left.\frac{\partial\Psi_{CS\_Az}(f,f_\tau)}{\partial f_\tau}\right|_{f_\tau=0}f_\tau \tag{4.17}$$

$$\approx A_{Az}(f)+B_{Az}f_\tau$$

The first term is the azimuth shift and is range frequency dependent and the second term is the azimuth scaling and is constant.

$$A_{Az}(f) = 2\pi R_m e_{23} \frac{(f + f_0)}{c_0} \qquad (4.18)$$
$$B_{Az} = \pi R_m \left[(2 - \mu) + \mu e_{13} \right]$$

Equation (4.14) is simplified using equation (4.15) and (4.17), and is written as:

$$W_3(f, f_\tau) = H(f, f_\tau) \qquad (4.19)$$
$$\int_{-\infty}^{\infty} \int_{-\infty}^{\infty} \sigma(R_{0R}, \tau_{0R}) e^{-j\left[\left(A_{Ra}(f_\tau) + B_{Ra}(f_\tau) f \right) R_{0R} + \left(A_{Az}(f) + B_{Az} f_\tau \right) \tau_{0R} \right]} dR_{0R} d\tau_{0R}$$

Where $H(f, f_\tau)$ is expressed as:

$$H(f, f_\tau) = e^{-j\Psi_{CS0}(f, f_\tau)} e^{j\left[A_{Ra}(f_\tau) + B_{Ra}(f_\tau) f \right] R_m} \qquad (4.20)$$

Equation (4.19) can be further simplified as:

$$W_4(f, f_\tau) = W_3(f, f_\tau) \times H^*(f, f_\tau) \qquad (4.21)$$
$$\approx \sigma\left(A_{Ra}(f_\tau) + B_{Ra}(f_\tau) f, A_{Az}(f) + B_{Az} f_\tau \right)$$

Here, the final spectrum is represented in terms of the back scattering coefficient, which is scaled and shifted in range and azimuth. Now the next step is to compensate the shift and scaling in range and azimuth. A SIFT will be used to convert the scaled spectrum into non scaled counter parts [3]-[8]. More details are given in Appendix C.

4.3 Focusing Algorithm for Bistatic SAR Configurations

Bistatic SAR focusing can be interpreted as a process of obtaining the backscattering coefficient in image space $\sigma(r, \tau_{0R})$ domain. Here, we use a SIFT to correct scaling in range and azimuth directions. The implementation of the processing algorithm for general bistatic SAR configurations is shown in Figure 34 .

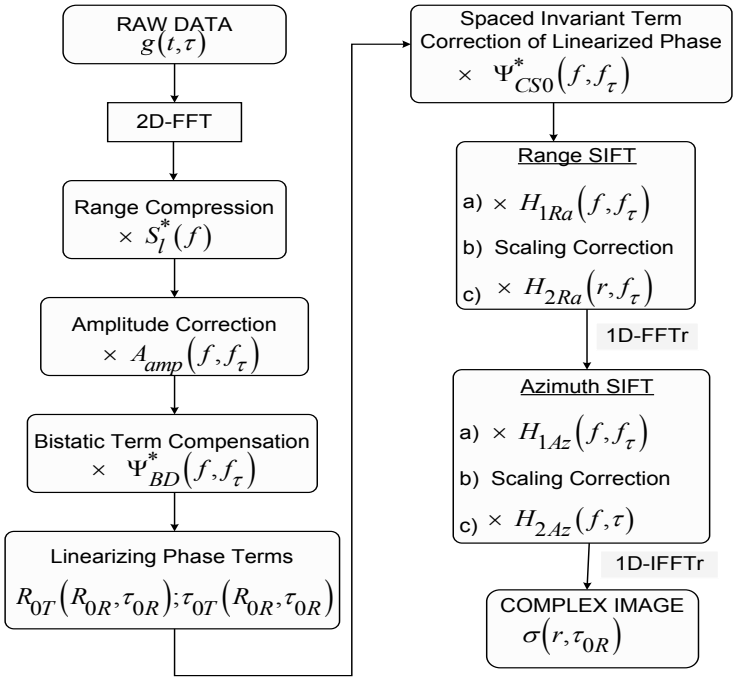

Figure 34: Block Diagram of Bistatic SAR Processing Algorithm

The processing steps are explained as follows:

1. The first step is transforming raw data from range and azimuth time domain to frequency domain. This is done by taking two dimensional Fourier transformations of the raw data. After that, range compression is performed by using match filtering in the frequency domain. Raw data is multiplied with the complex conjugate of the transmitted signal spectrum. The range compression is represented in equation (4.2).
2. The next step performs the amplitude correction. The constant amplitude terms of compressed spectrum are cancelled by multiplying with their inverse, as given in equation (4.3). It is followed by BD phase term compensation, which is done by multiplying the compressed spectrum with the complex conjugate of the BD phase term and is described in equation (4.4). The BD phase term as given in equation (2.26) depends on the transmitter's v_T and receiver's v_R velocities, range f and azimuth f_τ frequencies, a_2 and average value of receiver's slant range R_{0R} at PCA. The resulting spectrum after range compression, amplitude correction and bistatic deformation phase term compensation is given in equations (4.5) and (4.6).
3. Then, the phase term is linearized. Bistatic phase term depends on slant ranges and azimuth time of transmitter and receiver $(R_{0T}, R_{0R}, \tau_{0T}, \tau_{0R})$ at PCA. Linearization is achieved by representing slant range and azimuth time at PCA of the transmitter $(R_{0T}\tau_{0T})$ in terms of the receiver (R_{0R}, τ_{0R}). After linearization new phase term depends on (R_{0T}, τ_{0T}). The linear expression of the complete scene is given in

equation (4.10). The first phase term as given in equation (4.11) is invariant of range and azimuth and can be taken out from the integral. Later, this space invariant term of linearized phase is compensated by multiplying spectrum with its conjugate $\Psi^*_{CS0}(f, f_\tau)$. The remaining bistatic spectrum is expressed in equation (4.21).

4. Next step is to perform a SIFT in range. The basic principle is symbolized as [5]:

$$S(A\ f) \xrightarrow{SCALED\quad INVERSE\quad FT} \frac{1}{\left|\det(A)\right|} s(t) \tag{4.22}$$

From equation (4.21), it is clear that back scattering coefficient term is scaled and shifted in range. First we consider one dimension of backscattering coefficient spectrum, which is dependent on range frequency f, we can write:

$$\sigma\left(r, A_{Az}(f) + B_{Az} f_\tau\right) = \int_{-\infty}^{+\infty} \sigma\left(f', A_{Az}(f) + B_{Az} f_\tau\right) e^{j2\pi r f'} df' \tag{4.23}$$

$$let\ \ f' = B_{Ra} x\ \ ;\ \ df' = B_{Ra} dx$$

$$\sigma\left(r, A_{Az}(f) + B_{Az} f_\tau\right) = \int_{-\infty}^{+\infty} \sigma\left(B_{Ra} x, A_{Az}(f) + B_{Az} f_\tau\right) e^{j2\pi r B_{Ra} x} B_{Ra} dx$$

$$let\ \ x = f + A_{Ra}/B_{Ra}\ \ ;\ \ dx = df$$

$$\sigma\left(r, A_{Az}(f) + B_{Az} f_\tau\right) = B_{Ra} \int_{-\infty}^{+\infty} \sigma\left(A_{Ra} + B_{Ra} f, A_{Az}(f) + B_{Az} f_\tau\right) e^{j2\pi r\left[A_{Ra} + B_{Ra} f\right]} df$$

$$= B_{Ra} e^{j2\pi A_{Ra} r} \int_{-\infty}^{+\infty} \sigma\left(A_{Ra} + B_{Ra} f, A_{Az}(f) + B_{Az} f_\tau\right) e^{j2\pi r B_{Ra} f} df$$

The scaling and shift terms are expressed in equation (4.16). The scaling in range is corrected using a SIFT and final expression is given as follows:

$$\sigma\left(r, A_{Az}(f) + B_{Az} f_\tau\right) = H_{2Ra}(r, f_\tau) \int_{-\infty}^{\infty} W(f, f_\tau) H_{1Ra}(f, f_\tau) df \tag{4.24}$$

$$H_{1Ra}(f, f_\tau) = e^{j2\pi r B_{Ra}(f_\tau) f}$$

$$H_{2Ra}(r, f_\tau) = B_{Ra}(f_\tau) e^{j2\pi r A_{Ra}(f_\tau)}$$

After these steps 1D-FFT is required in range.

5. In the next step, a SIFT is performed in azimuth. Here, we consider the other dimension of the backscattering coefficient spectrum, which is dependent on azimuth frequency f_τ, we can write:

$$\sigma(f,\tau_{0R}) = \int_{-\infty}^{+\infty} \sigma(f,f'_\tau) e^{j2\pi\tau_{0R}f'_\tau} df'_\tau \tag{4.25}$$

$$let \;\; f'_\tau = B_{Az}y \;\; ; \;\; df'_\tau = B_{Az}dy$$

$$\sigma(f,\tau_{0R}) = \int_{-\infty}^{+\infty} \sigma(f,B_{Az}y) e^{j2\pi\tau_{0R}B_{Az}y} B_{Az}dy$$

$$let \;\; y = f_\tau + A_{Az}/B_{Az} \;\; ; \;\; dy = df_\tau$$

$$\sigma(f,\tau_{0R}) = B_{Az}\int_{-\infty}^{+\infty} \sigma(f,A_{Az}+B_{Az}f_\tau) e^{j2\pi\tau_{0R}[A_{Az}+B_{Az}f_\tau]} df_\tau$$

$$= B_{Az}e^{j2\pi A_{Az}\tau_{0R}} \int_{-\infty}^{+\infty} \sigma(f,A_{Az}+B_{Az}f_\tau) e^{j2\pi\tau_{0R}B_{Az}f_\tau} df_\tau$$

The scaling and shift are corrected in azimuth and final expression is represented as below:

$$\sigma(f,\tau_{0R}) = H_{2Az}(f,\tau_{0R}) \int_{-\infty}^{\infty} \sigma(f,A_{Az}(f)+B_{Az}f_\tau) H_{1Az}(f,f_\tau) df_\tau \tag{4.26}$$

$$H_{1Az}(f,f_\tau) = e^{j2\pi\tau_{0R}B_{Az}f_\tau}$$

$$H_{2Az}(f,\tau_{0R}) = B_{Az}e^{j2\pi\tau_{0R}A_{Az}(f)}$$

6. The above equation represents backscattering coefficient in range frequency and azimuth time domain. Performing 1D-IFFT in range gives us complex image represented in terms of backscattering coefficient $\sigma(r,\tau_{0R})$ in range and azimuth time domain.

4.4 Focusing Results of Azimuth Invariant Configurations

The bistatic SAR configurations can be categorized into two groups, azimuth variant and azimuth invariant. In this section, we consider Azimuth Invariant Configurations (AIC). In these configurations, the baseline between transmitter and receiver remains constant during the flight or data acquisition. Examples of such configurations are tandem and TI configurations. In tandem configurations both transmitter and receiver follow each other along same path and distance between them remains constant during the data acquisition as shown in Figure 18. In TI configurations, the transmitter and receiver flies parallel to each other but the offset between them remains constant as shown in Figure 21.

The AICs are also called constant offset configurations. The system parameters $a_0 = (\tau_{0T} - \tau_{0R})$; $a_2 = R_{0T}/R_{0R}$ which represent the azimuth time difference and slant range ratio of transmitter and receiver at PCA are constant. As a_0, a_2 are constant, the processing algorithm given in sections 4.2 and 4.3 can be simplified accordingly. Azimuth scaling correction is also unnecessary in constant offset configurations. As the transmitter and receiver contribute equally towards the bistatic phase term, we use a weighting factor of $\mu = 1$ [55].

4.4.1 Bistatic Airborne Experiment

As an example for AICs, we consider an airborne bistatic experiment performed by Fraunhofer-Institute of High Frequency Physics and Radar techniques FHR (former FGAN) in November 2003 [9], [19], [25]. The transmitter sensor AER-II (Airborne Experimental Radar) was carried by Dornier Do-228 platform and PAMIR (Phased Array Multifunctional Imaging Radar) is used as receiver (carried by Transall C-160 platform). Both platforms had parallel trajectories (TI configuration) and were flown at average height of $2500m$ with velocities of $98\,m/s$. They shared a common bandwidth of 300 *MHz* (X-band) and had a bistatic angle of 13°. The imaging site was Oberndorf am Lech, Germany. We use our proposed processing algorithm for focusing of the raw data obtained during this experiment. Some important parameters of the experiment are given in Table 8.

Table 8: Bistatic Airborne Experiment (Azimuth Invariant TI Configuration)

Parameters	**Transmitter**	**Receiver**
Velocity	98 m/s	
Pulse duration	3 μs	
Carrier frequency	10.13 GHz	10.17 GHz
Bandwidth	300 MHz	
PRF	1250 Hz	
Range Sampling Rate	400 Msamples/s	
Depression Angle	55°	42°
Slant Range	2906 m	3590 m
Distance between planes	1050 m	

4.4.2 Results and Comparison

The raw data of bistatic airborne experiment is focused using the algorithm given in sections 4.2 and 4.3. As this raw data is collected over a wide range, we consider only a part of it (which is good combination of vegetations and buildings) for focusing. The final image obtained after using our bistatic focusing algorithm is given in Figure 35 (right). As a comparison we also provide an optical image (from Google maps) of the same scene in Figure 35 (left).

Figure 35: Focusing Results of Bistatic Azimuth Invariant Configurations: [Left] Optical Image (Google Maps), [Right] Bistatic SAR Image using a SIFT

After comparing both images we can see that the image is well focused and all the important details can be seen in bistatic SAR image which are present in the optical image.

4.5 Focusing Results of Azimuth Variant Configurations

Azimuth Variant Configurations (AVC) also called as the general configurations ([1], [8], [19]), are those where baseline between transmitter and receiver varies over the azimuth time. In such configurations, the transmitter and receiver can move with different velocities and along different directions. We consider hybrid configurations as an example for AVC. In hybrid configurations a satellite is used as transmitter and an aircraft is used as receiver. As there is a large difference between the velocities and altitudes of the transmitter and receiver, we consider the weighted azimuth contribution of transmitter and receiver phases in LBF [55].

In the next subsections, we consider two hybrid bistatic SAR experiments and use their raw data for our processing algorithm. These experiments were performed by

Fraunhofer-FHR using TerraSAR-X satellite as transmitter and PAMIR system as receiver [29]. The transmitter and receiver have almost parallel flight tracks. During the flight, PAMIR was in the main beam of the satellite to receive simultaneously the echoed signal from the scene and the direct signal from the satellite using an additional antenna mounted on the aircraft. The differential Global Positioning System (GPS) and Inertial Navigation System (INS) were used on board to provide an accurate altitude and position information [29]. Tracking and Imaging Radar (TIRA) was also used to measure the satellite's orbit parameters accurately and also it's expected time of arrival before the data acquisition and then to compare it with the values predicted by the satellite [30]. This information along with the on board navigation system of aircraft helped for footprints synchronization of the transmitter and receiver and for navigating the aircraft to fly over the scene along with the satellite at accurately predetermined time.

In these experiments, continuous data acquisition was not possible due to limited data rate of the recording unit [29]. Therefore an appropriate gated receiving mode has been used. The data intake is based on pulse synchronization. The direct satellite signal is used to synchronize the receiver. The direct TerraSAR-X pulses are detected by Digital Phased Locked Loop (DPLL) and are used to trigger receiving unit with a delay, which incorporates the two way travel time of echoed signal [30]. After being triggered, the receiver operated with a fixed PRF, which is one third of PRF of the transmitter for proper sampling of the received signal.

4.5.1 Hybrid Experiment 1

This experiment was performed in July 2008 [29]. Both the transmitter and receiver have X-band phased array antennas with the ability of beam steering. The transmitter was operated in sliding spotlight mode and receiver in stripmap mode with common range bandwidth of 150 MHz. In stripmap mode, one third of the antenna size (one sub aperture) of PAMIR was used to increase azimuth scene extent. The receiver's azimuth beam width was increased by 6° to increase the azimuth scene extent, which on other hand decreases the SNR. Operating in stripmap mode has longer illumination time for the targets and therefore has better azimuth resolution. The test site was Pommersfelden, Germany, a good combination of urban area, vegetation and a castle (Weißenstein). Some important parameters of this experiment are given in Table 9.

Table 9: Hybrid Bistatic SAR Experiment (Pommersfelden, Germany)

Parameters	**Transmitter**	**Receiver**
Velocity	7600 m/s	95 m/s
Altitude	515 km	3300 m
Incidence Angle	47°	70°
Azimuth Beam width	0.33°	6°
Bandwidth	150 MHz	
PRF	3798.61 Hz	1266.22 Hz
Slant Range	723 km	9900 m

4.5.1.1 Preprocessing of Raw Data

The raw data obtained in these experiments needs to undergo some preprocessing, before the actual frequency domain focusing algorithm can be applied. Two preprocessing steps have been taken into account.

4.5.1.1.1 Correction of Drift in Raw Data

As mentioned earlier, continuous recording of the received data was not possible due to limited data rate of the recording unit. Therefore, the PRF of the receiver was chosen accordingly to avoid ambiguities in range and azimuth. The PRF of the transmitter is approximately three times larger than that of receiver [29]. This mismatching of PRF introduces a constant drift in the range lines along azimuth of the raw data. This drift must be corrected before applying a frequency domain focusing algorithm. It is corrected along azimuth by multiplying each range line with a phasor given in the following equation.

$$g'(f,\tau) = g(f,\tau)e^{-j2\pi(f+f_0)d_f} \tag{4.27}$$

Here, d_f is drift factor and is given as:

$$d_f = 3\times PRI_T - PRI_R \tag{4.28}$$

4.5.1.1.2 Unfolding of azimuth spectrum

After range compression and correction of the drift in the raw data, azimuth spectrum is unfolded to avoid aliasing in azimuth. If the PRF is not high enough to properly sample the signal in azimuth according to its bandwidth characteristics, the spectral folding is caused due to limited sampling frequency. This limitation can be solved by replicating the data spectrum in azimuth direction by the number of times of the folded replica [82].

In hybrid experiments [29], the raw data was down sampled on receiving and is therefore up sampled before processing to avoid aliasing in azimuth.

4.5.1.2 Focusing Results

The raw data collected during this experiment is processed using our frequency domain focusing algorithm. The image obtained is given in Figure 36. We use back projection algorithm to compare results with our frequency domain algorithm. The back projection algorithm is a time domain processing approach.

Figure 36: Focusing Result of Hybrid Experiment (Pommersfelden) using Frequency Domain Focusing Algorithm

Figure 37: Focusing Result of Hybrid Experiment (Pommersfelden) using Back Projection Algorithm

Comparing the results in Figure 36 and Figure 37, we can say that our proposed focusing algorithm provides very good quality images in considerably shorter time and is approximately 30 times faster than back projection algorithm. We consider a cut out of castle area in the image, in order to see more details. In Figure 38, a comparison of the

castle using our focusing algorithm (right), back projection algorithm (left) and optical image (Google maps), is given. We can see a good comparison of trees, building structures and vegetation fields. Our frequency domain algorithm provides as good results as obtained from the back projection algorithm.

Figure 38: Comparison of Castle (Weißenstein) Image (Left) Back Projection Algorithm (Middle) Google Maps (Right) Frequency Domain Focusing Algorithm.

A quantitative comparison of histograms of the normalized amplitude of the frequency and time domain processed images (Figure 38) is shown in Figure 39. A histogram is generated based on the grayscale (8-bit) normalized absolute value of the image. The solid and dotted lines represent frequency domain and back projection images respectively. It is quiet interesting to observe that the shape and height of the distributions are almost similar. The standard deviation of the distributions obtained from the frequency and time domain processing algorithms are 15.22 and 14.85 respectively. A small shift in the distributions may arise due to higher grayscale value of a pixel in one image than the other.

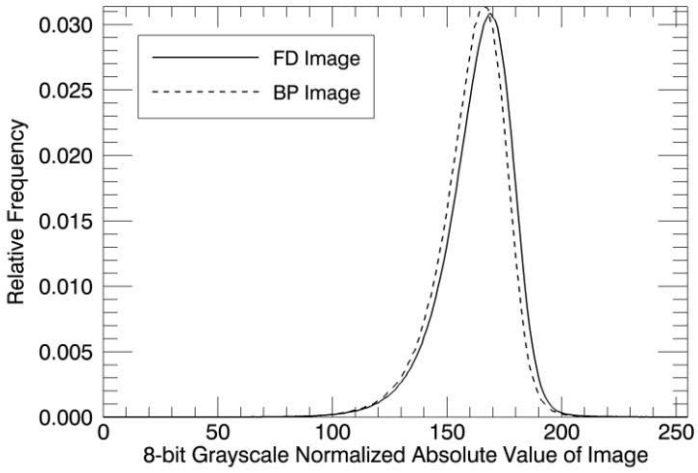

Figure 39: Histogram of the Normalized Amplitude of the Time and Frequency domain Processed Images

In the next step we investigate whether our frequency domain processing approach is phase preserving which implies that the pixel's phase in the focused image is propotional to its distance at point of closest approach. We plot the interferogram of the back projection and the frequency domain image. This is done by coregistration of the time and frequency domain image. The coregistration is the rescaling and space variant shift of one image towards the other. The interferometric phase and its overlap on the intensity image and is shown in the Figure 40.

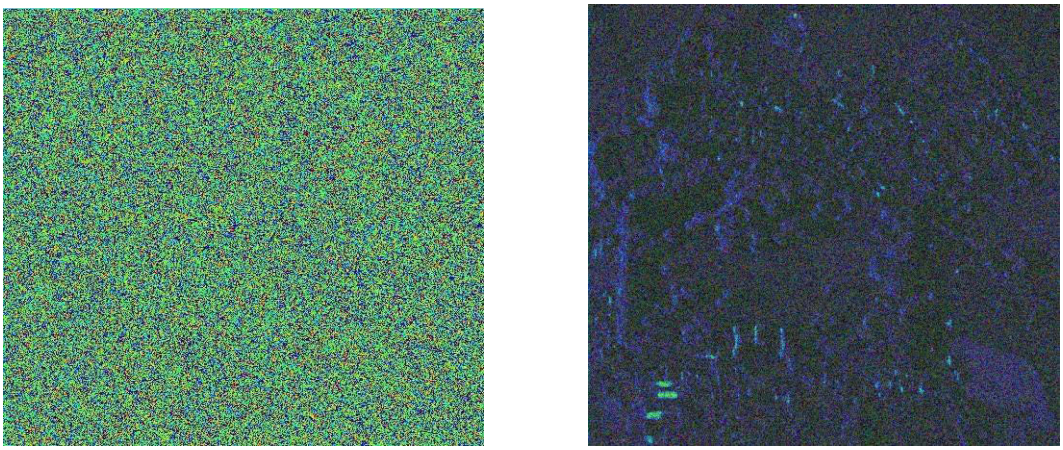

Figure 40: Interferometric Phase of the Time and Frequency Domain Images and its Overlap on the Intensity Image

In the above figure, the phase difference of the time and frequency domain processed images appears random and we can not find correlation between the results. The time and frequency domain images are processed in different geometries and they are coregistered afterwards by locating the similar portions in both images and then calculating the shifting vectors. In the amplitude image comparison we can see similar results with same focusing quality.

4.5.2 Hybrid Experiment 2

Another hybrid experiment was performed in March 2009 [29]. The basic difference between these two experiments is the receiver's operating mode and the common range bandwidth. In this experiment, PAMIR used full antenna size and hence reduced azimuth beam width (2.5°) but have a better SNR. TerraSAR-X and PAMIR operated in sliding and inverse sliding spotlight mode respectively, to achieve a larger azimuth scene extent. This configuration is called double sliding spotlight mode [29], where transmitter and receiver both have beam steering capabilities. It has disadvantage of shorter illumination time for targets, which leads to a lower azimuth resolution. The antenna footprint of the receiver moves four times faster than its own velocity for a better compromise between azimuth scene extent and the azimuth resolution [29]. The common

bandwidth of transmitter and receiver in range is 300 *MHz* and it is the maximum bandwidth of the TerraSAR-X. Some important parameters of this experiment are given in Table 10.

Table 10: Hybrid Bistatic SAR Experiment (Niederweidbach, Germany)

Parameters	**Transmitter**	**Receiver**
Velocity	7600 m/s	95 m/s
Altitude	515 km	3400 m
Incidence Angle	55.3°	65°
Azimuth Beam width	0.33°	2.5°
Bandwidth	300 MHz	
PRF	4374.45 Hz	1458.15 Hz
Slant Range	844 km	8000 m

The imaging site was Niederweidbach, Germany. The raw data obtained is processed using our frequency domain processing algorithm and results are shown in Figure 41.

Figure 41: Focusing Result of Hybrid Experiment (Niederweidbach) using Frequency Domain Focusing Algorithm

Figure 42: Optical Image (Google Map) of Niederweidbach

We compare our result with an optical image (Google map) shown in Figure 42 and can well distinguish highways, roads, fields, forestation, houses, factory and stream. Hence we can say that our frequency domain focusing algorithm provides very good quality images.

4.6 Conclusions

In this chapter, we have presented a general processing algorithm based on BPTRS using a SIFT for focusing a complete scene. We have applied our focusing algorithm for azimuth variant and invariant configurations. In AICs we have considered an airborne-airborne experiment. As there is no considerable difference in the altitudes and velocities of the transmitter and receiver, therefore we have considered equal azimuth weighting of transmitter and receiver phases. In AVCs, we have investigated spaceborne-airborne experiments. Due to large difference between the altitude and velocities of transmitter and receiver, we have considered weighted azimuth contributions of the transmitter and receiver phases. The focusing results of the bistatic SAR experiments show that our proposed focusing algorithm works very well for azimuth variant and invariant configurations.

5 Stationary Receiver Configurations

5.1 Introduction

This chapter presents bistatic stationary receiver configurations. In these configurations, the transmitter moves along a trajectory and illuminates the scene, while the receiver remains stationary with its antenna pointing towards the illuminated scene. This scenario is a special case of AVCs, where only the moving transmitter contributes to the azimuth modulation. Bistatic stationary receiver configurations are inexpensive to build as compared to the moving receiver platform and can provide high resolution bistatic SAR data at reasonable cost. Also, they can be easily extended to multiple receiving channels for interferometric and polarimetric SAR applications.

The stationary receiver/transmitter with moving transmitter/receiver has been considered in various publications. In [41], a nonlinear chirp scaling is used to process bistatic ground based stationary receiver and moving transmitter operating in stripmap mode. The Range Cell Migration Correction (RCMC) is done in azimuth time domain. A nonlinear chirp perturbation function is used to equalize the frequency modulation rates of targets at the same range gate. Bistatic interferometry using stationary receiver configurations is described in [68] for the generation of DEMs. A hybrid SAR processing method for bistatic stationary configurations is presented in [71]. A Fourier based convolution is used to partially process the data and residual errors are corrected by using time varying filter. In [62], a wave number domain algorithm is used to process stationary transmitter with moving receiver configuration and results of simulated and real bistatic SAR data are provided. A sub-aperture range Doppler algorithm is used to process the stationary receiver configurations in [72]. A stationary receiver system SABRINA (SAR Bistatic Fixed Receiver for Interferometric Applications) is used with a moving C-band SAR satellite (Envisat and ERS-2). For each transmitted pulse, a bistatic slant range map is calculated from DEM of the illuminated scene. The image is then divided into sub-apertures, the RCMC is performed in range Doppler domain and the azimuth compression is performed in two steps [72]. It has been used for the interferometric applications in [73].

In 2009, the Center for Sensor System (ZESS) at the University of Siegen developed an X-band receiver system (HITCHHIKER) to perform bistatic high resolution SAR spaceborne/stationary experiments. This passive receiver system works with TerraSAR-X satellite operated in sliding spotlight mode. The details of hardware setup and experiments are given in [69], [70]. Different experiments were conducted in the cities of Siegen and Koblenz and raw data is processed with modified back projection algorithm

and quick look processor. These experiments have also been investigated for polarimetric and interferometric applications [11], [12].

A geometrical model for stationary receiver configurations, hardware implementation and data acquisition are described in sections 5.2 and 5.3 respectively. A bistatic point target reference spectrum is derived in section 5.4. A frequency domain focusing algorithm is implemented in section 5.5 to focus the experimental data obtained in these experiments. A comparison of the results with back projection algorithm and conclusions are drawn in sections 5.6 and 5.7 respectively.

5.2 Geometrical Model

The bistatic SAR geometry for stationary receiver configurations is illustrated in Figure 43. The stationary receiver is located on a high mountain or high building top and is facing towards the scene illuminated by the TerraSAR-X satellite operating in sliding spotlight mode with a high bandwidth of $300\ MHz$. In this figure, the receiver has two channels, one antenna points towards the satellite for direct reception of the transmitted signal and second antenna is directed toward the scene for the reception of backscattered signals. At any azimuth time instant τ, the transmitter's and the receiver's slant ranges are denoted by R_T and R_R. Here, R_D is the slant range of directly received transmitter signal. The transmitter's slant range and azimuth time at PCA are denoted as R_{0T} and τ_{0T} respectively.

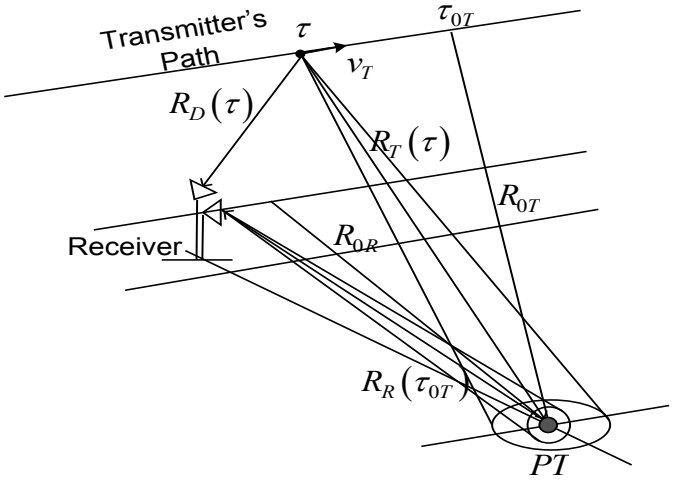

Figure 43: Stationary Receiver Configuration

5.3 Hardware Implementation and Data Acquisition

The receiver system, HITCHHIKER comprises three main units, the RF-front end, the digitizer and the computational unit [69], [70]. In earlier experiments, two identical horn

antennas were used for the reception of direct signal and backscattered echoes. The received signal is amplified and is band pass filtered and mixed with an Intermediate Frequency (IF). IQ demodulation is done using signal processing.

The transmitter and receiver are synchronized using the direct channel and is also used to trigger the acquisition window. A timestamp is saved at the occurrence of each trigger and is used to synchronize the acquisition window to the transmitter's PRF. The received data through direct channel observes a drift due to motion of the transmitter and stationary nature of the receiver. More details on hardware implementation and data acquisition are given in [69], [70].

5.4 Bistatic Point Target Reference Spectrum

The geometry of stationary receiver configuration is shown in Figure 43. The BPTRS derived in section 2.5 can be modified for stationary receiver configurations. The bistatic slant range is sum of transmitter's and receiver's slant ranges and is given as:

$$\begin{aligned} R_B(\tau) &= R_T(\tau) + R_R(\tau_{0T}) \\ &= \sqrt{R_{0T}^2 + v_T^2(\tau - \tau_{0T})^2} + \sqrt{R_{0R}^2 + v_T^2 \tau_{0T}^2} \end{aligned} \tag{5.1}$$

As we can see from the above equation, the slant range of receiver is independent of varying azimuth time τ .The received signal in range and azimuth time domain from PT is written as:

$$g_l\left(t, \tau, R_{0R}, \tau_{0T}\right) = \sigma\left(R_{0R}, \tau_{0T}\right)\omega(\tau - \tau_c)\, s_l(t - t_0)\, e^{-j2\pi f_0 t_0} \tag{5.2}$$

Where, σ is the backscattering coefficient representing brightness of a PT. w is a rectangular window with center time τ_c representing composite antenna pattern. s_l is the transmitted signal and t_0 is the two way propagation delay time and is given as:

$$t_0(\tau) = \frac{R_B(\tau)}{c_0} \tag{5.3}$$

After performing Fourier transformation over range time t and azimuth time τ, the BPTRS in 2-D frequency domain is represented as follows:

$$G_l\left(f, \tau, R_{0R}, \tau_{0T}\right) = \sigma\left(R_{0R}, \tau_{0T}\right)\omega(\tau - \tau_c)\, S_l(f)\, e^{-j2\pi(f + f_0)t_0} \tag{5.4}$$

$$G_l\left(f, f_\tau, R_{0R}, \tau_{0T}\right) = \sigma\left(R_{0R}, \tau_{0T}\right) S_l(f)\, e^{-j2\pi \frac{(f+f_0)}{c_0} R_R(\tau_{0T})} \int_{-\infty}^{\infty} \omega(\tau - \tau_c)\, e^{-j2\pi\left[\frac{(f+f_0)}{c_0} R_T(\tau) + f_\tau \tau\right]} d\tau$$

As the receiver is stationary, only transmitter contributes to the bistatic phase term and is given as:

$$\phi_B(\tau) = 2\pi \frac{(f+f_0)}{c_0} R_T(\tau) + 2\pi f_\tau \tau \tag{5.5}$$

Now, we apply PSP and expand the bistatic phase using second order Taylor's expansion around common point of stationary phase $\tilde{\tau}_s$ and is given as:

$$\phi_B(\tau) \simeq \phi_B(\tilde{\tau}_s) + \frac{1}{2}\ddot{\phi}_B(\tilde{\tau}_s)(\tau - \tilde{\tau}_s)^2 \tag{5.6}$$

The first derivative of bistatic phase at PSP is zero.

$$\left.\frac{d\phi_B(\tau)}{d\tau}\right|_{\tau=\tilde{\tau}_s} = 0 \tag{5.7}$$

Equation (5.4) can be simplified using equation (5.6) as follows:

$$G_l\left(f, f_\tau, R_{0R}, \tau_{0T}\right) = \sigma\left(R_{0R}, \tau_{0T}\right)\omega(\tau - \tau_c) S_l(f) \frac{\sqrt{2\pi}}{\sqrt{\ddot{\phi}_B(\tilde{\tau}_s)}} e^{-j2\pi\left[\frac{(f+f_0)}{c_0} R_R(\tau_{0T}) + \phi_B(\tilde{\tau}_s)\right]} e^{-j\pi/4} \tag{5.8}$$

The PSP and bistatic phase at PSP can be obtained using equations (5.1), (5.5), (5.6) and (5.7) and are derived as follows:

$$\begin{aligned}
\tilde{\tau}_s &= \tau_{0T} - \frac{f_\tau c_0}{2v_T^2} \frac{R_{0T}}{F_T^{1/2}(f, f_\tau)} \\
\phi_B(\tilde{\tau}_s) &= \pi f_\tau \tau_{0T} + \frac{2\pi R_{0T}}{c_0} F_T^{1/2}(f, f_\tau) \\
\ddot{\phi}_B(\tilde{\tau}_s) &= \frac{2\pi v_T^2}{c_0 R_{0T}} \frac{F_T^{3/2}(f, f_\tau)}{(f+f_0)^2}
\end{aligned} \tag{5.9}$$

Here F_T is the transmitter's frequency history and is defined as:

$$F_T(f, f_\tau) = (f+f_0)^2 - \frac{\mu^2 f_\tau^2 c_0^2}{4v_T^2} \tag{5.10}$$

Using equation (2.32) for stationary receiver configurations, the weighting factor is obtained as $\mu = 2$. We substitute equation (5.9) into (5.8). The final expression of BPTRS for stationary receiver configurations is given as:

$$G_l\left(f, f_\tau, R_{0R}, \tau_{0T}\right) = \sigma\left(R_{0R}, \tau_{0T}\right)\omega\left(\tau - \tau_c\right)S_l\left(f\right)\sqrt{\frac{\left(f+f_0\right)^2 c_0 R_{0T}}{v_T^2 F_T^{3/2}\left(f, f_\tau\right)}} \tag{5.11}$$
$$e^{-j2\pi\frac{(f+f_0)}{c_0}R_R(\tau_{0T})}\; e^{-j2\pi\frac{F_T^{1/2}(f,f_\tau)}{c_0}R_{0T}}\; e^{-j[\pi f_\tau \tau_{0T} + \pi/4]}$$

In stationary receiver configurations, only the moving transmitter contributes to the azimuth modulation. The bistatic phase term in equation (5.5) has only one hyperbolic range history of the moving platform. In this configuration, the stationary platform introduces a range shift to all the PTs located at the same range parallel to the azimuth. All these PTs at the same range have same Doppler histories and their RCM trajectories follow a hyperbolic path along the azimuth axis. Frequency domain focusing algorithms like range Doppler algorithm can not directly process such configurations due to the hyperbolic distribution of range histories of the PTs located at same range.

The first phase term in equation (5.11) represents the range shift along azimuth of PTs located at the same range. It is a linear function of range frequency and a non-linear function of the coordinates R_{0R} and τ_{0T}. Due to this non-linear coordinate dependence, this phase term can not be entirely corrected using a SIFT in 2-D frequency domain. The second phase term represents the contribution by moving transmitter and contains a Doppler dependent RCM.

5.5 Focusing Algorithm

The implementation of focusing algorithm for stationary receiver configurations consists of following steps and is shown in Figure 44.

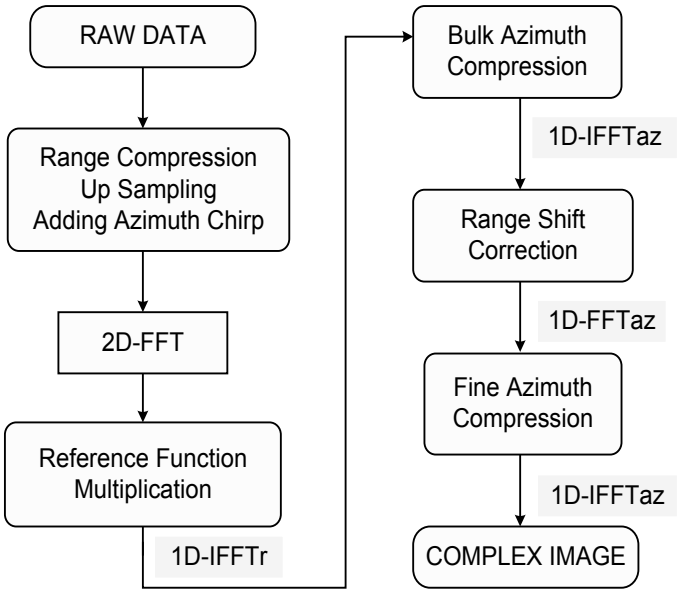

Figure 44: Block Diagram of Focusing Algorithm (Stationary Receiver Configurations)

1. Pre processing: The raw data obtained from the stationary receiver experiments require some pre processing. The first part of which is range compression. The received signal W_0 is range compressed by multiplying it with the complex conjugate of the directly received transmitter's signal S_{DL} from the direct channel and is given as:

$$W(t,\tau) = IFFT_r\left[W_0(f,\tau) \times S_{DL}^*(f) \right] \tag{5.12}$$

Here, $W(t,\tau)$ is the range compressed raw data in the 2-D time domain. The deramping of data is performed in the range compression step. The directly received signal already contains the phase history of the trigger antenna with respect to the satellite position. Hence by multiplying with its complex conjugate, gives a bulk azimuth compression for the slant range of the transmitter and the same holds for the range migration. The second part of pre processing is the up-sampling of data and adding an azimuth chirp. The bandwidth of complete scene is greater than the sampling rate and PRF is not high enough to properly sample the signal in azimuth; therefore, azimuth signal is up-sampled. After up-sampling, we add an azimuth chirp depending on the varying distance from the satellite to trigger antenna, in order to achieve a constant PRF. The correction of shift in the range lines introduced due to the moving transmitter and stationary receiver is expressed as:

$$W(f,\tau).\mathrm{e}^{-j2\pi(f+f_0)\Delta t} \quad ; \quad \Delta t = \frac{\Delta R(\tau)}{c_0} \tag{5.13}$$

In this step, we have added a range phasor and range migration to the received raw data, which is corrected later in the reference function multiplication step.

2. A 2-D Fourier transformation is performed to transform the raw data into 2-D frequency domain. The next important step is the reference function multiplication. The pre processed data is multiplied with a reference function phasor in range and azimuth frequency domain and is expressed as follows:

$$H_{RFM}(f,f_\tau) = e^{j2\pi\frac{R_m}{c_0}F_T^{1/2}(f,f_\tau)} \tag{5.14}$$

The reference slant range R_m is the closest slant range from scene center to the transmitter's track. It compensates the phase at R_m and the phase due to azimuth frequency modulation [76]. The transmitter's frequency history $F_T(f,f_\tau)$ given in (5.10) has a square root term in the phase of BPTRS and is non-linear in azi-

muth frequency f_τ. $F_T(f, f_\tau)$ is expanded using first order Taylor's expansion at range frequency f and is given as follows:

$$F_T^{1/2}(f, f_\tau) \simeq f_0 \sqrt{1 - \frac{\mu^2 f_\tau^2 c_0^2}{4 v_T^2 f_0^2}} + f \left[1 \Big/ \sqrt{1 - \frac{\mu^2 f_\tau^2 c_0^2}{4 v_T^2 f_0^2}} \right] \\ = f_0 D(f_\tau) + f \left[1 / D(f_\tau) \right] \tag{5.15}$$

The first term of above equation is the range shift and is dependent on azimuth frequency f_τ. The second term is the range scaling and has azimuth frequency dependence.

3. The azimuth compression is performed into two steps; first we perform bulk azimuth compression followed by fine azimuth compression. The signal is transformed into range Doppler domain and the bulk azimuth compression is expressed as below:

$$H_{BAC}(f_\tau) = e^{j2\pi \frac{(R_0 - R_m + n\delta_{ra})}{c_0} f_0 D(f_\tau)} \tag{5.16}$$

Here, R_0 is the slant range of the transmitter from beginning of the scene and δ_{ra} is the width of one range cell. After performing the bulk azimuth compression, a residual azimuth modulation still exists in the remaining phase term of equation (5.11) and is compensated in the fine azimuth compression step.

4. Next step is to correct the coordinate dependent range shift in range introduced because of the stationary receiver. The signal is converted into 2D time domain and range interpolation is used to correct the non-linear range shift to the range cell migration trajectories at the same range along azimuth. After this step, all targets with same Doppler histories are aligned along the same range gate.

5. The signal is again transformed into range Doppler domain for correcting the remaining azimuth modulation. The phasor for fine azimuth compression is given as follows:

$$H_{FAC}(f_\tau) = e^{j2\pi \frac{(R_{0T} - R_0)}{c_0} f_0 D(f_\tau)} \tag{5.17}$$

Here, R_{0T} is the transmitter's slant range at PCA. After performing inverse Fourier transformation in azimuth, the focused image is obtained.

5.6 Experimental Results

The stationary receiver experiments conducted at the University of Siegen using the HITCHHIKER stationary receiver system with the TerraSAR-X satellite, operating in sliding spotlight mode. In sliding spotlight mode, the antenna is steered continuously to illuminate a particular area of interest. The number of backscattered echoes is increased extensively as compared to stripmap mode. The overall azimuth bandwidth of the complete scene is the superposition of the individual bandwidths of all PTs in the scene. This high azimuth bandwidth of complete scene in spotlight mode demands high sampling rates in order to avoid under sampling effects. But on the other hand high sampling rates introduces ambiguities in the range. The techniques like de-ramping (or dechirping) are commonly used to reduce these high data rates [38]. As PRF is not high enough to sample the signal in azimuth properly, azimuth signal is up-sampled before applying any azimuth focusing techniques [82]. As transmitter is moving while receiver is stationary, this leads to a non constant PRF and a shift to the range lines along the azimuth. The receiving channel records the backscattered signal after it is being triggered by the arrival of pulse at the direct channel. This eliminates the main azimuth chirp, which is added in the pre processing step along with the correction of range shift along azimuth.

5.6.1 Experiment 1

The first experiment using the stationary receiver and TerraSAR-X was performed at the University of Siegen on September, 2009. The transmitter operated in high resolution spotlight mode. The incidence angles of transmitter and receiver are 53^{o} and 85^{o} respectively. The receiver was installed at the roof top of a high building (Adolf-Reichwein Campus, University of Siegen) approximately $100m$ above the ground level of scene. The receiver's antenna is directed to the east, towards the imaging site of Dreis-Tiefenbach, Siegen-Weidenau, Germany.

The raw data is processed with the proposed frequency domain focusing algorithm and result is shown in Figure 45. We process the same data set using a back projection algorithm and the image obtained is shown in Figure 46.

Figure 45: Focusing Result of Stationary Receiver Experiment (Dreis-Tiefenbach) using Frequency Domain Algorithm

Figure 46: Focusing Result of Stationary Receiver Experiment (Dreis-Tiefenbach) using Back Projection Algorithm

The presence of shadows in the image is due to hilly landscape of Dreis-Tiefenbach and large incidence angle of the receiver. On comparing the above two figures, we can say that our frequency domain algorithm produces as good quality images as obtained using back projection algorithm. The appearance of curved artifacts in the above images is due to high backscattered energy from an arbitrary point target during a small portion of the synthetic aperture. This high energy peak in the azimuth chirp remains uncompensated during the azimuth compression and is distributed along the iso-range lines, at all the equidistant points from the stationary receiver. Some parts of the scene (a factory and vegetation land) are considered for a more detailed comparison using both algorithms in Figure 47.

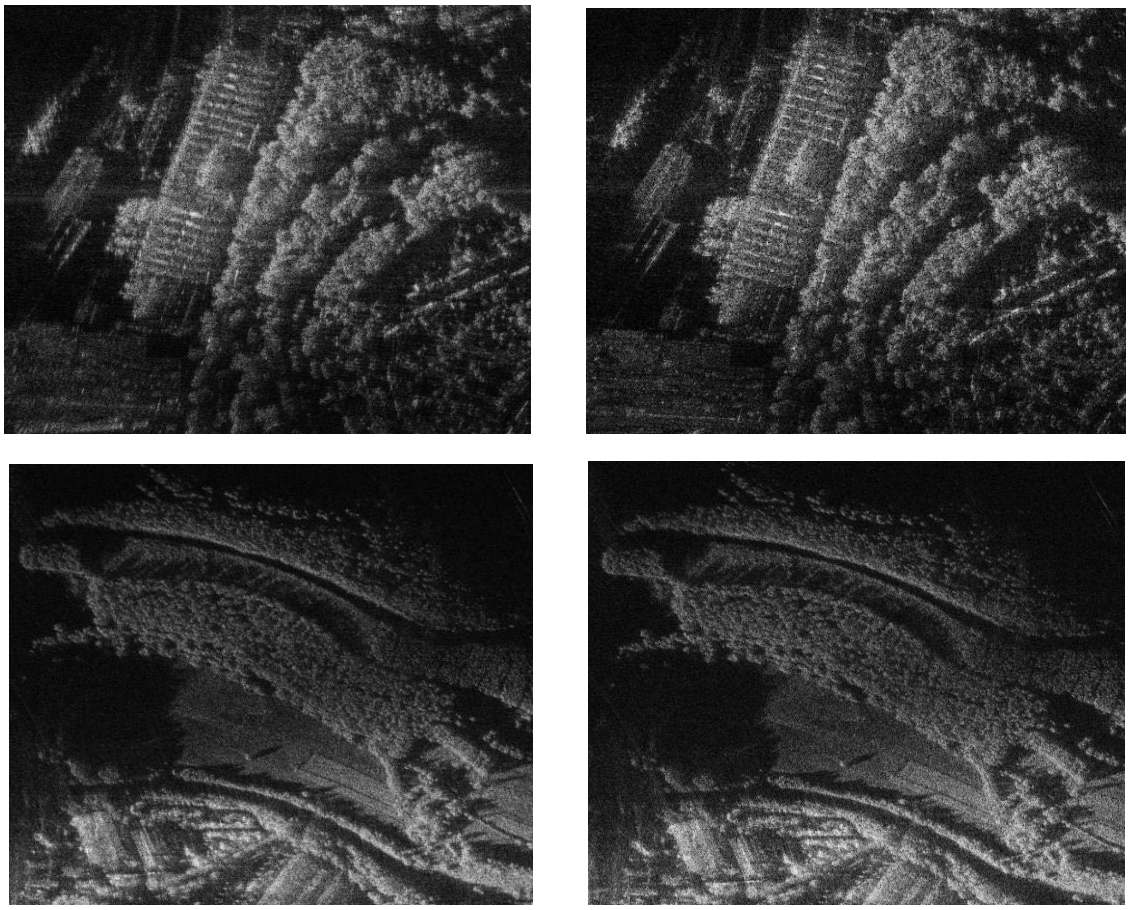

(A) Frequency Domain Algorithm (B) Back Projection Algorithm

Figure 47: Comparison of some parts of the scene (Dreis-Tiefenbach)

A quantitative comparison of the distributions of the time and frequency domain processed images is shown in Figure 48. We compare the histograms of the normalized amplitudes of the time and frequency domain processed images shown in Figure 45 and Figure 46. A histogram of the grayscale normalized absolute value of the image is generated. The solid and dotted lines represent back projection and frequency domain images respectively. We observe that the shape and height of both distributions are almost similar. The standard deviation of the distributions obtained from the frequency and time domain processing algorithms are 20.77 and 21.65 respectively, according to the 8-bit grayscale quantization. A small shift in the distributions may arise due to higher grayscale value of a pixel in one image than the other.

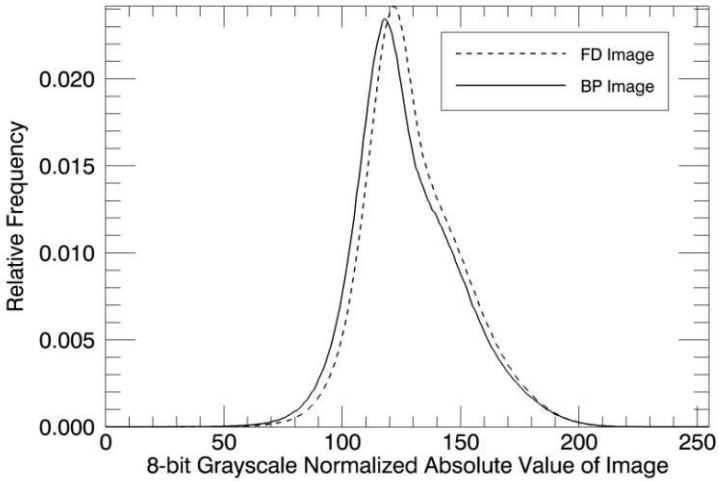

Figure 48: Histogram of the Normalized Amplitude of the Time and Frequency Domain Processed Images

As a next step we plot the interferogram of time and frequency domain processed images. After coregistration of time and frequency domain images, we plot the interferometric phase in Figure 49.

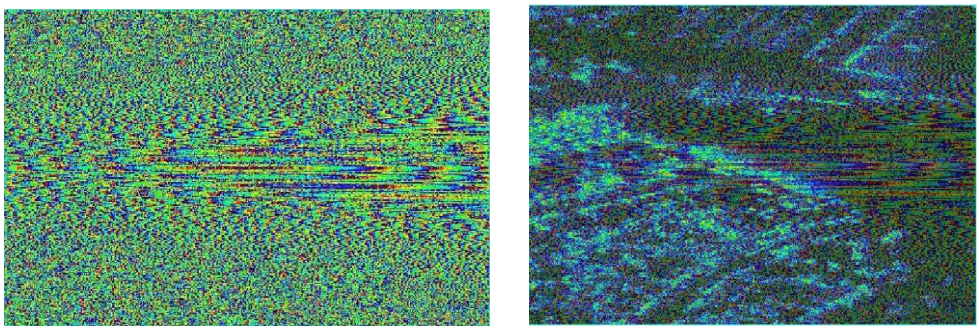

Figure 49: Interferometric Phase of the Time and Frequency Domain Images and its Overlap on the Intensity Image

Above figure shows some structures which are due to geometry of the 2D grid in back projection algorithm. Due to this regular grid in phase there are some dominant artifacts visible. We can not say that the frequency and time domain processed images are coherent due to these strong artifacts which are due to the geometry of the stationary receiver configuration. The amplitude image comparison shows same quality of focusing.

5.6.2 Experiment 2

Another stationary receiver experiment was performed at Ehrenbreitstein fort in the city of Koblenz, Germany on October, 2009. The focusing results of raw data using the frequency domain and back projection algorithm are shown in Figure 50 and Figure 51 respectively.

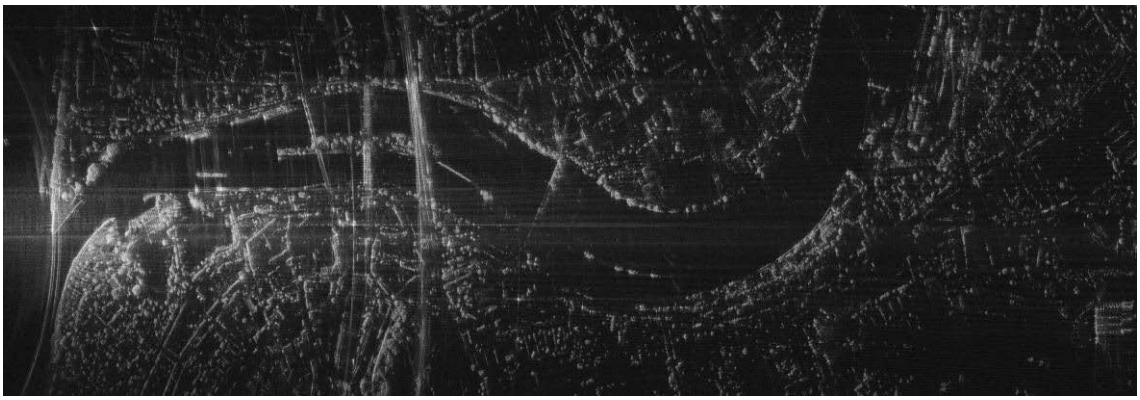

Figure 50: Focusing Result of Stationary Receiver Experiment (Koblenz) using the Frequency Domain Algorithm

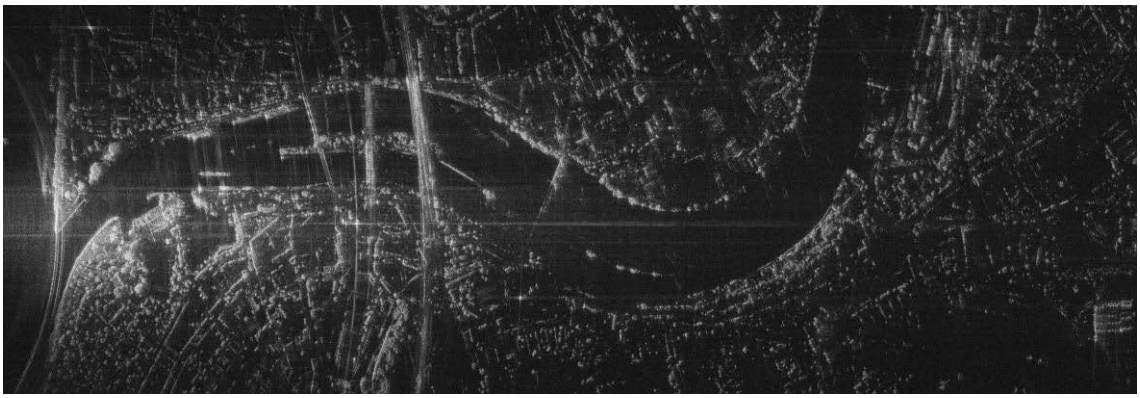

Figure 51: Focusing Result of Stationary Receiver Experiment (Koblenz) using Back Projection Algorithm

The bridges over the river are quiet prominent in the above images. As mentioned earlier, the curved artifacts in the image are due to high backscattered energy from a point target. It appears as a high energy peak in the azimuth chirp and distributes along the iso-range line, at all the equidistant points from the stationary receiver. A detailed comparison of the famous edge at the junction of two rivers Rhine and Mosel called 'Deutsches Eck' is shown in the Figure 52, using frequency and time domain algorithms.

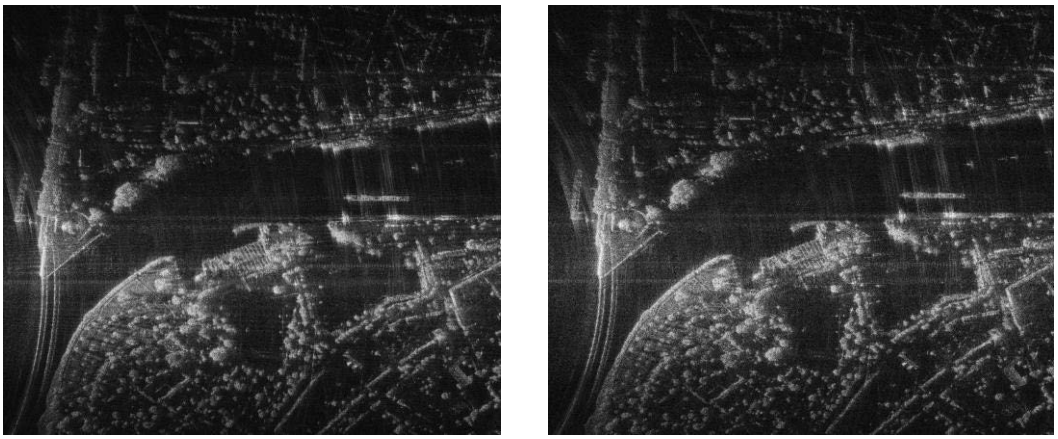

(A) Frequency Domain Algorithm (B) Back Projection Algorithm

Figure 52: Comparison of a part of the scene (Koblenz)

A quantitative comparison is provided for the time and frequency domain images shown in Figure 52, by comparing the histograms of their normalized amplitudes. We normalize the distribution by dividing the absolute values with the maximum amplitude. A histogram is generated based on the normalized absolute value of the image and is shown in Figure 53. The solid and dotted lines represent back projection and frequency domain images respectively. The grayscale (8-bit) values of the normalized amplitude of the images are plotted against their relative frequencies. It is quiet interesting to observe that the shape and height of the distributions are quite similar. The standard deviation of the distributions obtained from the frequency and time domain processing algorithms are 21.15 and 20.91 respectively. There is a small shift in the distributions which may arise due to higher grayscale value of a pixel in one image than the other.

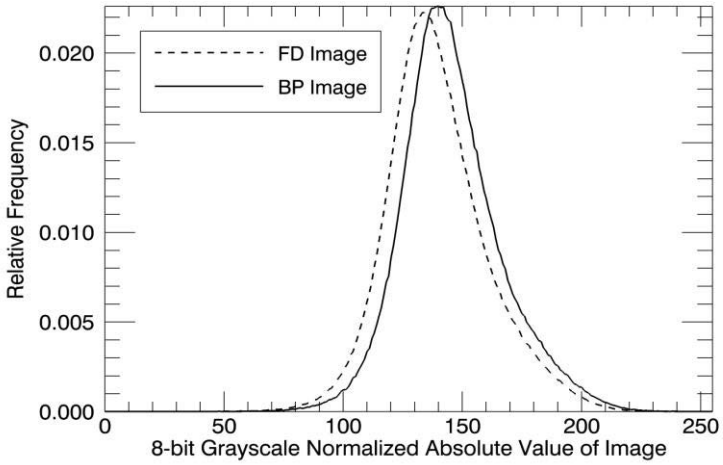

Figure 53: Histogram of the Normalized Amplitude of the Time and Frequency Domain Processed Images

We again plot the interferogram of time and frequency domain processed images. After coregistration of time and frequency domain images, we plot the interferometric phase and is shown in Figure 54.

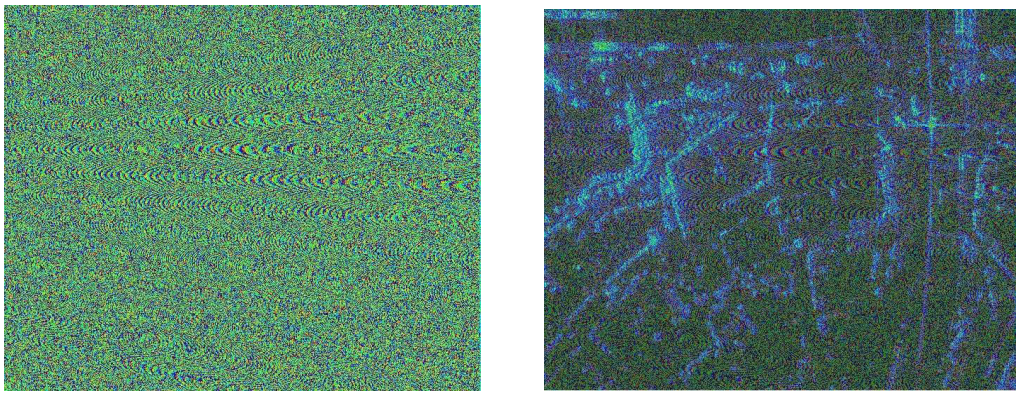

Figure 54: Interferometric Phase of the Time and Frequency Domain Images and its Overlap on the Intensity Image

In the above figure, we again observe some artifacts which are coming from the back projection algorithm and they are due to this specific geometry of the stationary receiver configurations. In the phase of the image processed by the back projection algorithm we can see these artifacts are starting from the position of the receiver in the image. Due to these strong artifacts we can not say that the frequency and time domain processed images are coherent. Although the amplitude image comparison shows that both time and frequency domain processing approaches give same focusing quality.

5.6.3 Interferometric Experiment

An interferometric experiment was performed in 2010, using a single transmitter (TerraSAR-X satellite) and three receiving antennas of the HITCHHIKER receiver system. One antenna was used to receive the direct signal from the satellite and the remaining two antennas were used to generate an interferogram of the illuminated scene. The satellite operated in spotlight mode with range bandwidth of $300MHz$. The two receiving antennas were separated by a vertical baseline of $90cm$ in a plane perpendicular to the satellite's velocity vector. The experiment was performed at the University of Siegen and other specifications of this experiment are similar as mentioned in section 5.6.1. The interferometric phase is generated due to the height variation of the receiving antennas.

Two high resolution SAR images are produced from the two receiving antennas. An interferogram is generated based on the phase difference between these images processed using a frequency domain algorithm and is shown in Figure 55. In Figure 56, the interferogram of the same data sets is generated by processing them using the back projection algorithm. Comparing these two figures, we can say that the data processed us-

ing our frequency domain algorithm produces very good quality interferograms in a comparably short time (the ratio of the processing time using frequency and time domain processing algorithms is 1 min : 132 mins). In Figure 57, the interferometric phase is overlaid on the radar intensity image.

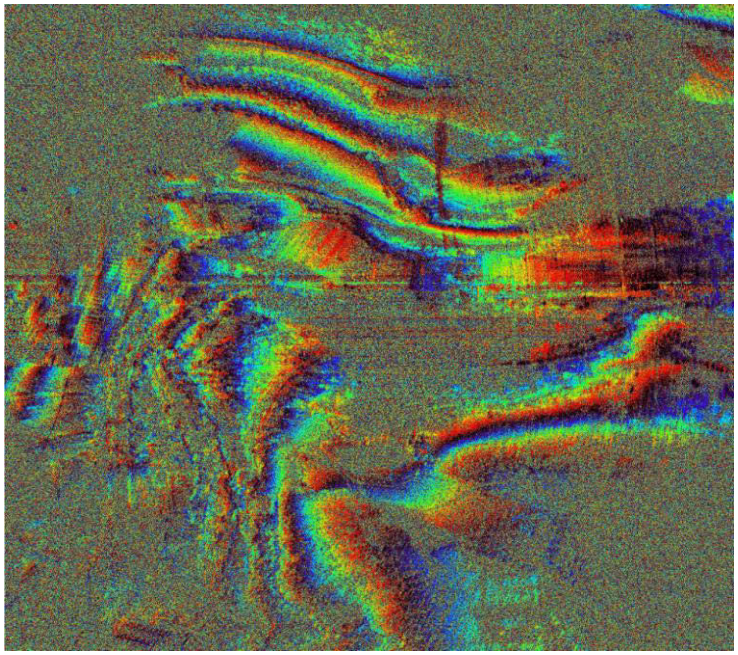

Figure 55: Interferogram of the Scene (Dreis-Tiefenbach) – Using Frequency Domain Algorithm

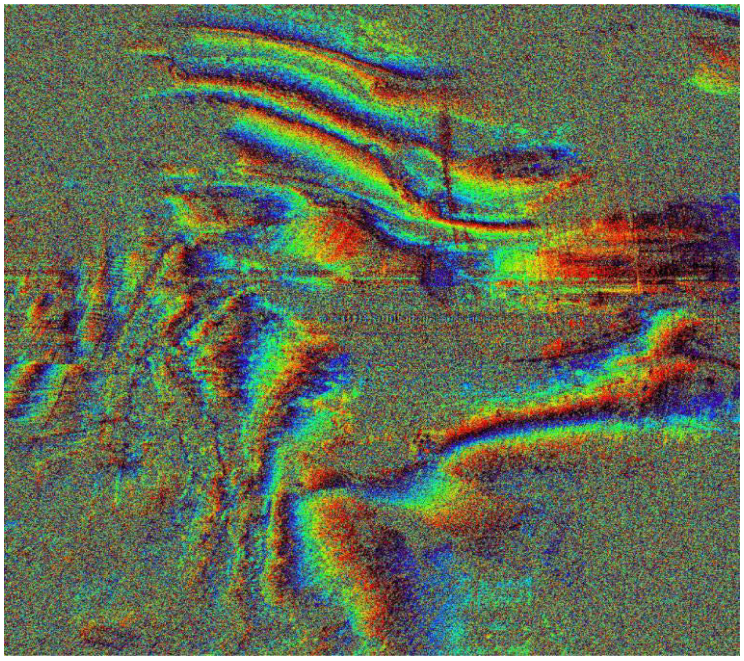

Figure 56: Interferogram of the Scene (Dreis-Tiefenbach) – Using Time Domain Processing Approach

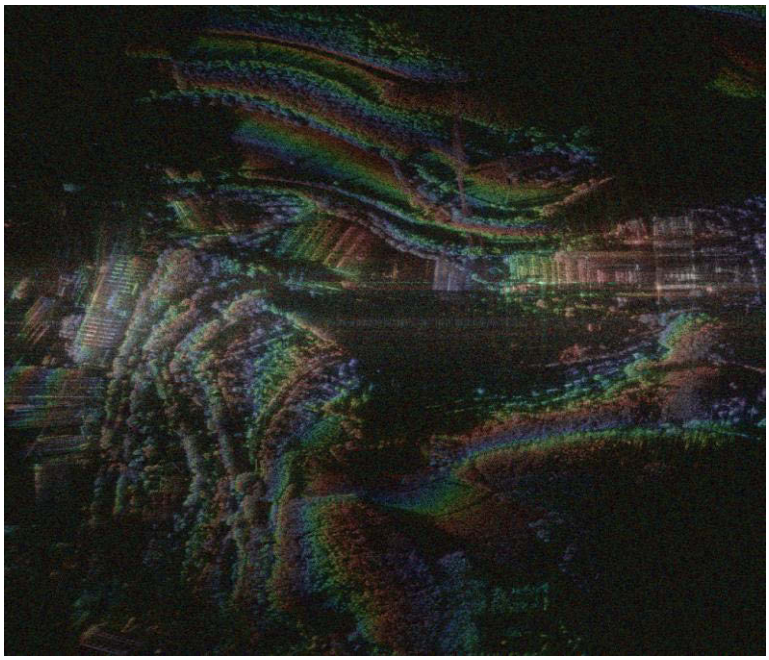

Figure 57: Interferometric Phase Overlaid on the Radar Intensity Image (Dreis-Tiefenbach)

We consider a small cutout of the above scene to generate a differential interferogram. It is generated by considering the phase difference between the two interferograms shown in Figure 55 and Figure 56. The interferogram in Figure 55 is generated from the interferometric data processed in the frequency domain and the interferogram in Figure 56 is generated by processing the same interferometric data in the time domain. The differential interferogram is shown in Figure 58.

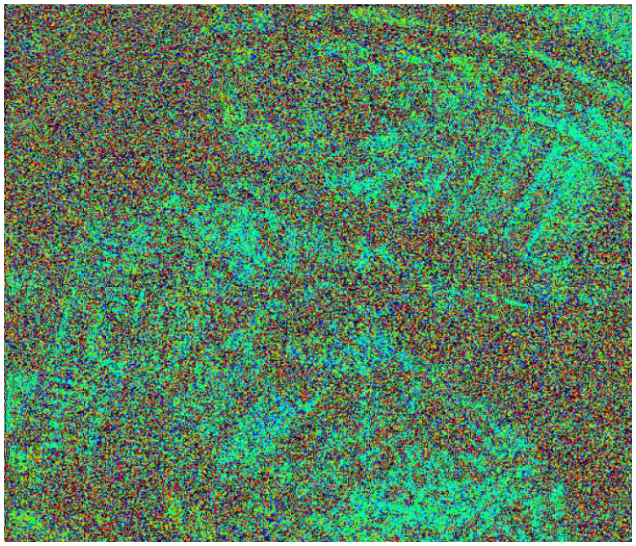

Figure 58: Differential Interferogram

Here, we observe coherence between the results processed in the time and frequency domain. We also observe a constant phase difference over the whole cut out and is not

varying along range and azimuth. The histogram of the differential interferometric phase of Figure 58 is shown in Figure 59.

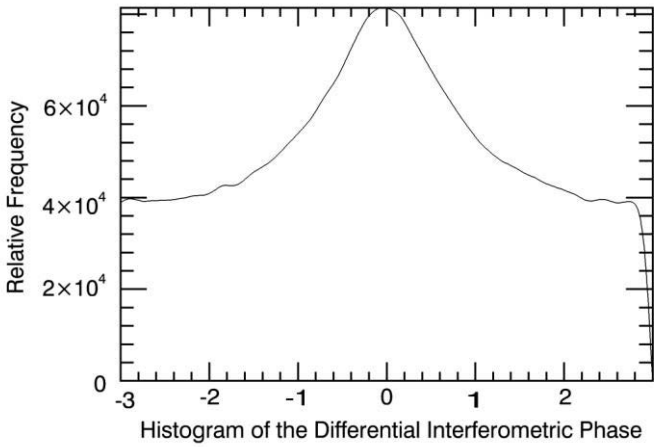

Figure 59: Histogram of the Differential Interferogram

The histogram of the differential interferometric phase is plotted against its relative frequencies. The mean and standard deviation of the distribution are 0.001 and 1.63 respectively. The minimum and maximum values of the phase lies between $-\pi$ to $+\pi$.

5.7 Conclusions

In this chapter, we have considered a special case of an AVCs, called stationary receiver configurations. Some experiments are conducted at the University of Siegen to obtain high resolution bistatic SAR data using a stationary receiver and TerraSAR-X satellite as transmitter. The raw data obtained during these experiments are processed using our proposed frequency domain algorithm and comparison with back projection algorithm is provided. First, we have considered the geometry of stationary receiver configurations and a signal model has been provided. In stationary receiver configurations, only the moving transmitter contributes towards the azimuth modulation. As the receiver is stationary, it introduces a range shift to the range migration trajectories of all targets located at the same range. A BPTRS is derived using the method of stationary phase and a frequency domain focusing algorithm is implemented to focus the data of stationary receiver experiments and to generate frequency domain interferometric images. A detailed comparison of some parts of the scene shows that our frequency domain focusing algorithm works well for stationary receiver configurations.

6 Summary and Conclusions

Bistatic SAR is a very effective tool to exploit various data acquisition geometries for analysis and processing. In this thesis, we have derived a frequency domain processing algorithm, for different bistatic SAR configurations. A bistatic point target reference spectrum is derived for a general bistatic SAR configuration based on Loffeld's bistatic formula and using the method of stationary phase. We assume different azimuth contributions of transmitter and receiver in the bistatic phase. The transmitter and receiver phases are expanded using the second order Taylor's expansion around their individual points of stationary phases. The bistatic point target reference spectrum depends on weighted azimuth contributions of transmitter and receiver phases. This weighting is derived by minimizing the square difference between common and individual points of stationary phases of the transmitter or receiver. The simulation results show good focusing of point targets for different bistatic SAR configurations.

The validity constraints for the transmitter and receiver are derived based on BPTRS. They express the validity of BPTRS for different bistatic SAR configurations. Their performance is analyzed for tandem, TI and hybrid configurations and the simulation results based on focusing of point targets are provided. Simulation results show that validity constraints are better fulfilled using different azimuth contributions of the transmitter and receiver phases in hybrid configurations. They are further analyzed to find an analytical expression for the weighting factor.

A frequency domain processing algorithm has been derived based on BPTRS using a scaled inverse Fourier transformation for focusing a complete scene. It is used to process azimuth variant and invariant configurations. An airborne experiment conducted at Fraunhofer-FHR in 2003, is considered for azimuth invariant configurations. As there are no considerable differences in the altitudes and velocities of the transmitter and receiver, therefore, equal azimuth weighting of the transmitter and receiver phases in BPTRS was applied. For azimuth variant configurations we have considered two hybrid experiments conducted by FHR using their airborne receiver system with TerraSAR-X satellite (transmitter). In hybrid bistatic SAR experiments, there is a large difference between the altitudes and velocities of the transmitter and receiver. Therefore, we have used different azimuth weighting of the transmitter and receiver phases in BPTRS. The focusing results of bistatic SAR experiments show that our frequency domain algorithm works well for the azimuth variant and invariant configurations. These results are also compared with those obtained using a time domain processing approach (back projection algorithm) and with optical images (Google maps).

In 2009, an X-band receiving system (HITCHHIKER) was developed at the University of Siegen to perform bistatic SAR spaceborne-stationary experiments. TerraSAR-X satellite is used with the stationary receiver system. Such bistatic stationary configurations can provide low cost, high resolution data. Different experiments have been conducted in different cities of Germany. In these configurations, only the moving platform contributes towards the azimuth modulation. The stationary receiver introduces a range shift in range to the range migration trajectories of point targets located at same range along azimuth. The BPTRS is modified for these configurations and based on it a frequency domain algorithm is implemented to process the data obtained during these experiments. A detailed comparison of some parts of the scene with back projection algorithm confirms that our frequency domain algorithm provides good quality images.

Appendix A: Detailed Derivation for Bistatic Point Target Reference Spectrum

The BPTRS has been derived in chapter 2, for unequal azimuth contributions of the transmitter and receiver phase terms. The mathematical expression is given in equation (2.19). It depends upon QM and BD phase terms. These phase terms depend upon first and second order phases of the transmitter and receiver, obtained at their individual and common PSPs. Their detailed expressions can be derived using the range histories of the transmitter and receiver.

A.1 Receiver Phase Terms

The receiver phase term is given in equation (2.9). It depends on range and azimuth frequencies and receiver's slant range. The first and second order derivatives of the receiver's phase terms are obtained using equation (2.9), as follows:

$$\dot{\phi}_R(\tau) = 2\pi\left\{\frac{(f+f_0)}{c_0}\dot{R}_R(\tau, R_{0R}, \tau_{0R}) + \frac{(2-\mu)}{2}f_\tau\right\} \tag{A.1}$$

$$\ddot{\phi}_R(\tau) = 2\pi\left\{\frac{(f+f_0)}{c_0}\ddot{R}_R(\tau, R_{0R}, \tau_{0R})\right\} \tag{A.2}$$

The receiver's phase and its derivatives depend upon receiver slant range and its derivatives. Taking inner product of slant range vector with itself, we can write:

$$R_R^2(\tau, R_{0R}, \tau_{0R}) = \vec{R}_R(\tau, R_{0R}, \tau_{0R}) \cdot \vec{R}_R(\tau, R_{0R}, \tau_{0R}) \tag{A.3}$$

Differentiating above expression and using the fact that derivative of the slant range vector is negative of the velocity vector of the receiver, we get following expression:

$$2R_R(\tau, R_{0R}, \tau_{0R})\dot{R}_R(\tau, R_{0R}, \tau_{0R}) = 2\dot{\vec{R}}_R(\tau, R_{0R}, \tau_{0R}) \cdot \vec{R}_R(\tau, R_{0R}, \tau_{0R}) \tag{A.4}$$

$$\dot{R}_R(\tau, R_{0R}, \tau_{0R}) = \frac{\dot{\vec{R}}_R(\tau, R_{0R}, \tau_{0R}).\vec{R}_R(\tau, R_{0R}, \tau_{0R})}{R_R(\tau, R_{0R}, \tau_{0R})}$$

$$= \frac{-\vec{v}_R.\vec{R}_R(\tau, R_{0R}, \tau_{0R})}{R_R(\tau, R_{0R}, \tau_{0R})}$$

The receiver slant range is given in equation (2.1), multiplying its both sides with the velocity vector $\vec{v}_R$ we get:

$$\vec{R}_R\left(\tau,R_{0R},\tau_{0R}\right)=\vec{R}_R\left(\tau_{0R},R_{0R},\tau_{0R}\right)-\vec{v}_R\left(\tau-\tau_{0R}\right) \tag{A.5}$$
$$\vec{v}_R\cdot\vec{R}_R\left(\tau,R_{0R},\tau_{0R}\right)=\vec{v}_R\cdot\vec{R}_R\left(\tau_{0R},R_{0R},\tau_{0R}\right)-\vec{v}_R\cdot\vec{v}_R\left(\tau-\tau_{0R}\right)$$
$$\vec{v}_R\cdot\vec{R}_R\left(\tau,R_{0R},\tau_{0R}\right)=-v_R^2\left(\tau-\tau_{0R}\right)$$

The velocity vector and receiver slant range at PCA are orthogonal to each other. Therefore, their dot product is zero i.e. $\vec{v}_R\cdot\vec{R}_R\left(\tau_{0R},R_{0R},\tau_{0R}\right)=0$. Substituting equation (A.5) into (A.4) we get:

$$\dot{R}_R\left(\tau,R_{0R},\tau_{0R}\right)=\frac{v_R^2\left(\tau-\tau_{0R}\right)}{R_R\left(\tau,R_{0R},\tau_{0R}\right)} \tag{A.6}$$

The second order derivative of the receiver's slant range is obtained by differentiating equation (A.3), we get:

$$2R_R\left(\tau,R_{0R},\tau_{0R}\right)\dot{R}_R\left(\tau,R_{0R},\tau_{0R}\right)=2\dot{\vec{R}}_R\left(\tau,R_{0R},\tau_{0R}\right)\cdot\vec{R}_R\left(\tau,R_{0R},\tau_{0R}\right) \tag{A.7}$$
$$\dot{R}_R^2\left(\tau,R_{0R},\tau_{0R}\right)+R_R\left(\tau,R_{0R},\tau_{0R}\right)\ddot{R}_R\left(\tau,R_{0R},\tau_{0R}\right)=$$
$$\dddot{\vec{R}}_R\left(\tau,R_{0R},\tau_{0R}\right)\cdot\vec{R}_R\left(\tau,R_{0R},\tau_{0R}\right)+\ddot{\vec{R}}_R\left(\tau,R_{0R},\tau_{0R}\right)\cdot\dot{\vec{R}}_R\left(\tau,R_{0R},\tau_{0R}\right)$$
$$\ddot{R}_R\left(\tau,R_{0R},\tau_{0R}\right)=\frac{1}{R_R\left(\tau,R_{0R},\tau_{0R}\right)}\begin{bmatrix}\dddot{\vec{R}}_R\left(\tau,R_{0R},\tau_{0R}\right).\vec{R}_R\left(\tau,R_{0R},\tau_{0R}\right)+\\ \ddot{\vec{R}}_R\left(\tau,R_{0R},\tau_{0R}\right)\cdot\dot{\vec{R}}_R\left(\tau,R_{0R},\tau_{0R}\right)\\ -\dot{R}_R^2\left(\tau,R_{0R},\tau_{0R}\right)\end{bmatrix}$$

Using equation (A.6) and assuming that the velocity vector is constant and its derivative is zero $\dddot{\vec{R}}_R\left(\tau,R_{0R},\tau_{0R}\right)=\ddot{\vec{v}}_R=0$, we simplify the above equation as follows:

$$\ddot{R}_R\left(\tau,R_{0R},\tau_{0R}\right)=\frac{v_R^2}{R_R\left(\tau,R_{0R},\tau_{0R}\right)}-\frac{v_R^4\left(\tau-\tau_{0R}\right)^2}{R_R^3\left(\tau,R_{0R},\tau_{0R}\right)} \tag{A.8}$$

Using equations (2.12) and (2.9), receiver phase at PSP is written as:

$$2\pi\left\{\frac{\left(f+f_0\right)}{c_0}\dot{R}_R\left(\tilde{\tau}_R,R_{0R},\tau_{0R}\right)+\frac{(2-\mu)}{2}f_\tau\right\}=0 \tag{A.9}$$

The above equation can be simplified using equation (A.6), as follows:

$$\frac{\left(f+f_0\right)}{c_0}\frac{v_R^2\left(\tilde{\tau}_R-\tau_{0R}\right)}{R_R\left(\tilde{\tau}_R,R_{0R},\tau_{0R}\right)}+\frac{(2-\mu)}{2}f_\tau=0 \tag{A.10}$$
$$v_R^2\left(\tilde{\tau}_R-\tau_{0R}\right)=-\frac{(2-\mu)}{2}\frac{f_\tau c_0}{\left(f+f_0\right)}R_R\left(\tilde{\tau}_R,R_{0R},\tau_{0R}\right)$$

After squaring the above equation, we can write:

$$v_R^4\left(\tilde{\tau}_R-\tau_{0R}\right)^2=-\frac{(2-\mu)^2}{4}\frac{f_\tau^2c_0^2}{\left(f+f_0\right)^2}R_R^2\left(\tilde{\tau}_R,R_{0R},\tau_{0R}\right) \tag{A.11}$$

The receiver's slant range as given in equation (2.1) is evaluated at receiver's PSP and is given as:

$$v_R^2\left(\tilde{\tau}_R-\tau_{0R}\right)^2=R_R^2\left(\tilde{\tau}_R,R_{0R},\tau_{0R}\right)-R_{0R}^2 \tag{A.12}$$

Combining equations (A.11) and (A.12) and using equation (2.22) we get:

$$R_R\left(\tilde{\tau}_R,R_{0R},\tau_{0R}\right)=\frac{R_{0R}\left|f+f_0\right|}{F_R^{1/2}\left(f,f_\tau\right)} \tag{A.13}$$

Substituting equation (A.13) into (A.10), we get:

$$\tilde{\tau}_R=\tau_{0R}-\frac{(2-\mu)}{2}\frac{\left|f+f_0\right|}{\left(f+f_0\right)}\frac{f_\tau c_0R_{0R}}{v_R^2F_R^{1/2}\left(f,f_\tau\right)} \tag{A.14}$$

$$\tilde{\tau}_R=\tau_{0R}-\frac{(2-\mu)f_\tau c_0}{2v_R^2}\frac{R_{0R}\,\mathrm{sgn}\left(f+f_0\right)}{F_R^{1/2}\left(f,f_\tau\right)}$$

The second order derivative of the receiver slant range is given in equation (A.8), using equation (A.6) and evaluating it at PSP of receiver we get:

$$\ddot{R}_R\left(\tilde{\tau}_R,R_{0R},\tau_{0R}\right)=\frac{v_R^2-\dot{R}_R^2\left(\tilde{\tau}_R,R_{0R},\tau_{0R}\right)}{R_R\left(\tilde{\tau}_R,R_{0R},\tau_{0R}\right)} \tag{A.15}$$

Evaluating equations (A.6) at PSP of receiver and using equation (A.10), we get:

$$\dot{R}_R\left(\tilde{\tau}_R,R_{0R},\tau_{0R}\right)=-\frac{(2-\mu)}{2}\frac{f_\tau c_0}{\left(f+f_0\right)} \tag{A.16}$$

Substituting equation (A.13) and (A.16) into (A.15), after simplification we get:

$$\begin{aligned}\ddot{R}_R\left(\tilde{\tau}_R,R_{0R},\tau_{0R}\right)&=\frac{F_R^{1/2}\left(f,f_\tau\right)}{R_{0R}\left|f+f_0\right|}\frac{v_R^2}{\left(f+f_0\right)^2}\left[\left(f+f_0\right)^2-\frac{(2-\mu)^2f_\tau^2c_0^2}{4v_R^2}\right]\\&=\frac{v_R^2}{\left(f+f_0\right)^2}\frac{F_R^{3/2}\left(f,f_\tau\right)}{R_{0R}\left|f+f_0\right|}\end{aligned} \tag{A.17}$$

Using equations (A.2) and (A.17), the receiver's second order phase term evaluated at its PSP is written as follows:

$$\ddot{\phi}_R\left(\tilde{\tau}_R\right)=\frac{2\pi v_R^2}{c_0R_{0R}}\frac{\mathrm{sgn}\left(f+f_0\right)}{\left(f+f_0\right)^2}F_R^{3/2}\left(f,f_\tau\right) \tag{A.18}$$

Similarly, the receiver phase term at PSP can be written using equations (2.9), (A.13) and (A.14).

$$\phi_R\left(\tilde{\tau}_R\right) = 2\pi\left\{\begin{array}{l}\dfrac{\left(f+f_0\right)}{c_0}\dfrac{R_{0R}\left|f+f_0\right|}{F_R^{1/2}\left(f,f_\tau\right)}+\dfrac{(2-\mu)f_\tau}{2}\\ \left[\tau_{0R}-\dfrac{(2-\mu)}{2}\dfrac{f_\tau c_0 R_{0R}}{v_R^2}\dfrac{\operatorname{sgn}\left(f+f_0\right)}{F_R^{1/2}\left(f,f_\tau\right)}\right]\end{array}\right\} \tag{A.19}$$

$$= 2\pi\left\{\frac{(2-\mu)}{2}f_\tau\tau_{0R}+\frac{R_{0R}\operatorname{sgn}\left(f+f_0\right)}{c_0F_R^{1/2}\left(f,f_\tau\right)}\left[\left(f+f_0\right)^2-\frac{(2-\mu)^2}{4}\frac{f_\tau^2c_0^2}{v_R^2}\right]\right\}$$

$$= \pi(2-\mu)f_\tau\tau_{0R}+\frac{2\pi}{c_0}\operatorname{sgn}\left(f+f_0\right)R_{0R}F_R^{1/2}\left(f,f_\tau\right)$$

Equations (A.13), (A.16) and (A.17) give the receiver's slant range and its derivatives and equations (A.18) and (A.19) give the receiver's phase and its derivatives at PSP.

A.2 Transmitter Phase Terms

The transmitter's phase terms can be obtained in a similar way as the receiver's phase terms. The first and second order derivatives of the transmitter's phase terms are obtained using equation (2.9), as follows:

$$\dot{\phi}_T\left(\tau\right) = 2\pi\left\{\frac{\left(f+f_0\right)}{c_0}\dot{R}_T\left(\tau,R_{0R},\tau_{0R}\right)+\frac{\mu}{2}f_\tau\right\} \tag{A.20}$$

$$\ddot{\phi}_T\left(\tau\right) = 2\pi\left\{\frac{\left(f+f_0\right)}{c_0}\ddot{R}_T\left(\tau,R_{0R},\tau_{0R}\right)\right\} \tag{A.21}$$

The relationship between slant range vectors of the transmitter and receiver can be obtained from geometry. From Figure 60, we can write the following relationship:

$$\vec{R}_T\left(\tau,R_{0R},\tau_{0R}\right) = \vec{R}_R\left(\tau_{0R},R_{0R},\tau_{0R}\right)-\vec{v}_T\left(\tau-\tau_{0R}\right)+\vec{d}\left(\tau_{0R}\right) \tag{A.22}$$

Where, vector $\vec{d}\left(\tau_{0R}\right)$ represents distance between the transmitter and receiver at receiver's PCA.

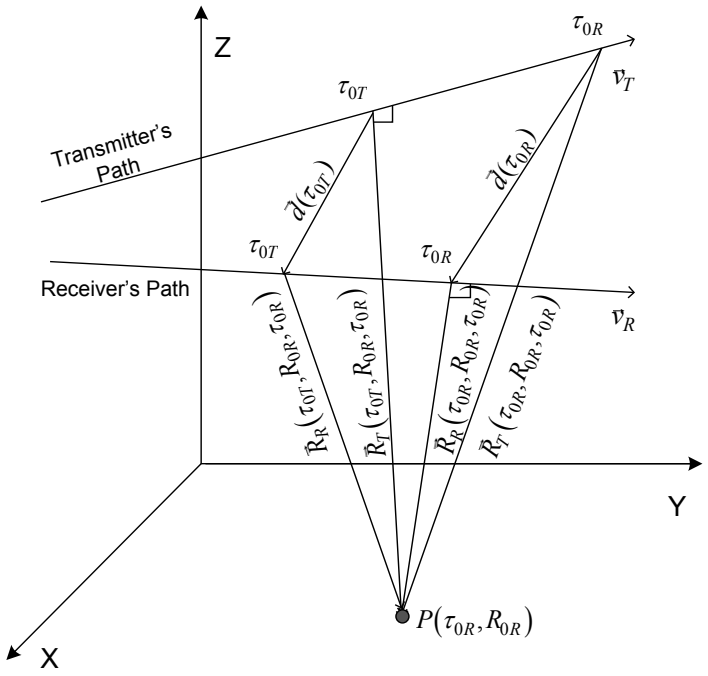

Figure 60: Bistatic Vectorial Geometry

Relationship between the receiver's slant ranges is given in equation (A.4), similarly we can write for the transmitter as:

$$R_T\left(\tau, R_{0R}, \tau_{0R}\right)\dot{R}_T\left(\tau, R_{0R}, \tau_{0R}\right) = -\vec{v}_T.\vec{R}_T\left(\tau, R_{0R}, \tau_{0R}\right) \tag{A.23}$$

Differentiating the above equation, we get second order derivative of the transmitter's slant range.

$$\dot{R}_T^2\left(\tau, R_{0R}, \tau_{0R}\right) + \ddot{R}_T\left(\tau, R_{0R}, \tau_{0R}\right)R_T\left(\tau, R_{0R}, \tau_{0R}\right) = -\vec{v}_T \cdot \dot{\vec{R}}_T\left(\tau, R_{0R}, \tau_{0R}\right) \tag{A.24}$$

$$\ddot{R}_T\left(\tau, R_{0R}, \tau_{0R}\right) = \frac{v_T^2 - \dot{R}_T^2\left(\tau, R_{0R}, \tau_{0R}\right)}{R_T(\tau, R_{0R}, \tau_{0R})}$$

Using equations (2.12) and (2.9), the transmitter phase term at PSP is written as:

$$2\pi\left\{\frac{\left(f + f_0\right)}{c_0}\dot{R}_T\left(\tilde{\tau}_T, R_{0R}, \tau_{0R}\right) + \frac{\mu}{2}f_\tau\right\} = 0 \tag{A.25}$$

The above equation is simplified for first order derivative of the transmitter's slant range at PSP.

$$\dot{R}_T\left(\tilde{\tau}_T, R_{0R}, \tau_{0R}\right) = -\frac{\mu f_\tau c_0}{2\left(f + f_0\right)} \tag{A.26}$$

Equation (A.24) can be simplified using equation (A.26), as follows:

$$\ddot{R}_T\left(\tilde{\tau}_T, R_{0R}, \tau_{0R}\right) = \frac{1}{R_T(\tilde{\tau}_T, R_{0R}, \tau_{0R})}\left[v_T^2 - \frac{\mu^2 f_\tau^2 c_0^2}{4\left(f + f_0\right)^2} \right] \tag{A.27}$$

Substituting equation (A.22) into (A.23), we get:

$$\dot{R}_T\left(\tau, R_{0R}, \tau_{0R}\right) = \frac{v_T^2\left(\tau - \tau_{0R}\right) - \vec{v}_T\left[\vec{R}_R\left(\tau_{0R}, R_{0R}, \tau_{0R}\right) + \vec{d}\left(\tau_{0R}\right)\right]}{R_T\left(\tau, R_{0R}, \tau_{0R}\right)} \tag{A.28}$$

Evaluating the above equation at the transmitter's PSP and using equation (A.26), we get:

$$\frac{v_T^2\left(\tilde{\tau}_T - \tau_{0R}\right) - \vec{v}_T\left[\vec{R}_R\left(\tau_{0R}, R_{0R}, \tau_{0R}\right) + \vec{d}\left(\tau_{0R}\right)\right]}{R_T\left(\tilde{\tau}_T, R_{0R}, \tau_{0R}\right)} = -\frac{\mu f_\tau c_0}{2\left(f + f_0\right)} \tag{A.29}$$

Simplifying the above equation we get:

$$\tilde{\tau}_T - \tau_{0R} = -\frac{\mu f_\tau c_0 R_T\left(\tilde{\tau}_T, R_{0R}, \tau_{0R}\right)}{2v_T^2\left(f + f_0\right)} + \frac{\vec{v}_T}{v_T^2}\left[\vec{R}_R\left(\tau_{0R}, R_{0R}, \tau_{0R}\right) + \vec{d}\left(\tau_{0R}\right)\right] \tag{A.30}$$

Evaluating equation (A.22) at the transmitter PCA τ_{0T} and multiplying both sides with $\vec{v}_T$, we get:

$$\begin{aligned} 0 &= \vec{v}_T\left[\vec{R}_R\left(\tau_{0R}, R_{0R}, \tau_{0R}\right) + \vec{d}\left(\tau_{0R}\right)\right] - v_T^2\left(\tau_{0T} - \tau_{0R}\right) \\ \left(\tau_{0T} - \tau_{0R}\right) &= \frac{\vec{v}_T}{v_T^2}\left[\vec{R}_R\left(\tau_{0R}, R_{0R}, \tau_{0R}\right) + \vec{d}\left(\tau_{0R}\right)\right] \end{aligned} \tag{A.31}$$

Using equations (2.25) and (A.31), we can simplify equation (A.30) as follows:

$$\tilde{\tau}_T - \tau_{0R} = -\frac{\mu f_\tau c_0}{2v_T^2\left(f + f_0\right)} R_T\left(\tilde{\tau}_T, R_{0R}, \tau_{0R}\right) + a_0 \tag{A.32}$$

Evaluating equation (A.22) at the transmitter's PSP, we get:

$$\vec{R}_T\left(\tilde{\tau}_T, R_{0R}, \tau_{0R}\right) = \vec{R}_R\left(\tau_{0R}, R_{0R}, \tau_{0R}\right) - \vec{v}_T\left(\tilde{\tau}_T - \tau_{0R}\right) + \vec{d}\left(\tau_{0R}\right) \tag{A.33}$$

Substituting equation (A.32) into (A.33) we get:

$$\vec{R}_T\left(\tilde{\tau}_T, R_{0R}, \tau_{0R}\right) = \vec{R}_R\left(\tau_{0R}, R_{0R}, \tau_{0R}\right) - \vec{v}_T\begin{pmatrix} a_0 - \dfrac{\mu f_\tau c_0}{2v_T^2\left(f + f_0\right)} \\ R_T\left(\tilde{\tau}_T, R_{0R}, \tau_{0R}\right) \end{pmatrix} + \vec{d}\left(\tau_{0R}\right) \tag{A.34}$$

Squaring above equation and using equation (2.25) and (A.31), we get:

$$R_T^2\left(\tilde{\tau}_T, R_{0R}, \tau_{0R}\right) = \left[\vec{R}_R\left(\tau_{0R}, R_{0R}, \tau_{0R}\right) + \vec{d}\left(\tau_{0R}\right)\right]^2 + v_T^2 \begin{pmatrix} a_0 - \dfrac{\mu f_\tau c_0}{2v_T^2\left(f + f_0\right)} \\ R_T\left(\tilde{\tau}_T, R_{0R}, \tau_{0R}\right) \end{pmatrix}^2 \quad \text{(A.35)}$$

$$-2\vec{v}_T\left[\vec{R}_R\left(\tau_{0R}, R_{0R}, \tau_{0R}\right) + \vec{d}\left(\tau_{0R}\right)\right] \begin{pmatrix} a_0 - \dfrac{\mu f_\tau c_0}{2v_T^2\left(f + f_0\right)} \\ R_T\left(\tilde{\tau}_T, R_{0R}, \tau_{0R}\right) \end{pmatrix}$$

$$= \left[\vec{R}_R\left(\tau_{0R}, R_{0R}, \tau_{0R}\right) + \vec{d}\left(\tau_{0R}\right)\right]^2 - a_0^2 v_T^2$$

$$+ \frac{\mu^2 f_\tau^2 c_0^2}{4v_T^2\left(f + f_0\right)^2} R_T^2\left(\tilde{\tau}_T, R_{0R}, \tau_{0R}\right)$$

Simplifying the above equation we get:

$$R_T\left(\tilde{\tau}_T, R_{0R}, \tau_{0R}\right) = \frac{\sqrt{\left[\vec{R}_R\left(\tau_{0R}, R_{0R}, \tau_{0R}\right) + \vec{d}\left(\tau_{0R}\right)\right]^2 - a_0^2 v_T^2}}{\sqrt{1 - \dfrac{\mu^2 f_\tau^2 c_0^2}{4v_T^2\left(f + f_0\right)^2}}} \quad \text{(A.36)}$$

$$= \frac{\sqrt{\left[\vec{R}_R\left(\tau_{0R}, R_{0R}, \tau_{0R}\right) + \vec{d}\left(\tau_{0R}\right)\right]^2 - a_0^2 v_T^2}}{F_T^{1/2}\left(f, f_\tau\right)} \left|f + f_0\right|$$

From equations (2.25) and (A.22) we know:

$$a_2 = \frac{R_{0T}}{R_{0R}} = \frac{\left|\vec{R}_T\left(\tau_{0T}, R_{0R}, \tau_{0R}\right)\right|^2}{\left|\vec{R}_R\left(\tau_{0R}, R_{0R}, \tau_{0R}\right)\right|^2} \quad \text{(A.37)}$$

$$= \frac{\left|\vec{R}_R\left(\tau_{0R}, R_{0R}, \tau_{0R}\right) - \vec{v}_T\left(\tau_{0T} - \tau_{0R}\right) + \vec{d}\left(\tau_{0R}\right)\right|^2}{\left|\vec{R}_R\left(\tau_{0R}, R_{0R}, \tau_{0R}\right)\right|^2}$$

$$= \left|\frac{\vec{R}_R\left(\tau_{0R}, R_{0R}, \tau_{0R}\right) + \vec{d}\left(\tau_{0R}\right)}{\vec{R}_R\left(\tau_{0R}, R_{0R}, \tau_{0R}\right)}\right|^2 - \frac{v_T^2 a_0^2}{R_{0R}^2}$$

Using (A.37), we can simplify (A.36) as:

$$R_T\left(\tilde{\tau}_T, R_{0R}, \tau_{0R}\right) = \frac{R_{0R} a_2}{F_T^{1/2}\left(f, f_\tau\right)} \left|f + f_0\right| \quad \text{(A.38)}$$

Substituting equation (A.38) into (A.32), we get:

$$\tilde{\tau}_T = \tau_{0T} - \frac{\mu f_\tau c_0}{2v_T^2} \frac{R_{0T}\,\mathrm{sgn}\left(f + f_0\right)}{F_T^{1/2}\left(f, f_\tau\right)} \quad \text{(A.39)}$$

Similarly, substituting equation (A.38) into (A.27), we get the second order derivative of the transmitter slant range at its stationary point.

$$\ddot{R}_T\left(\tilde{\tau}_T, R_{0R}, \tau_{0R}\right) = \frac{v_T^2}{\left(f+f_0\right)^2} \frac{F_T^{3/2}\left(f, f_\tau\right)}{R_{0T}\left|f+f_0\right|} \tag{A.40}$$

In equation (2.20), the difference between PSPs of the transmitter and receiver can be obtained using equations (A.39) and (A.14) as follows:

$$\tilde{\tau}_T - \tilde{\tau}_R = a_0 - \frac{f_\tau c_0 R_{0R}\,\mathrm{sgn}\left(f+f_0\right)}{2v_T^2 v_R^2}\left(\frac{\mu a_2 v_R^2}{F_T^{1/2}\left(f, f_\tau\right)} + \frac{(2-\mu)v_T^2}{F_R^{1/2}\left(f, f_\tau\right)}\right) \tag{A.41}$$

The transmitter's phase at PSP can be obtained by substituting equations (A.38) and (A.39) into (2.9), we get:

$$\begin{aligned}\phi_T\left(\tilde{\tau}_T\right) &= 2\pi\left\{\begin{array}{l}\dfrac{R_{0T}\left(f+f_0\right)^2}{c_0}\dfrac{\mathrm{sgn}(f+f_0)}{F_T^{1/2}\left(f, f_\tau\right)} + \dfrac{\mu}{2}\tau_{0T} f_\tau - \\ \dfrac{\mu^2 f_\tau^2 c_0 R_{0T}}{4v_T^2}\dfrac{\mathrm{sgn}\left(f+f_0\right)}{F_T^{1/2}\left(f, f_\tau\right)}\end{array}\right\} \\ &= \pi\mu\tau_{0T} f_\tau + 2\pi\frac{R_{0T}\,\mathrm{sgn}(f+f_0)}{c_0} F_T^{1/2}\left(f, f_\tau\right)\end{aligned} \tag{A.42}$$

The second order transmitter phase term at PSP can be obtained using equations (A.21), (A.27) and (A.38).

$$\ddot{\phi}_T\left(\tilde{\tau}_T\right) = \frac{2\pi v_T^2}{c_0 R_{0T}}\frac{\mathrm{sgn}\left(f+f_0\right)}{\left(f+f_0\right)^2} F_T^{3/2}\left(f, f_\tau\right) \tag{A.43}$$

Equations (A.27), (A.28) and (A.38) give the transmitter's slant range and its derivatives and equations (A.42) and (A.43) give the transmitter's phase and its derivatives at PSP.

Appendix B: Quality Measuring Parameters

In this section, we discuss some parameters, which provide information about the quality of SAR images. We consider the impulse response function of a single point target and discuss its quality parameters in terms of Impulse Response Width (IRW) in range and azimuth, Peak Side Lobe Ratio (PSLR) and Integrated Side Lobe Ratio (ISLR).

B.1 Impulse Response Width

It gives information about resolution of a point target in range and azimuth. Resolution is a measure of the main lobe width of the impulse response of a point target at -3 dB level. Impulse response is a 2D function which depends on reflected characteristics (brightness) of a point target. The main lobe width of sinc pulse at -3 dB in range (or azimuth) is 0.886 of the inverse of range (or azimuth) bandwidth and is given as [75]:

$$IRW_{ra} = 0.886\frac{c_0}{2B_{ra}} \quad ; \quad IRW_{az} = 0.886\frac{v}{B_{az}} \tag{B.1}$$

Here, c_0 is the velocity of light and v is the platform velocity. B_{ra} and B_{az} are range and azimuth bandwidth respectively.

B.2 Integrated Side Lobe Ratio

The focused result of a point target is represented as impulse response function. It has a main lobe with high peak at the location of point target and also has surrounding side lobes with smaller peaks. Integrated side lobe ratio is a measure of the energy integrated over side lobes to the energy in the main lobe.

$$ISLR = \frac{\int_{-\infty}^{-l/2} |h(x)|^2 dx + \int_{l/2}^{\infty} |h(x)|^2 dx}{\int_{-l/2}^{l/2} |h(x)|^2 dx} \tag{B.2}$$

Here, $h(x)$ is the amplitude of impulse response of a point target and l is the width of the main lobe between its left and right first zero crossing. The lower the ISLR of impulse response function, the lower will be the spreading of the side lobe energy of stronger targets and lower will be the masking of weaker targets. Its value is about -10 dB for sinc pulse and can drop to -20 dB using Hamming filter.

B.3 Peak Side Lobe Ratio

The peak side lobe ratio of impulse response of a point target is the ratio between the peak of the main lobe and that of the first side lobe. The PSLR for a sinc pulse is around -13 dB. A high PSLR means stronger returns from side lobes of the target which either results in the detection of false targets or masking of weaker targets. They can be reduced at cost of geometrical resolution.

The quality parameters are calculated for the point targets for different bistatic SAR configurations and are given in chapter 3.

Appendix C: Scaled Inverse Fourier Transformation

We have used a SIFT in focusing of complete scene for a general bistatic SAR configuration. It is a mathematical tool used to transform a scaled spectrum into non-scaled counter parts in time domain.

Now, we consider a scaled spectrum and its Fourier transformations as:

$$H(f) = U(af) \tag{C.1}$$

$$h(t) = \int_{-\infty}^{\infty} U(af) e^{j2\pi ft} df$$

We change integration variable as $\tilde{f} = af$, and substitute in above equation and get:

$$h(t) = \frac{1}{|a|} \int_{-\infty}^{\infty} U(\tilde{f}) e^{j2\pi \tilde{f} \frac{t}{a}} d\tilde{f} \tag{C.2}$$

$$= \frac{1}{|a|} u\left(\frac{t}{a}\right)$$

Here we can see that the corresponding signal of a scaled spectrum is scaled inverse in the time domain. In SAR processing we want to compensate the scaled spectrum to get non-scaled signal in the time domain. We consider equation (C.1) and multiply scaled spectrum with $e^{j2\pi aft}$ instead of $e^{j2\pi ft}$, we get:

$$\tilde{h}(t) = \int_{-\infty}^{\infty} U(af) e^{j2\pi aft} df \tag{C.3}$$

We change the integration variable $\tilde{f} = af$ as:

$$\tilde{h}(t) = \frac{1}{|a|} \int_{-\infty}^{\infty} U(\tilde{f}) e^{j2\pi \tilde{f} t} d\tilde{f} \tag{C.4}$$

$$= \frac{1}{|a|} u(t)$$

In the above result the problem of a scaled inverse signal in the time domain is solved, we get:

$$u(t) = |a| \int_{-\infty}^{\infty} U(af) e^{j2\pi aft} df \tag{C.5}$$

Above integral is similar to Fourier integral of $u(t)$ but with a scaling coefficient in phase. It can be rewritten as:

$$u(t) = |a| e^{j\pi a t^2} \int_{-\infty}^{\infty} U(af) e^{j\pi a f^2} e^{-j\pi a (t-f)^2} df \tag{C.6}$$

Above integral can be written as convolution of two signals:

$$u(t) = |a| e^{j\pi a t^2} \left[U(af) e^{j\pi a f^2} * e^{-j\pi a f^2} \right] \tag{C.7}$$

Above equation gives a very interesting result, it shows that a non-scaled signal $u(t)$ can be obtained by multiplying the scaled spectrum $U(af)$ with a chirp $e^{j\pi a f^2}$ in the frequency domain, then convolving the result with chirp $e^{-j\pi a f^2}$ in the frequency domain, the result is then multiplied with chirp $e^{j\pi a t^2}$ in the time domain. This transformation is called SIFT [66] and mathematical steps are shown in Figure 61.

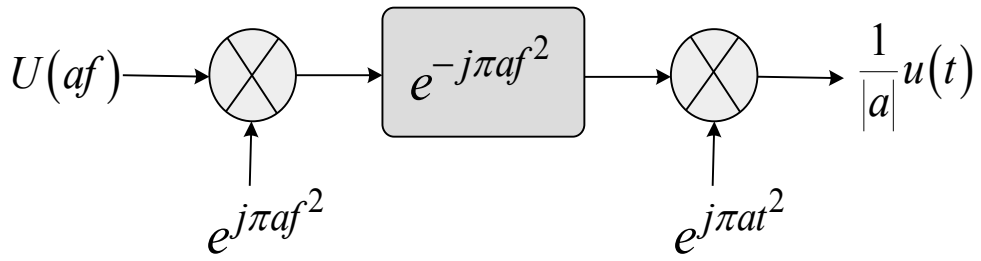

Figure 61: Scaled Inverse Fourier Transformation

References

[1] O. Loffeld, H. Nies, V. Peters and S. Knedlik. Models and Useful Relations for Bistatic SAR Processing. *IEEE Transactions on Geosciences and Remote Sensing*, Vol. 42, No. 10, October 2004.

[2] O. Loffeld, H. Nies, U. Gebhardt, V. Peters and S. Knedlik. Bistatic SAR - Some Reflections on Rocca's Smile. *In EUSAR 2004, European Conference on Synthetic Aperture Radar,* Ulm, Germany, May 2004.

[3] O. Loffeld and A. Hein. SAR Processing by Inverse Scaled Fourier Transformation. *In EUSAR 1996*, Königswinter, Germany, 1996.

[4] O. Loffeld, F. Schneider and A. Hein. Focusing SAR Images by Inverse Scaled Fourier Transformation. *In International Conference on Signal Processing and Communication*, Las Palmas, Gran Canaria, 1998.

[5] O. Loffeld, K. Natroshvili, H. Nies, U. Gebhardt, S. Knedlik, A. Medrano Ortiz and A. Amankwah. 2D-Scaled Inverse Fourier Transformation for Bistatic SAR. *In EUSAR 2006,* Dresden, Germany, 2006.

[6] K. Natroshvili, O. Loffeld, H. Nies and A. Medrano Ortiz. First Steps to Bistatic SAR Focusing. *In IGARSS 2005, International Geosciences and Remote Sensing Symposium,* Seoul, Korea, 2005.

[7] K. Natroshvili, O. Loffeld and H. Nies. Focusing of Arbitrary Bistatic SAR Configurations. *In EUSAR 2006,* Dresden, Germany, 2006.

[8] K. Natroshvili, O. Loffeld, H. Nies, A. Medrano Ortiz and S. Knedlik. Focusing of General Bistatic SAR Configuration Data with 2D Inverse Scaled FFT. *IEEE Transactions in Geosciences and Remote Sensing,* Vol. 44, No. 10, Oct 2006.

[9] H. Nies, O. Loffeld, K. Natroshvili, I. Walterscheid and A. R. Brenner. Parameter Estimation for Bistatic Constellations. *In IGARSS 2005,* Seoul, Korea, 2005.

[10] H. Nies, O. Loffeld and K. Natroshvili. Analysis and Focusing of Bistatic Airborne SAR Data. *In EUSAR 2006,* Dresden, Germany, 2006.

[11] H. Nies, F. Behner, S. Reuter, O. Loffeld and R. Wang. SAR Experiments in a Bistatic Hybrid Configuration for Generating PollnSAR Data with TerraSAR-X Illumination. *In EUSAR 2010,* Aachen, Germany, June 2010.

[12] H. Nies, F. Behner, S. Reuter, O. Loffeld and R. Wang. Polarimetric and Interferometric Applications in a Bistatic Hybrid SAR Mode using TerraSAR-X. *In IGARSS 2010*, Hawaii, USA, July 2010.

[13] U. Gebhardt, O. Loffeld, H. Nies, K. Natroshvili and J. Ender. Bistatic Airborne/ Spaceborne Hybrid Experiment: Simulation and Analysis. *In EUSAR 2006*, Dresden, Germany, 2006.

[14] D. D'Aria, A. Monti Guarnieri and F. Rocca. Focusing Bistatic Synthetic Aperture Radar using Dip Move Out. *IEEE Transactions on Geosciences and Remote Sensing,* Vol. 42, pp.1362-1376, July 2004.

[15] D. D'Aria, A. Monti Guarnieri and F. Rocca. Precision Bistatic Processing with a Standard SAR Processor. *In EUSAR 2004,* Ulm, Germany, May 2004.

[16] C. Cafforio, C. Prati and F. Rocca. SAR Data Focusing using Seismic Migration Techniques. *IEEE Transactions on Aerospace and Electronic Systems,* Vol. 27, no. 2, pp.194-206, March 1991.

[17] I. Walterscheid, J. H. Ender, A. Brenner and O. Loffeld. Bistatic SAR Processing and Experiments. *IEEE Transactions on Geosciences and Remote Sensing*, Vol. 44, No. 10, Oct 2006.

[18] I. Walterscheid, T. Espeter and J. H. Ender. Performance Analysis of a Hybrid Bistatic SAR System Operating in Double Sliding Spotlight Mode. *In IGARSS 2007*, Barcelona, Spain, July 2007.

[19] J. H. Ender, I. Walterscheid and A. Brenner. New Aspects of Bistatic SAR: Processing and Experiments. *In IGARSS 2004,* Anchorage, USA, Sept 2004.

[20] J. H. Ender. A Step to Bistatic SAR Processing. *In EUSAR 2004*, Ulm, Germany, May 2004.

[21] P. Dubois-Fernandez, H. Cantalloube, B. Vaizan, G. Krieger, R. Horn, M. Wendler, and V. Giroux. ONERA-DLR Bistatic SAR Campaign: Planning, Data Acquisition, and first Analysis of Bistatic Scattering Behavior of Natural and Urban Targets. *IEEE Proceedings Radar, Sonar and Navigation*, Vol. 153, No.3, 2006.

[22] G. Yates and A. M. Horne. Bistatic SAR Image Formation. *In EUSAR 2004*, Ulm, Germany, May 2004.

[23] J. H. Ender. Signal Theoretical Aspects of Bistatic SAR. *In IGARSS 2003*, Tolouse, France, July 2003.

[24] J. H. Ender, I. Walterscheid and A. Brenner. Bistatic SAR – Translational Invariant Processing and Experimental Results. *IEEE Proceedings Radar, Sonar and Navigation,* Vol. 153, No. 3, pp. 177-183, June 2006.

[25] I. Walterscheid, A. R. Brenner and J. H. Ender. Geometry and System Aspects for a Bistatic Airborne SAR-Experiment. *In EUSAR 2004,* Ulm, Germany, May 2004.

[26] I. Walterscheid, J. H. Ender, A. R. Brenner and O. Loffeld. Bistatic SAR Processing Using an Omega-k Type Algorithm. *In IGARSS 2005,* Seoul, Korea, 2005.

[27] I. Walterscheid, A. Brenner, J. H. Ender, and O. Loffeld. A Bistatic Airborne SAR Experiment and Processing Results. *In IRS, International Radar Symposium,* Berlin, Germany, 2005.

[28] I. Walterscheid, J. Klare, A. R. Brenner, J. H. Ender and O. Loffeld. Challenges of a Bistatic Spaceborne/Airborne SAR Experiment. *In EUSAR 2006,* Dresden, Germany, 2006.

[29] I. Walterscheid, T. Espeter, A. Brenner, J. Klare, J. H. Ender, H. Nies, R. Wang and O. Loffeld. Bistatic SAR Experiments with PAMIR and TerraSAR-X – Setup, Processing and Image Results. *IEEE Transactions on Geosciences and Remote Sensing,* Vol. 48, No. 8, Aug 2010.

[30] T. Espeter, I. Walterscheid, J. Klare and J. H. Ender. Synchronization Techniques for Bistatic Spaceborne/Airborne SAR Experiments with TerraSAR-X and PAMIR. *In IGARSS 2007*, Barcelona, Spain, July 2007.

[31] S. V. Baumgartner and M. Rodriguez-Cassola. Bistatic Experiment Using TerraSAR-X and DLR's new F-SAR System. *In EUSAR 2008*, Friedrichshafen, Germany, June 2008.

[32] D. Martinsek and R. Goldstein. Bistatic Radar Experiment. *In EUSAR*, Friedrichshafen, Germany, May 1998.

[33] A. Damini, M. McDonald and G. E. Haslam. X-band Wideband Experimental Airborne Radar for SAR, GMTI and Maritime Surveillance. *IEEE Proceedings Radar, Sonar and Navigation,* Vol. 150, No. 4, pp. 305-312, Aug 2003.

[34] R. Bamler and E. Boerner. On the Use of Numerically Computed Transfer Functions for Processing of Data from Bistatic SAR and High Squint Orbit SAR. *In IGARSS 2005*, Seoul, Korea, July 2005.

[35] R. Bamler. A Comparison of Range-Doppler and Wave number Domain SAR Focussing Algorithms. *IEEE Transactions on Geosciences and Remote Sensing*, Vol. 30, No. 4, July 1992.

[36] R. Bamler, F. Meyer and W. Liebhart. No Math: Bistatic SAR Processing using Numerically Computed Transfer Functions. *In IGARSS 2006*, Denver, USA, July 2006.

[37] A. Moreira, J. Mittermayer and R. Schreiber. Extended Chirp Scaling Algorithm for Air- and Spaceborne SAR Data Processing in Stripmap and ScanSAR Imaging Modes. *IEEE Transactions on Geosciences and Remote Sensing*, Vol. 34, No. 5, 1996.

[38] J. Mittermayer, A. Moriera and O. Loffeld. Spotlight SAR Data Processing Using the Frequency Scaling Algorithm. *IEEE Transactions on Geosciences and Remote Sensing,* Vol. 37, No. 5, Sept 1999.

[39] G. Krieger, H. Fiedler and A. Moriera. Bi- and Multistatic SAR: Potentials and Challenges. *In EUSAR 2004*, Ulm, Germany, May 2004.

[40] G. Krieger, A. Moriera, I. Hajnsek and D. Hounam. A Tandem TerraSAR-X Configuration for Single Pass SAR Interferometry. *In RADAR 2004*, Toulouse, France, Oct 2004.

[41] F. Wong and T. S. Yeo. New Applications of Nonlinear Chirp Scaling in SAR Data Processing. *IEEE Transactions of Geosciences and Remote Sensing,* Vol. 39, No. 5, May 2001.

[42] F. H. Wong, I. Cumming and Y. L. Neo. Focusing Bistatic SAR Data Using the Non-Linear Chirp Scaling Algorithm. *IEEE Transactions of Geosciences and Remote Sensing,* Vol. 46, No. 9, September 2008.

[43] Y. L. Neo, F. Wong and I. Cumming. A Two-Dimensional Spectrum for Bistatic SAR Processing Using Series Reversion. *IEEE Geosciences and Remote Sensing Letters*, Vol. 4, No. 1, Jan 2007.

[44] Y. L. Neo, F. Wong and I. Cumming. Focusing Bistatic SAR Images Using Non-Linear Chirp Scaling. *In RADAR 2004,* Toulouse, France, Oct 2004.

[45] Y. L. Neo, F. Wong and I. Cumming. An Effective Non-Linear Chirp Scaling Method of Focusing Bistatic SAR Images. *In EUSAR 2006,* Dresden, Germany, May 2006.

[46] R. Wang, O. Loffeld, Q. Ul-Ann, H. Nies, A. Medrano-Ortiz and A. Samarah. A Bistatic Point Target Reference Spectrum for General Bistatic SAR Processing. *IEEE Geosciences Remote Sensing Letters*, Vol. 5, No. 3, pp. 517-521, July 2008.

[47] R. Wang, O. Loffeld, H. Nies, S. Knedlik, Q. Ul-Ann, A. Medrano-Ortiz and J. H. G. Ender. Frequency Domain Bistatic SAR Processing for

Spaceborne/Airborne Configuration. *IEEE Transactions on Aerospace and Electronic Systems,* Vol. 46, No. 3, pp. 1329-1345, July 2010.

[48] R. Wang, O. Loffeld, Q. Ul-Ann, H. Nies, A. Medrano-Ortiz and S. Knedlik. A Special Point Target Reference Spectrum for Spaceborne/Airborne Bistatic SAR Processing. *In EUSAR 2008*, Friedrichshafen, Germany, June 2008.

[49] R. Wang, O. Loffeld, Q. Ul-Ann, H. Nies, A. Medrano-Ortiz and S. Knedlik. Analysis and Extension of Loffeld's Bistatic Formula in Spaceborne/Airborne Configuration. *In EUSAR 2008*, Friedrichshafen, Germany, June 2008.

[50] R. Wang, O. Loffeld, H. Nies, Q. Ul-Ann, A. Medrano-Ortiz, S. Knedlik and A. Samarah. Analysis and Processing of Spaceborne/Airborne Bistatic SAR Data. *In IGARSS 2008*, Boston, USA, July 2008.

[51] R. Wang, O. Loffeld, H. Nies, Q. Ul-Ann and A. Medrano-Ortiz. A Two-Step Method to Process Bistatic SAR Data in the General Configuration. *In RADAR 2008*, Rome, Italy, June 2008.

[52] Q. Ul-Ann, O. Loffeld, H. Nies and R. Wang. A General Bistatic SAR Focusing Algorithm for Azimuth Variant and Invariant Configurations. *In IET Radar 2012*, Glasgow, UK, Oct 2012.

[53] Q. Ul-Ann, O. Loffeld, H. Nies, R. Wang, K. Natroshvili and S. Knedlik. Performance Analysis of the Validity Constraints for the Bistatic SAR Processing. *In EUSAR 2008*, Friedrichshafen, Germany, June 2008.

[54] Q. Ul-Ann, O. Loffeld, H. Nies, R. Wang and S. Knedlik. Optimizing the Individual Azimuth Contribution of Transmitter and Receiver Phase Terms in Loffeld's Bistatic Formula (LBF) for Bistatic SAR Processing. *In IGARSS 2008*, Boston, USA, July 2008.

[55] Q. Ul-Ann, O. Loffeld, H. Nies and R. Wang. A Point Target Reference Spectrum Based on Loffeld's Bistatic Formula (LBF) for Hybrid Configurations. *In ICET 2008*, Rawalpindi, Pakistan, Oct 2008.

[56] Q. Ul-Ann, O. Loffeld, H. Nies and R. Wang. Considerations on the Validity Constraints for the Bistatic SAR Processing. *In ICICT 2009*, Karachi, Pakistan, Aug 2009.

[57] Q. Ul-Ann, O. Loffeld, H. Nies and R. Wang. Determining the Weighting Factor for the Unequal Azimuth Contributions of Transmitter and Receiver Phase Terms Based on the Validity Constraints for Bistatic SAR Processing. *In IRS 2009*, Hamburg, Germany, Sep 2009.

[58] Q. Ul-Ann, O. Loffeld, H. Nies and R. Wang. Considering the Linear and Quadratic Combination of Stationary Points for the Bistatic SAR Processing. *In EUSAR 2010*, Aachen, Germany, June 2010.

[59] R. Wang, O. Loffeld, Y. Neo, H. Nies and Z. Dia. Extending Loffeld's Bistatic Formula for General Bistatic SAR Configurations. *IET Radar Sonar and Navigation*, Vol. 4, No. 1, Jan 2010.

[60] R. Wang, O. Loffeld, H. Nies, S. Knedlik and J. H. Ender. Chirp Scaling Algorithm for the Bistatic SAR Data in the Constant-offset Configuration. *IEEE Transactions of Geosciences and Remote Sensing,* Vol. 47, No. 3, March 2009.

[61] R. Wang, O. Loffeld, H. Nies and A. Medrano-Ortiz. Focusing Results and Analysis of Advanced Bistatic SAR Experiments in Spaceborne or Airborne / Airborne or Stationary Configurations. *In EUSAR 2010*, Aachen, Germany, June 2010.

[62] R. Wang, O. Loffeld, Y. L. Neo, H. Nies, I. Walterscheid, T. Espeter, J. Klare and J. H. G. Ender. Focusing Bistatic SAR Data in Airborne/Stationary Configuration. *IEEE Transactions on Geosciences and Remote Sensing,* Vol. 48, No. 1, Jan 2010.

[63] W. M. Brown and R. J. Fredericks. Range Doppler Imaging with Motion through Resolution Cells. *IEEE Transactions on Aerospace and Electronics Systems,* Vol. AES-5, no. 1, pp. 98 – 102, 1969.

[64] D. C. Munson and R. L. Visentin. A Signal Processing View of Strip Mapping Synthetic Aperture Radar. *IEEE Transactions on Acoustics, Speech and Signal Processing,* Vol. 37, no. 12, pp. 2131 – 2147, 1989.

[65] D. Massonnet. The Interferometric Cartwheel: A Constellation of Passive Satellites to Produce Radar Images to be Coherently Combined. *International Journal of Remote Sensing,* Vol. 22, No. 12, 2001.

[66] R. Lanari. A New Method for the Compensation of the SAR Range Cell Migration Based on the Chirp Z-Transform. *IEEE Transactions on Geosciences and Remote Sensing,* Vol. 33, pp. 1296 – 1299, 1995.

[67] M. Soumekh. A System Model and Inversion for Synthetic Aperture Radar. *IEEE Transactions on Image Processing,* Vol. 1, no. 1, pp. 64 – 76, 1992.

[68] S. Duque, P. Lopez-Dekker and J.J. Mallorqui. Single-Pass Bistatic SAR Interferometry using Fixed-Receiver Configurations: Theory and Experimental Validation. *IEEE Transactions on Geosciences and Remote Sensing,* Vol. 48, No. 6, June 2010.

[69] F. Behner and S. Reuter. HITCHHIKER, Hybrid Bistatic High Resolution SAR Experiment Using a Stationary Receiver and TerraSAR-X Transmitter. *In EUSAR 2010,* Aachen, Germany, June 2010.

[70] S. Reuter, F. Behner, H. Nies, O. Loffeld, D. Matthes and J. Schiller. Development and Experiments of a Passive SAR Receiver System in a Bistatic Spaceborne/Stationary Configuration. *In IGARSS 2010,* Hawaii, USA, July 2010.

[71] I. C. Sikaneta. A Hybrid SAR Processing Method for Data Collected using a Stationary Bistatic Receiver. *In EUSAR 2008*, Friedrichshafen, Germany, June 2008.

[72] J. Sanz-Marcos, J. J. Mallorqui, A. Aguasca and P. Prats. First ENVISAT and ERS-2 Parasitic Bistatic Fixed Receiver SAR images Processed with the Subaperture Range-Doppler Algorithm. *In EUSAR 2006*, Dresden, Germany, May 2006.

[73] J. Sanz-Marcos, P. Lopez-Dekker, J. J. Mallorqui, A. Aguasca and P. Prats. SABRINA: A SAR Bistatic Receiver for Interferometric Applications. *IEEE Geosciences Remote Sensing Letters*, Vol. 4, No. 2, April 2007.

[74] C. E. Yarman, B. Yazc and M. Cheney. Bistatic Synthetic Aperture Radar Imaging for arbitrary flight trajectories. *IEEE Transaction on Geosciences and Remote Sensing*, Vol. 17, No. 11, pp. 84 – 93, Jan 2008.

[75] A. Moreira. *Radar mit Synthetischer Apertur: Grundlagen und Signalverarbeitung*. Habilitationsschrift, Oct 2000.

[76] I. Cumming and F. Wong. *Digital Processing of Synthetic Aperture Radar Data Algorithms and Implementation*. Artech House, 2005.

[77] J. C. Curlander and R. N. McDonough. *Synthetic Aperture Radar: System and Signal Processing*. Wiley Interscience, 1991.

[78] A. Hein. *Processing of SAR Data: Fundamentals, Signal Processing and Interferometry.* Springer Verlag, 2004.

[79] John J. Kovaly. *Synthetic Aperture Radar.* Artech House, ISBN: 0-89006-056-8.

[80] J. Patrick Fitch. *Synthetic Aperture Radar.* Springer Verlag, 1988.

[81] M. Soumekh. *Synthetic Aperture Radar Signal Processing with MATLAB Algorithms.* Wiley Interscience, 1999.

[82] G. Franceschetti and R. Lanari. *Synthetic Aperture Radar Signal Processing.* CRC Press, ISBN: 0-8493-7899-0.

[83] A. V. Oppenheim and A. S. Willsky. *Signals and Systems*. Prentice Hall, 1996, ISBN: 0-13-651175-9.